

# **Robust adaptive beamforming for clutter rejection on atmospheric radars**

by

**Taishi Hashimoto**



# Contents

<b>1</b>	<b>General Introduction</b>	<b>1</b>
1.1	Introduction	1
1.2	Fundamentals of pulse Doppler radar	2
1.2.1	Radio waves	2
1.2.2	Radar basics	2
1.2.3	Ranging	3
1.2.4	Doppler velocity measurement	3
1.2.5	Radar equation	5
1.3	Phased antenna arrays	7
1.3.1	Array manifold vector	8
1.3.2	Nonadaptive beamforming	8
1.3.3	Array factor and radiation pattern	8
1.3.4	Calculation of element pattern	10
1.4	Atmospheric radar observation	10
1.4.1	Atmospheric echoes	11
1.4.2	Clutter contamination	12
1.4.3	Galactic Noise	17
1.5	Wind velocity measurement using atmospheric Doppler radars	20
1.5.1	Data acquisition and signal processing overview	20
1.5.2	Power spectrum and periodogram	22
1.5.3	Detectability	23
1.5.4	Noise floor level estimation	24
1.5.5	Estimation of radial Doppler velocity	29
1.5.6	3-D wind field measurement	29
1.6	Conventional clutter suppression techniques for atmospheric radars	30
1.6.1	Moving target indication	31
1.6.2	Pulse Doppler processing	31
1.7	Clutter suppression techniques using adaptive beamforming	32
1.7.1	Directionally constrained minimization of power	32
1.7.2	Norm-constrained DCMP algorithm	33

1.8	Organization of this thesis . . . . .	35
<b>2</b>	<b>Meteor clutter rejection and accurate measurement of the wind velocity in Mesosphere</b>	<b>36</b>
2.1	Introduction . . . . .	36
2.2	System model . . . . .	39
2.3	Methods for generating simulated signals of atmospheric radar observation	39
2.3.1	Some representative quantities in a Doppler spectrum . . . . .	39
2.3.2	Atmospheric signal generation . . . . .	41
2.3.3	Clutter signal generation . . . . .	44
2.3.4	Noise generation . . . . .	44
2.4	Simulation of adaptive meteor clutter rejection . . . . .	45
2.4.1	Signal generation . . . . .	45
2.4.2	Adaptive signal processing . . . . .	45
2.4.3	Incoherent integration and meteor trail echo rejection . . . . .	46
2.4.4	Detailed simulation settings . . . . .	46
2.4.5	Results and discussion . . . . .	49
2.5	Applying the adaptive meteor clutter rejection technique to an actual observation . . . . .	52
2.5.1	Observational settings of the radar system . . . . .	52
2.5.2	Signal processing . . . . .	53
2.5.3	Results and discussion . . . . .	54
2.6	Summary and concluding remarks . . . . .	58
<b>3</b>	<b>Adaptive sidelobe cancellation technique for atmospheric radars containing arrays with nonuniform gain</b>	<b>59</b>
3.1	Introduction . . . . .	59
3.2	Adaptive beamforming technique for nonuniform-gain array . . . . .	60
3.2.1	Kamio's Method . . . . .	60
3.2.2	Gain-weighted NC-DCMP algorithm . . . . .	60
3.3	Performance evaluation with numerical simulations . . . . .	61
3.3.1	System model . . . . .	61
3.3.2	Signal generation . . . . .	64
3.3.3	Signal processing . . . . .	66
3.3.4	Statistical evaluation and performance indices . . . . .	67
3.3.5	Results and Discussion . . . . .	67
3.4	Application to actual observations . . . . .	71
3.4.1	Observation Settings . . . . .	71

3.4.2	Signal Processing . . . . .	71
3.4.3	Performance Evaluation Method . . . . .	71
3.4.4	Results and Discussion . . . . .	72
3.5	Summary and concluding remarks . . . . .	75
<b>4</b>	<b>User parameter-free diagonal-loading scheme for clutter rejection on atmospheric radars</b>	<b>77</b>
4.1	Introduction . . . . .	77
4.2	Proposed power balance algorithm . . . . .	78
4.2.1	Estimation of SNR and SIR degradations . . . . .	78
4.2.2	Formulation of the cost function . . . . .	82
4.2.3	The procedure for the power balance algorithm . . . . .	84
4.3	System model . . . . .	86
4.4	Numerical simulations . . . . .	90
4.4.1	Simulation settings . . . . .	90
4.4.2	Signal generation . . . . .	92
4.4.3	Signal processing and performance evaluation . . . . .	94
4.4.4	Results and discussion . . . . .	95
4.5	Application to radar observations . . . . .	99
4.5.1	Observations . . . . .	99
4.5.2	Signal processing . . . . .	99
4.5.3	Results and discussion . . . . .	100
4.6	Summary and concluding remarks . . . . .	102
<b>5</b>	<b>Concluding remarks</b>	<b>104</b>

# List of Tables

1.1	Three test cases used in the simulation. These are based on the standard observation of the MU radar. . . . .	28
1.2	Comparison of the strict and Gaussian-approximated segment methods. $a \pm b$ denotes mean $a$ and standard deviation $b$ . Cases are defined in Table 1.1. . . . .	28
2.1	Radar settings used in the simulation of meteor clutter rejection. . . . .	47
2.2	Parameters for generating atmospheric echoes in simulation 2. . . . .	48
2.3	Parameters for generating meteor echoes in simulation 2. . . . .	48
2.4	Radar system settings for the observation made by the MU radar on 14:05 to 15:46 (UTC), October 8, 2011. . . . .	53
2.5	Threshold $B_t$ for discarding contaminated spectra in incoherent integration, the defection ratio $R_d$ with thresholding and the equivalent number of incoherent integration $\hat{N}_i$ for the observation. . . . .	58
3.1	Observational parameters of the MU radar. . . . .	65
4.1	Simulation parameters used for generating atmospheric backscatter signals. . . . .	93
4.2	Parameters for observations made on March 20, 2015, by the PANSY radar. . . . .	99

# List of Figures

1.1	Basics of a radar system. . . . .	2
1.2	Coherent detector. . . . .	4
1.3	The radar volume. . . . .	6
1.4	An example of phased array system. . . . .	7
1.5	Example of array factor and radiation pattern. . . . .	9
1.6	An example Doppler spectrum in ST region observed by the MU radar, containing the ground and aircraft clutter. . . . .	13
1.7	An example Doppler spectrum in mesosphere region observed by the MU radar, containing the meteor trail echoes. . . . .	14
1.8	Illustration of the IS observation and the FAI echo contamination in the PANSY radar. . . . .	16
1.9	Range-time-intensity plot for the incoherent scattering (upper) and FAI echoes (lower) observed by the PANSY radar. . . . .	17
1.10	All-sky map of the galactic noise at 12:00 UTC (15:00 LT), March 31 2015. Modified after Guzmán et al. (2011). . . . .	18
1.11	(a) Noise temperature extracted from Fig. 1.10, and (b) observed noise floor level for zenith, north, and south beams of the PANSY radar. . . . .	19
1.12	Schematic flow of data acquisition and signal processing of atmospheric radars to obtain the radial Doppler velocity. . . . .	21
1.13	An example of the Gaussian approximation for $\chi^2$ distribution. . . . .	27
1.14	Illustration of the Doppler beam swing method for phased arrays. . . . .	30
1.15	Beam directional error in the DCMP algorithm. . . . .	33
2.1	The antenna position and channel assignment of the MU radar. Modified after Fukao et al. (1985a). . . . .	37
2.2	The block diagram of of the MU radar (Hassenpflug et al., 2008). . . . .	38
2.3	Representative quantities in a Doppler spectrum. . . . .	40
2.4	Example of the spectra generated in simulation 1. SIDR is $-5$ dB. . . . .	50
2.5	RMS errors of wind velocity estimated with the nonadaptive beamforming and NC-DCMP algorithm. . . . .	51

2.6	(a) RMS errors of the wind velocity estimations of the nonadaptive beamforming and NC-DCMP algorithm. (b) Intensities of the atmospheric and meteor echoes for each range. . . . .	52
2.7	The range-time-intensity plot for the whole observed data. . . . .	54
2.8	Overlaid spectral peaks processed by the nonadaptive beamforming and its threshold $B_t$ . . . . .	55
2.9	Overlaid spectral peaks processed by the NC-DCMP algorithm and its threshold $B_t$ . . . . .	56
2.10	Estimated wind velocity for each range obtained by the nonadaptive beamforming and NC-DCMP algorithm. . . . .	57
3.1	Antenna position and channel number assignment of the MU radar for both simulation and observation. The five black circles in the outer groups are sub-array antennas used in types B and C. . . . .	62
3.2	Azimuth section of one-way directional gains at $\phi = 0^\circ$ for the main array (Main), and one of the main array channel consisting of 19 crossed Yagi antennas indicated by a hexagon in Fig. 3.1 (Hex). . . . .	63
3.3	Azimuth section of one-way directional gains at $\phi = 0^\circ$ for one of the sub-array groups of type A (dotted), B(solid), and C (dashed). . . . .	64
3.4	(a) Clutter suppression ratio $Z$ and (b) SNR loss $L$ . . . . .	68
3.5	Performance index $Q$ . . . . .	69
3.6	Range profile of the DC component obtained by the uniform and gain-weighted NC-DCMP algorithms. . . . .	73
3.7	Example of the range section at 5 km, which is indicated by a horizontal line in Fig. 3.6. . . . .	74
3.8	Comparison of the performance indices $Z$ , $L$ and $Q$ for the uniform NC-DCMP algorithm (Uni), the Kamio method (KM), and the gain-weighted NC-DCMP algorithm (GW) throughout the roughly 1-hour duration of observations. . . . .	75
4.1	Output power diagram for nonadaptive beamforming, the standard DCMP algorithm, and an intermediate diagonal-loading value $\alpha$ , respectively. Hatched area indicates the SIR degradation compared with the standard DCMP algorithm, and dotted area denotes the SNR degradation compared with nonadaptive beamforming. . . . .	79
4.2	Example of the relationship between the SIR degradation factor $\Delta P_I(\alpha)$ (abscissa) and SNR degradation factor $\Delta P_N(\alpha)$ (ordinate) for various diagonal-loading values $\alpha$ . Gray circles indicate the magnitude of $\alpha$ . . . . .	81

4.3	Example of the relationship between various diagonal-loading values $\alpha$ and the cost function of the PB algorithm, $f(\alpha)$ , and standard DCMP algorithm, $g(\alpha)$ . . . . .	83
4.4	The radiation pattern of the PANSY radar. . . . .	86
4.5	The antenna position and channel assignment of the PANSY radar. . . . .	87
4.6	The block diagram of of the PANSY radar (Sato et al., 2014). . . . .	88
4.7	The planning (upper left) and current (upper right) antenna arrangement and the resulting array patterns (lower) of the PANSY radar. . . . .	89
4.8	Antenna position and subarray configuration of the PANSY radar used for simulations and observations. Each set of antennas surrounded by a polygonal frame indicates a single channel in the uniform-gain configuration. Each hexagon with black circles indicates a subarray used as the sidelobe canceller in the nonuniform-gain configuration. In the nonuniform-gain configuration, all antennas with white circles are synthesized in-phase. . . . .	91
4.9	Power directionality pattern of the main array (Main) and one of the subarrays of the sidelobe canceller array (SC) used for observations. This is the section at an azimuth angle of $45^\circ$ . . . . .	92
4.10	(a) Average SINDR, and (b) beam directional error compared with the nonadaptive beamforming for the DCMP algorithm (DCMP), NC-DCMP algorithm (NC), and the proposed PB algorithm (PB) in the simulation for uniform-gain (U) and nonuniform-gain (N) configurations. The input SNDR is 20 dB. . . . .	96
4.11	Average SINDRs for the input SNDR of 40 dB. . . . .	97
4.12	An example of the reception beam pattern synthesized by the DCMP algorithm (DCMP), NC-DCMP algorithm (NC), and the proposed PB algorithm (PB) when the input SNDR is 40 dB. This is the section at an azimuth angle of $45^\circ$ . . . . .	98
4.13	Doppler spectra at (a) 6.0 km and (b) 4.2 km, which is averaged for about 40 min. . . . .	101

# Acknowledgments

This thesis and related works in Toru Sato laboratory, Graduate School of Informatics, Kyoto University, could not have been accomplished without the kind support of many people, whom I would like to gratefully acknowledge.

At the outset, I would like to express my profound gratitude to Professor Toru Sato, my supervisor, for his continuous support and consistent guidance. His great leadership has always spurred me carrying out my study, and his outstanding insight and immense knowledge invariably directed me to find the right solution. I am highly honored to be able to learn the professional awareness of engineer and scientist from him. I would also like to extend my sincere appreciation to Project Associate Professor Koji Nishimura, at the National Institute of Polar Research (NIPR), for his constructive advice and technical assistance. His pertinent comments greatly contributed to improve the quality of this study.

I am deeply indebted for the committee members of the thesis examination, Professors Masahiro Morikura and Mamoru Yamamoto. They kindly spared their precious time for thoroughly reviewing and discussing on my work. Their insightful comments and suggestions strongly stimulated me to complete this thesis.

This work used the observations from the MU radar and the PANSY project. The Shigaraki MU observatory and the MU radar were operated by the Research Institute for Sustainable Humanosphere, Kyoto University. I am thankful to the committee of the MU radar collaborative research program for adopting my proposal of the observation. PANSY is a multi-institutional project, with a core team at both The University of Tokyo and NIPR. I would like to thank Professor Kaoru Sato, at The University of Tokyo, Associate Professor Masaki Tsutsumi, at NIPR, and all other member of the PANSY project for offering me the great opportunity to work in the world's leading research project on polar atmospheric science. The PANSY radar was operated by the Japanese Antarctic Research Expedition (JARE) at the Syowa Station, Antarctic. I thank all the member of JARE for their persistent efforts on maintaining the observations.

I would also like to extend my sincere gratitude to the staffs in Toru Sato Laboratory. I am deeply grateful to Associate Professor Seiji Norimatsu for his constructive remarks and criticism. He was always attentive to details of my writings and presentations, and gave me precise advices. I wish to express my gratitude to Associate Professor Takuya

Sakamoto, now at University of Hyogo, and Assistant Professor Hirofumi Taki, now at Tohoku University, for the fruitful discussions with them. My special thanks go to Secretary Mses. Mari Watanabe and Syoko Horibe for their careful supports.

My cordial thanks also go to colleagues in Toru Sato laboratory. I would like to extend my through gratitude to Assistant Professor Kenshi Saho, now at Ritsumeikan University, for his dedicated coaching on research methods. I have learned lots of presentation techniques from his comprehensible talk. I would like to thank Mr. Shigeaki Okumura for his continuous support on the daily life in laboratory. He took care of many troublesome desk works for me. For maintaining the computer networks in Toru Sato laboratory, Messrs. Yuichiro Kano and Kentaro Ohishi helped me a lot, whom I would like to acknowledge.

Part of this work was done during my stay at the Syowa Station as a wintering member of the JARE54. I would like to thank my colleagues at JARE54, especially to Associate Professor Yoshihiro Tomikawa, at NIPR, and Mr. Kazuhiko Mushiake, Mitsubishi Electric, for supporting me at the Syowa Station both officially and privately.

Last but not least, my heartfelt gratitude goes to my family for their through support, patience, tolerance, and understanding. I would like to profoundly thank my parents Tetsuya and Harumi, grandparents Masami and Kazuko. My sincere thanks also goes to my brother Leon for discussing on various topics related to this work.

# Preface

The modern weather forecast is made through the combination of the initial condition from the currently observed state and the numerical model of the atmosphere calculated using the given initial conditions. The accuracy of the prediction is highly sensitive to errors in the initial conditions, especially for the long term forecast. Hence, the quality of observed data is the key to improve the accuracy of numerical model predictions.

Wind velocity is one of the important values for the initial conditions of numerical weather predictions, which is mainly obtained by ground-based radars. These radars observe the weak backscattered radio waves from the irregularities of refractive index in the atmosphere. However, radio waves spreads in all directions and are backscattered by various objects, e.g., the ground or water surfaces, aircrafts, birds, and other natural phenomena which are not of interest. Thus, the returned atmospheric signals are always contaminated by interference from undesired directions, called clutter. Among various clutter, ground clutter can cause severe biases in estimated wind velocities, because it semipermanently exists with much higher intensity than atmospheric signals. Therefore, ground clutter suppression is critical for accurate wind measurements using radars.

Modern radar systems for wind measurements generally employ the pulse Doppler radar, which can observe the radial wind velocity using the Doppler effect. To obtain the mean Doppler shift, the spectral fitting method is usually used, assuming the atmospheric spectral shape to have some statistical distributions, e.g., Gaussian. In this method, the effect of the ground clutter is relatively small when observing the off-vertical directions, because the radial Doppler velocity becomes sufficiently larger than zero, enabling the spectral filtering for the ground clutter. However, when observing the vertical wind velocity, the spectral peak usually exists near the zero Doppler component, because the vertical wind velocity is typically very small. In this case, the ground clutter becomes serious problem, e.g., disabling the use of the point with the highest signal-to-noise ratio, or obscuring the entire atmospheric spectrum with the spread clutter spectrum caused by the fading.

Recently, advanced computing technologies have enabled the real-time adaptive signal processing of the observed data from the multiple spatially distributed receivers. Particularly, in large atmospheric radars, phased antenna arrays have been commonly used in order to realize the rapid beam steering and large antenna aperture at the same

time, thus making the system well compatible with such adaptive beamforming techniques. By employing these methods on the phased array systems, one can suppress the interference signals from different directions than the desired one by synthesizing the output signals of each receiver with appropriate weighting in amplitude and phase, which is determined from the observed data itself.

One of the difficulties in adaptive beamforming is balancing the clutter suppression capability with the loss of signal detectability. The basic methodology for adaptive beamforming on atmospheric radars is the linearly constrained power minimization technique. This method finds the optimal weighting for each receiver that minimizes the total output power of the array under certain constraints, i.e., keeping the response to the desired direction. By employing the optimal weight, an optimal reception beam pattern is formed to suppress only the clutter signal with its mainlobe directed to the desired direction and its nulls directed to the incident angles of the interference. However, this method only works fine if the directional constraint is consistent with the actual incident angle of the desired signal and the desired signal power is sufficiently weak. Otherwise, the desired signal is suppressed as well as the clutter signal, or the background noise power is enhanced to degrade the signal detectability.

To prevent such a signal loss, additional constraint about the increased noise power, called the norm constraint, has been introduced. Although this modification was confirmed to be effective by applying it to observations of large atmospheric radars and weather radars, it was also shown that, in some situations, the norm constraint may be too strict in preventing the noise power increase to suppress the strong clutter. Because this residual clutter also degrades the signal detectability, the more universal algorithm that can balance the clutter suppression capability with the loss of signal detectability has been desired. Furthermore, the suitable array design and the element directional gains for adaptive beamforming on atmospheric radars have not been thoroughly studied.

This thesis presents two techniques that address these problems. The first one is the optimal array design guideline for atmospheric radars using adaptive beamforming. The key concept is the partial adaptive array, i.e., the large main array supplemented by small sidelobe canceller array. The optimal element gain functions for elements of the sidelobe canceller array is also considered. The second one is a novel clutter suppression algorithm. This method evaluates the clutter suppression capability and the noise power increase separately, and determines the optimal weight by balancing these two quantities. The method has the universality and robustness against the variation of signal or interference power.

# List of acronyms and abbreviations

Following acronyms and abbreviations are used in multiple chapters throughout this thesis. Each chapter introduces additional notation at the first usage.

3-D	three dimensional
CMD	clutter mitigation decision
CSR	clutter suppression ratio
dB	decibel
DBS	Doppler beam swing
DC	direct current
DCMP	directionally constrained minimization of power
E	east
FAI	field aligned irregularities
FIR	finite impulse response
GW	gain weighted
HPHW	half power half width
I	in-phase signal component
IIR	infinite impulse response
IPP	inter pulse period
IS	incoherent scattering
JARE	Japanese Antarctic Research Expedition
KM	Kamio's method
LT	local time
MOM	method of moments
MST	mesosphere-stratosphere-troposphere
MTI	moving target indication
MU radar	middle and upper atmosphere radar
N	north
NA	nonadaptive beamforming
NC	norm constrained
NC-DCMP	norm-constrained DCMP
NEC	numerical electromagnetic code

NIPR	National Institute of Polar Research
PANSY radar	Program of Antarctic Syowa MST/IS radar
PB	power balance
PDF	probability density function
PIAA	power inversion adaptive array
PRI	pulse repetition interval
Q	quadrature-phase signal component
RADAR	radio detecting and ranging
RF	radio frequency
RMS	root-mean-square
Rx	reception/receiving
S	south
SC	sidelobe canceller
SIR	signal-to-interference ratio
SIDR	signal-to-interference density ratio
SINR	signal-to-interference-plus-noise ratio
SINDR	signal-to-interference-plus-noise density ratio
SNR	signal-to-noise ratio
SNDR	signal-to-noise density ratio
ST	stratosphere-troposphere
Tx	transmission/transmitting
UTC	coordinated universal time
VAD	velocity azimuth display
VHF	very high frequency
W	west
Z	zenith

# List of common symbols

Following symbols are used in multiple chapters throughout this thesis. Each chapter also introduces their meaning at the first usage. Some symbols have more than one usage; their meaning is generally clear from the context.

$(\cdot)^*$	complex conjugate
$(\cdot)^T$	matrix transposition
$(\cdot)^H$	matrix conjugate transposition (Hermitian matrix)
$\langle(\cdot)\rangle$	ensemble average
$\alpha$	diagonal loading value (pseudo noise)
$\gamma$	forgetting factor, weighting factor
$\Delta t$	a short time interval
$\Delta T$	pulse width
$\Delta r$	range resolution
$\eta$	radar cross section per unit volume
$\theta$	zenith angle
$\theta_b$	half power half beam width
$(\theta_o, \phi_o)$	desired direction of a beamformer
$\lambda$	wave length
$\mu$	mean
$\pi$	circumference ratio (= 3.14159265...)
$\sigma_d$	spectral width
$\sigma_k$	standard deviation
$\tau$	fast time
$\phi$	azimuth angle
$\chi_k^2$	$\chi$ distribution with $k$ degrees of freedom
$\omega$	angular frequency
$\omega_d$	angular Doppler frequency
$\mathbf{A}(\theta, \phi)$	array manifold vector (steering vector)
$A_e$	effective antenna aperture
$c$	speed of light in atmosphere
$c_0$	speed of light in vacuum (= 299 792 458 m s <sup>-1</sup> )

<b>C</b>	directional constraint
$E[(\cdot)]$	expectation value
$f$	frequency
$f_d$	Doppler frequency shift
$f_{d\max}$	Nyquist frequency
$\mathcal{F}[(\cdot)]$	Fourier transform
$\mathcal{F}^{-1}[(\cdot)]$	inverse Fourier transform
$G$	gain
$H$	constraint response
$j$	imaginary unit
$k$	wavenumber, discrete sample index
<b>I</b>	3-D location
<b>L</b>	3-D location
$L_{\text{dB}}$	permissible SNR degradation in dB
$L_{\text{SNR}}$	SNR degradation factor
$M$	the number of antennas or receiver channels
$\mathbf{n}(t), \mathbf{n}(k)$	noise signal vector
$\mathcal{N}(\mu, \sigma)$	Gaussian distribution with mean $\mu$ and standard deviation $\sigma$
$N_b$	No. of beam
$N_d$	No. of segments
$N_f$	No. of frequency sample points
$N_h$	No. of range sample points
$N_i$	No. of incoherent integration
$N_s$	No. of velocity sample points in a segment
$N_t$	No. of time sample points
$N_v$	No. of velocity sample points
$N_w$	No. of samples averaged for covariance matrix in a single side
$P_I$	clutter power
$P_N$	mean noise power
$P_R$	received power
$P_S$	atmospheric spectral peak power
$P_t$	transmitted power
$r$	range
$r_{\max}$	maximum range without aliasing
<b>R</b>	covariance matrix
$\mathbf{s}(t), \mathbf{s}(k)$	desired signal vector
$S(\omega), S(v)$	periodogram, spectrum

$\bar{S}$	periodogram after incoherent integration
$t$	time, slow time
$T$	duration
$T_D$	detectability threshold
$T_p$	IPP, PRI
$\mathbf{u}(t), \mathbf{u}(k)$	interference signal vector
$U$	norm constraint
$v$	velocity
$v_d$	Doppler velocity
$v_{dmax}$	maximum Doppler velocity without aliasing
$V$	radar volume
$\mathbf{V}(\theta, \phi)$	radial unit vector
$\mathbf{W}$	weight vector
$\mathbf{X}$	input signal vector
$Y$	synthesized output of a beamformer

# Chapter 1

## General Introduction

### 1.1 Introduction

Radar remote sensing of Earth's atmosphere has become all the more important for both monitoring the global climate changes and predicting natural disasters caused by abnormal weathers. Among the various instruments, ground-based radars have the capability of continuously observing the wind velocities in wide height range or area with high temporal and spatial resolutions. However, because radio waves spread in all directions, interference from undesired directions, called clutter, becomes a serious problem. Typically, the source of clutter is a hard target, e.g., the ground surface, building, aircrafts or birds. Because atmospheric backscattered signals are extremely weak compared to those from such clutter sources, the clutter can obscure the desired signal, or bring intolerable biases in wind measurements. Thus, signal processing techniques for extracting the desired information have been extensively studied, such as high-pass filtering in time or frequency domain and spectral fitting. More recently, advanced computer technologies have enabled the software synthesis of the output signals of phased antenna arrays determining the appropriate weights for phases and amplitudes using the observed data. This technique is called adaptive beamforming, which is considered to be the promising countermeasure in clutter suppression of modern radar systems.

The goal of this thesis is to propose a novel adaptive clutter suppression algorithm for atmospheric radars, as well as the suitable array design for this purpose. This chapter provides an overview of the theory and signal processing techniques used in atmospheric radars. In sections 1.2 and 1.3, fundamentals of the pulse Doppler radars and phased antenna arrays are presented. In section 1.4, radar observation of Earth's atmosphere, as well as various clutter and noise sources are briefly reviewed. In section 1.5, data acquisition and signal processing procedures on atmospheric radars are described. In section 1.6, the conventional clutter suppression techniques are presented. Finally, in section 1.7, basic methodologies of adaptive beamforming is explained.

## 1.2 Fundamentals of pulse Doppler radar

### 1.2.1 Radio waves

Radio waves are electromagnetic radiation that have frequencies  $f$  from 3 kHz to 3 THz. They travel at the speed of light in vacuum,  $c_0$ , which is defined as  $c_0 = 299\,792\,458\text{ m s}^{-1}$  without uncertainty. In other medium, it is slightly changed because of the different magnetic permeability and electric permittivity, although the speed of light in the Earth's atmosphere,  $c$ , is very close to  $c_0$ . The wavelength  $\lambda$  can be written by using  $f$  and  $c$  as follows:

$$\lambda = c/f. \quad (1.1)$$

### 1.2.2 Radar basics

Radar (or RADAR: radio detection and ranging) is an instrument that uses radio waves to detect a target, measure the distance or direction to the target, or estimate the shape of the target. Figure 1.1 describes the basics of a radar system. A radar transmits radio

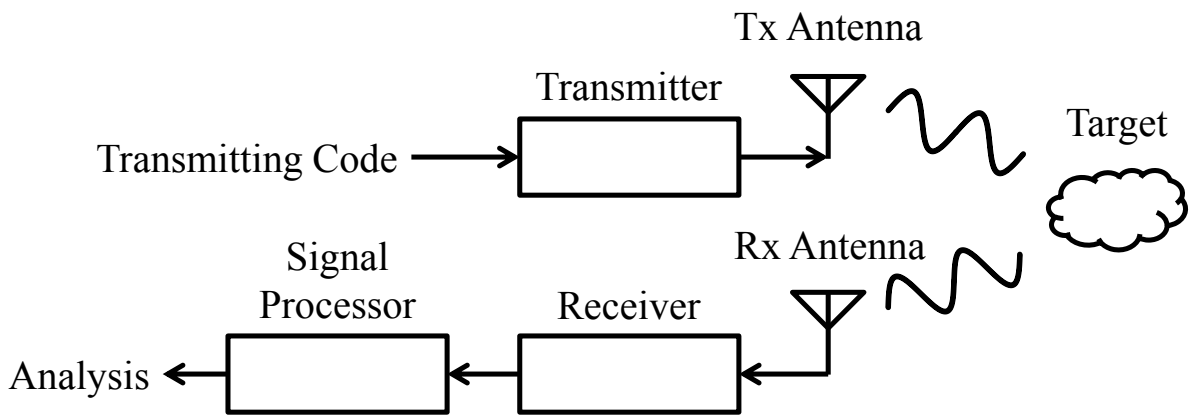


Figure 1.1: Basics of a radar system.

frequency (RF) signals from transmitting (Tx) antennas to the region of interest. The transmitted radio waves propagate through medium (e.g., atmosphere, water, or vacuum), and induce currents on the surface of targets in ahead of the radar. This induced currents reradiate radio waves, and some of them are returned to the radar. This process

is called backscattering. The backscattered radio waves travel back again, and are incident on the receiving (Rx) antennas. Note that Tx and Rx antennas may be the same antennas; in such systems, transmitted and received RF signals are separated by a switch and circulator. The incident radio waves induce currents on the Rx antennas again, and the signal is detected by the receiver. Further signal processing may be performed on the received signal, e.g., pulse decoding and Fourier transform.

### 1.2.3 Ranging

To measure the distance to a target from the radar, the time of flight of a pulse is generally used in pulse Doppler radars. As mentioned above, radio waves travel at the speed of light,  $c$ . Hence, the range to the target from the radar,  $r$ , can be written as follows:

$$r = 0.5cT, \quad (1.2)$$

where  $T$  is a duration between transmitting and receiving an RF pulse, i.e., for a round trip. In practice, RF pulses are not ideal impulses, causing an uncertainty in the determination of the range to a target. Let  $\Delta T$  be the pulse width, i.e., the duration of the high voltage in transmitted pulse. The range resolution,  $\Delta r$ , is then written in the same manner as Eq. (1.2):

$$\Delta r = 0.5c\Delta T. \quad (1.3)$$

### 1.2.4 Doppler velocity measurement

If the target is moving, the Doppler effect may be observed in backscattered radio waves. Let  $v$  be the speed of the target projected onto the line of sight from the radar to the target. The frequency of the backscattered signal is subject to the following relationship (e.g., Richards et al., 2010):

$$f' = \frac{c+v}{c-v}f = \frac{1+v/c}{1-v/c}f \quad (1.4)$$

$$= (1+v/c) \left( 1 + (v/c) + (v/c)^2 + \dots \right) \quad (1.5)$$

$$\sim \left( 1 + \frac{2v}{c} \right) f, \quad (1.6)$$

where  $f'$  is the frequency of the received radio waves. Equation (1.6) is derived by an assumption  $v \ll c$ . The Doppler frequency shift  $f_d$  is then obtained as the difference

between  $f'$  and  $f$ :

$$f_d = f' - f = \frac{2v}{c}f. \quad (1.7)$$

The mean Doppler velocity  $v_d$  is given by (e.g., Richards et al., 2010):

$$v_d = -\frac{\lambda}{2}f_d = -\frac{\lambda}{4\pi}\omega_d, \quad (1.8)$$

where  $\omega_d = 2\pi f_d$  is the Doppler angular frequency. The maximum Doppler velocity  $v_{d\max}$  observable without aliasing is limited by the Nyquist frequency  $f_{d\max}$  determined by the pulse repetition interval (PRI)  $T_p$ :

$$f_{d\max} = \frac{1}{2T_p}, \quad (1.9)$$

$$v_{d\max} = \frac{1}{2}\lambda f_{d\max} = \frac{\lambda}{4T_p}. \quad (1.10)$$

In actual, the Doppler frequency shift  $f_d$  cannot be obtained by monitoring a single voltage time series, because phase rotation and amplitude variation cannot be distinguished. Thus, the coherent detector is generally used, which is illustrated in Fig. 1.2. Here,  $\omega_0$  is the angular frequency of the radar system,  $A$  is the amplitude of the received

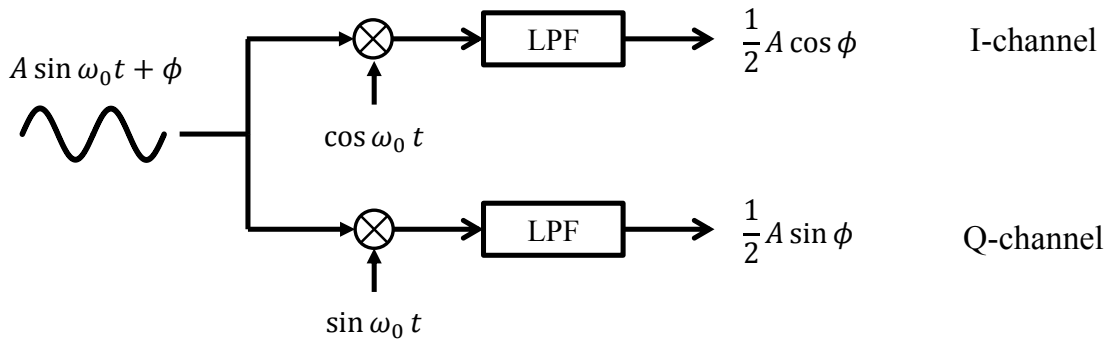


Figure 1.2: Coherent detector.

voltage signal, and  $\phi$  is the phase of the received voltage signal. In coherent detection,

the received signal is mixed by the reference signals generated by the local oscillator; one has a phase without modification and the other has a delay of  $90^\circ$ . These two channels are called in-phase (I) and quadrature-phase (Q) channels, respectively. Discrete time samples from both I and Q channels construct a complex time series  $x(k)$  called analytic signal:

$$x(k) = A(k) [\cos \phi(k) + j \sin \phi(k)] = A(k) \exp j\phi(k), \quad (1.11)$$

where  $A(k)$  and  $\phi(k)$  is the discrete time series of amplitude and phase. By using Eq. (1.11), the amplitude  $A(k)$  and phase  $\phi(k)$  can be separately measured. The Doppler frequency shift  $f_d$  can then be observed using successive samples of  $\phi(k)$ . Suppose the interval of two adjacent samples is  $\Delta t$ , and the radial velocity of the target is  $v_d$ . The distance of which the target travels in  $\Delta t$  is  $v_d \Delta t$ . The observed phase rotation can be related with this distance by the following expressions:

$$\frac{\lambda}{2\pi} [\phi(k) - \phi(k-1)] = v_d \Delta t = -\frac{\lambda f_d \Delta t}{2}, \quad (1.12)$$

$$\therefore f_d = -\frac{1}{\pi \Delta t} [\phi(k) - \phi(k-1)]. \quad (1.13)$$

Here, in Eq. (1.12), the relationship in Eq. (1.8) is used. Equation (1.13) indicates that the Doppler frequency shift can be obtained by measuring the phase rotation in the time series of the analytic signal.

## 1.2.5 Radar equation

The radar range equation is a useful tool to estimate the received echo power. For small distributed targets, the radar range equation is written as (e.g., Fukao et al., 2014):

$$P_r = \frac{P_t G A_e}{(4\pi)^2 r^4} V \eta, \quad (1.14)$$

where  $P_r$  is the received power,  $P_t$  is the transmitted power,  $G$  is the Tx antenna gain,  $A_e$  is the Rx antenna aperture,  $r$  is the distance to the target,  $V$  is the radar volume illuminated by the Tx beam, and  $\eta$  is the radar reflectivity which is the radar cross section per unit volume.

In atmospheric radar, the radar volume  $V$  can be considered as a circular truncated cone, which is the shaded area in Fig. 1.3. In this case, the half taper angle of the cone is  $\theta_b$ , which is approximately equivalent to the half power half width (HPHW) of the

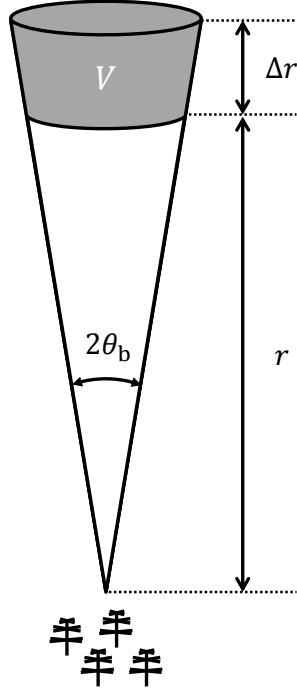


Figure 1.3: The radar volume.

radar beam.  $\Delta r$  is the range resolution which is derived by the Tx pulse width  $\Delta T$  using Eq. (1.3). The radar volume  $V$  is then written as:

$$V \sim \pi\theta_b^2 r^2 \Delta r, \quad (1.15)$$

for  $\Delta r \ll r$  and small  $\theta_b$ .

The effective aperture  $A_e$  and the beam width  $\theta_b$  has the following relationship (Richards et al., 2010):

$$\theta_b^2 = \gamma_b \frac{\lambda^2}{A_e}, \quad (1.16)$$

where  $\gamma_b$  is the beam width factor. The gain  $G$  and  $A_e$  also have the well-known relationship (Richards et al., 2010):

$$G = \frac{4\pi}{\lambda^2} A_e. \quad (1.17)$$

Note that  $A_{e0} = \lambda^2/4\pi$  is the effective aperture of an isotropic antenna. Substituting Eqs. (1.3) and (1.15) to (1.17) into Eq. (1.14) yields:

$$P_r = \delta_b \frac{P_t A_e \Delta T}{r^2} \eta, \quad (1.18)$$

where  $\delta_b = \gamma_b c/8$  is a constant. As in Eq. (1.18), the power of received signal is proportional to the transmitted power  $P_t$ , the effective antenna aperture  $A_e$ , and the pulse width  $\Delta T$ . This is an important characteristics of atmospheric radars. Especially, the power aperture product  $P_t A_e$  is a common measure of the radars capability.

### 1.3 Phased antenna arrays

A phased antenna array is an array of spatially-distributed antennas with each element driven to make the constructive interference at the specific direction. Phased antenna arrays have great advantages over mechanically scanned antennas with a reflector; e.g., free of moving parts, rapid beam scanning, and controllable sidelobe characteristics using adaptive weighting of amplitude gains and phase shifts for each element. In this section, the basic principles of phased antenna arrays are presented.

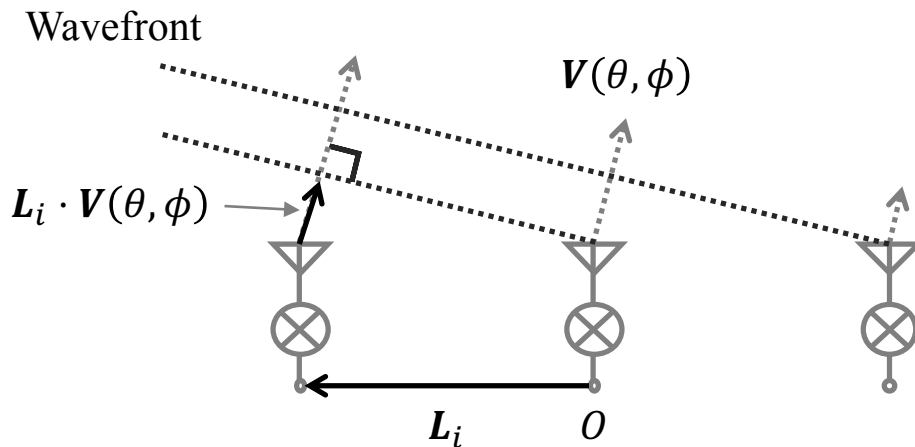


Figure 1.4: An example of phased array system.

### 1.3.1 Array manifold vector

Figure 1.4 is a schematic illustration of a phased array system.  $\mathbf{L}_i$  is the three-dimensional location of  $i$ -th antenna, and  $\mathbf{V}(\theta, \phi)$  is the radial unit vector in the desired direction  $(\theta, \phi)$ , where  $\theta$  and  $\phi$  are the zenith and azimuth angles for an arbitrary direction in three-dimensional space. Here, the azimuth angle is measured clockwise from the north. The wavefront in Fig. 1.4 is perpendicular to the looking direction  $(\theta, \phi)$ , and the electric field at this direction is coherent. The phase shifts to create such wavefronts are calculated by the normalized array manifold vector  $\mathbf{A}(\theta, \phi)$ . The  $i$ -th component of  $\mathbf{A}(\theta, \phi)$  is written as:

$$A_i(\theta, \phi) = \frac{1}{\sqrt{M}} \exp \left[ -j \frac{2\pi}{\lambda} \mathbf{L}_i \cdot \mathbf{V}(\theta, \phi) \right], \quad (1.19)$$

$$\mathbf{V}(\theta, \phi) = [\sin \theta \sin \phi, \sin \theta \cos \phi, \cos \theta]^T, \quad (1.20)$$

where  $M$  is the number of antennas,  $j$  is the imaginary unit, and  $(\cdot)^T$  denotes the transposition of a matrix. Note that Eq. (1.19) is also called the steering vector.

### 1.3.2 Nonadaptive beamforming

The narrowband beamforming output of a phased antenna array is generally written as:

$$Y = \mathbf{W}^H \mathbf{X}, \quad (1.21)$$

where  $\mathbf{X} = [X_1, X_2, \dots, X_M]^T$  is a complex time series for  $M$  spatially distributed antennas,  $\mathbf{W} = [W_1, W_2, \dots, W_M]^T$  is called a weight vector to change the amplitude and phase of the output signal of each receiver or antenna, and  $Y$  is the synthesized output. The notation  $(\cdot)^H$  represents the conjugate transposition of a matrix.

The weight vector to steer the main beam to the desired direction  $(\theta_o, \phi_o)$  can be calculated using Eq. (1.19):

$$\mathbf{W}_o = \mathbf{A}(\theta_o, \phi_o). \quad (1.22)$$

As in Eq. (1.22), the weight vector in this case is determined only by the geometrical positions of the receiver antennas, as well as the direction of the main beam. Thus, this operation is called nonadaptive beamforming.

### 1.3.3 Array factor and radiation pattern

As mentioned above, the direction in which the radio wave propagates can be controlled by the phase shift given by Eq. (1.19). However, undesired radiation also occurs at

almost all other directions, although the phase relationships in these directions do not make fully-constructive interference. Hence, the radiation pattern, or beam pattern, is an important characteristic of a phased antenna array that indicates how well the radiated power is concentrated to the desired direction.

To calculate the radiation pattern of a phased antenna array, the array factor  $F(\theta, \phi)$  is used, which is defined as follows:

$$F(\theta, \phi) = \mathbf{W}^H \mathbf{A}(\theta, \phi). \quad (1.23)$$

Note that Eq. (1.23) assumes all antenna elements to have the same omnidirectional antenna pattern. Otherwise, the generated electric field becomes a product of the element pattern  $E_e(\theta, \phi)$  and  $F(\theta, \phi)$ .

The far-field radiation pattern of a phased antenna array with the nonadaptive beamforming is calculated using Eqs. (1.22) and (1.23):

$$D(\theta, \phi; \theta_o, \phi_o) = |E_e(\theta, \phi) \mathbf{W}_o^H \mathbf{A}(\theta, \phi)|^2. \quad (1.24)$$

The weight vector  $\mathbf{W}_o$  can be calculated using either Eq. (1.22) or other adaptive beamforming techniques, e.g., those presented in section 1.7.

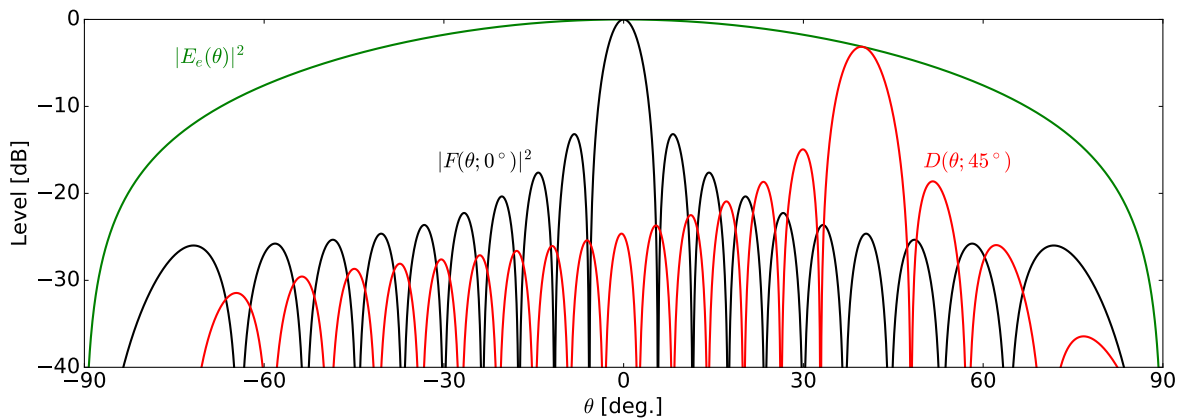


Figure 1.5: Example of array factor and radiation pattern.

Figure 1.5 shows an example of the broadside array factor and the radiation pattern of a 20-element uniform linear antenna array with equal spacing of half wave length. Each

antenna element is a half wavelength dipole antenna at the free space. This figure is a section at  $\phi = 0$ . The green line is the element pattern  $|E_e(\theta)|^2$ , the black line is the array factor  $F(\theta; 0^\circ)$ , and the red line is the total radiation pattern  $D(\theta; 45^\circ)$  with the steering direction  $\theta_o = 45^\circ$ . Note that element pattern and array factor are both normalized to 0 dB. As in Eq. (1.24), the total radiation pattern is the product of the element pattern and the array factor. This is also shown in Fig. 1.5, i.e., the radiation pattern of the array is weighted by the element pattern. This is called the law of pattern multiplication.

### 1.3.4 Calculation of element pattern

For more realistic cases presented in the next and following chapters, computation of the directional gain of each antenna is required to evaluate the total radiation pattern of an antenna array. Thus, the far-field element pattern of an antenna is calculated using the Numerical Electromagnetic Code (NEC). Actual implementation used in this thesis is NEC2++ (Molteni, 2014). Below is a brief explanation of NEC.

NEC solves the integral equations about the surface currents on wire or surface patch models. The basic methodology for solving these problems is the method of moments (MOM), which is classified into the finite element method (Harrington and Harrington, 1996). MOM first divides the surface of the original model into small-sized segments. Typically, the length of each segment is chosen so as to be less than  $0.1\lambda$  for enough accuracy (e.g., Rubinstein et al., 2006). On each small segment, the distribution of the surface current is approximated by a simple interpolating function, which is usually a piecewise sinusoidal function. By using this approximation, the integration can be calculated analytically, and the distribution of the surface currents is obtained. The far-field radiation pattern can easily be calculated from them.

In actual, above calculations are done using matrix inversion, and the dimensions of the matrix depend on the number of segments (Ferguson et al., 1976). Thus, MOM is usually used for models with dimensions of up to several wavelengths.

## 1.4 Atmospheric radar observation

Atmospheric radar is an instrument to observe wind velocities in clear air. Earth's atmosphere are commonly classified into four regions; from the bottom to top, troposphere, stratosphere, mesosphere, and thermosphere. The troposphere is the lowest region in the atmosphere from the ground to about 12 km in altitude. The stratosphere is the next region, up to 50 km. The mesosphere extends up to 90 km above the stratosphere. The sensitive radars capable of observing the radar returns from these three regions are called

mesosphere-stratosphere-troposphere (MST) radars. The primary echo sources in these regions are the irregularities of refractive index caused by atmospheric turbulences. MST radars observe the background winds using the motion of these turbulences as tracers.

The region above 80 km is called thermosphere. In this region, the air is so thin that atmospheric turbulences cannot be observed. However, this region is ionized by the solar radiation, and the electron density is higher than other regions. Thus, the backscattered signal from these free electrons, called incoherent scattering (IS), can be observed instead. Some powerful MST radars can observe this incoherent scattering, such as the middle-and-upper atmosphere (MU) radar mentioned in section 2.2.

The scattering theory in clear air turbulence was first investigated by Booker and Gordon (1950). Woodman and Guillen (1974) then confirmed the existence of atmospheric backscattered echoes in the stratosphere and mesosphere using the VHF-band pulse Doppler radar at the Jicamarca Radio Observatory. After that, the MST radar techniques rapidly evolved in 1970–1980s (e.g., Balsley and Gage, 1982; Gage and Balsley, 1978; Larsen and Röttger, 1982). This section provides an overview for the sources of the target signal, clutter, and noise for atmospheric radars.

### 1.4.1 Atmospheric echoes

The primary sources of atmospheric echoes in MST regions are the irregularities in refractive index caused by turbulences (Woodman and Guillen, 1974). The backscattering process is referred to as Bragg scattering. Below, a short explanation of Bragg scattering theory is presented, based on Fukao et al. (2014).

When radio waves transmitted from a radar are incident on the turbulent medium, the waves are scattered due to the irregularities of the refractive index. The refractive index in a medium at location  $\mathbf{l}$  is written as  $n(\mathbf{l})$ . The autocorrelation function  $N(\mathbf{r})$  with the displacement  $\mathbf{r}$  is given by:

$$N(\mathbf{r}) = \int n(\mathbf{l})n(\mathbf{l} + \mathbf{r})d\mathbf{l}. \quad (1.25)$$

The spatial distribution spectrum  $\hat{N}(\mathbf{k})$  is given by the Fourier transform of Eq. (1.25):

$$\hat{N}(\mathbf{k}) = \mathcal{F}[N(\mathbf{r})] = \frac{1}{(2\pi)^3} \iiint N(\mathbf{r})e^{-j\mathbf{k}\mathbf{r}}d\mathbf{r}, \quad (1.26)$$

where  $\mathbf{k} = \mathbf{k}_i - \mathbf{k}_s$  is the wave vector.  $\mathbf{k}_i$  and  $\mathbf{k}_s$  is the wave vectors of incident and scattered waves, and  $|\mathbf{k}_i| = k = 2\pi/\lambda$  is the wavenumber of the radar system. The average scattered power  $P_r$  is obtained using Eq. (1.26):

$$P_r = C \frac{k^4}{r^2} \hat{N}(\mathbf{k}), \quad (1.27)$$

where  $C$  is a constant determined by the radar system, and  $r$  is the distance to the radar volume. In backscattering case, the wave vectors of scattered and incident waves must have the relationship  $\mathbf{k}_s = -\mathbf{k}_i$ . Hence, the wave vector  $\mathbf{k}$  in Eq. (1.27) also has the relationship  $\mathbf{k} = 2\mathbf{k}_s$ . This condition implies that only the wave component with their wave number  $|\hat{\mathbf{k}}| = 2k = 4\pi/\lambda$  contributes to the scattering power in Bragg scattering. In common, MST radars use the frequencies in VHF band, because this corresponds to the ordinary scale of turbulent irregularities, i.e., 1 m to 10 m.

## 1.4.2 Clutter contamination

In atmospheric radars, suppression of clutter is critical in obtaining accurate measurements of wind velocities, especially for observing vertical air motion in the stratosphere and troposphere. Radial wind velocities are usually determined by taking the first moment of the spectrum of backscattered echoes. However, the returned atmospheric spectrum is contaminated by various clutter. Thus, by simply taking the moment of the observed spectrum, the estimated Doppler shift can contain severe biases. Below, the characteristics of typical clutter types are considered including the ground, aircraft, meteor, and FAI clutters. Clutter suppression techniques against them are also briefly introduced.

### Ground clutter

In the lower region of atmosphere, the primary source of the clutter is the ground surface. Aircrafts or birds can also become sources of the clutter (Chen et al., 2007). Figure 1.6 shows an example of the ground and aircraft clutter in ST region observed by the MU radar. Because sources of the ground clutter are stationary objects, the clutter spectrum exists in the zero Doppler component. In contrast, aircraft clutter usually has a wide spectrum because of their rapid motion; the typical speed of aircrafts are about  $250 \text{ m s}^{-1}$ . As mentioned in section 1.2.4, the maximum observable velocity without ambiguities depends on the slow time interval, which are usually chosen such that the maximum velocity becomes about  $30 \text{ m s}^{-1}$ . Thus, aircraft clutter contains severe Doppler aliasing as shown in Fig. 1.6. However, since the aircraft dwells in a range bin for a short time, rejection of aircraft clutter is not difficult, i.e., the affected data can simply be discarded. In contrast, the ground clutter semipermanently exists in almost all range bins, making its suppression the more critical for ground-based radars.

As mentioned above, the ground clutter exists mostly in the zero Doppler component of the observed spectrum. Thus, the ground clutter contamination can be mitigated by removing the zero Doppler component before taking the moments or performing the

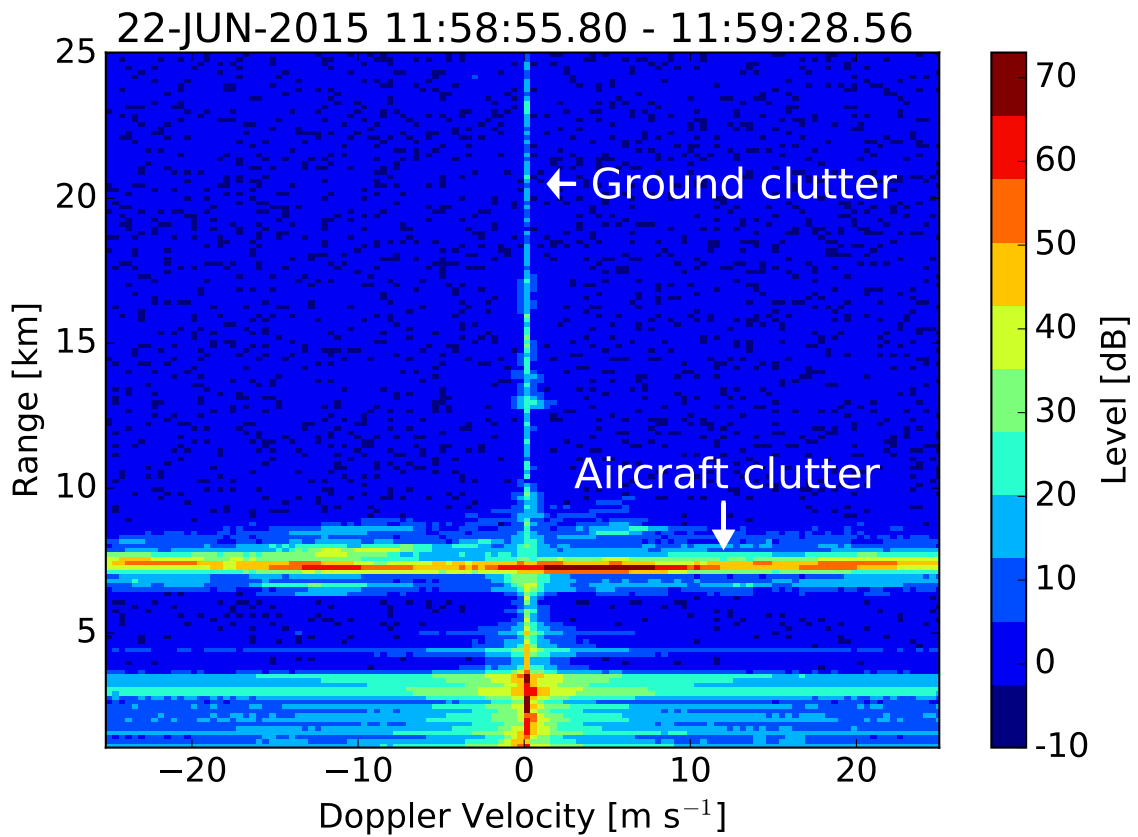


Figure 1.6: An example Doppler spectrum in ST region observed by the MU radar, containing the ground and aircraft clutter.

spectral fitting. However, the fading caused by the fluctuation along the pass of propagation, as well as the window function applied before the Fourier transform, can widen the clutter spectrum. Hence, modified fitting algorithm considering these fading effects also exists (Sato and Woodman, 1982). In weather radars, temporal high-pass filtering using regression or elliptic filters are also widely in use for moving target indication (MTI).

### Meteor trails

In mesosphere and ionosphere, meteor echoes are the major clutter. Meteorites are solid particles from the solar system which produce light when impinging on the Earth's atmosphere (Ceplecha et al., 1998). The meteor echoes are backscattered echoes originating

from meteorites, and can be categorized into two types; the head echo and trail echo.

Meteor head echo is thought as the backscattering from the ionized plasma surrounding the meteorite, although its nature is not fully understood yet. They are sometimes observed before the meteor trail, and their echo intensities are much weaker than the meteor trail echoes (Pellinen-Wannberg and Wannberg, 1994). Its velocity is initially the same as the meteorite (Hey et al., 1947; von Zahn and Hansen, 1988), e.g., between  $11.2 \text{ km s}^{-1}$  and  $72.8 \text{ km s}^{-1}$ . Hence, their dwell time in a radar range is very short, e.g., around 100 ms (Kero et al., 2012). Thus, simple data filtering can also be used to remove affected data by meteor head echoes like in the aircraft clutter.

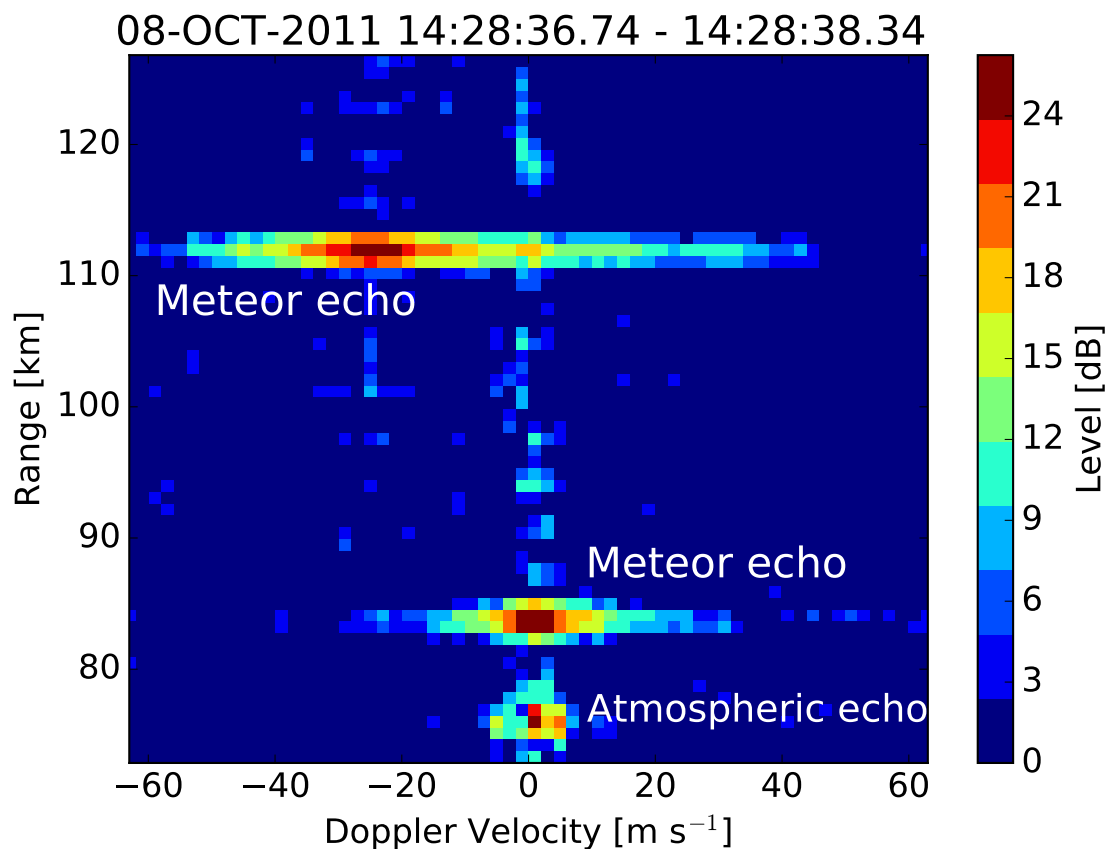


Figure 1.7: An example Doppler spectrum in mesosphere region observed by the MU radar, containing the meteor trail echoes.

Meteor trail echoes are returned from the ionized atmosphere along the pass of meteorites. Meteor trails can be considered as the linearly aligned ions and electrons, thus strongly backscatter the radio waves in a perpendicular direction. Figure 1.7 shows an example of the meteor trail echoes observed by the MU radar. Compared to the head echoes, these meteor trails have slower motion caused by the background wind. In addition, the duration of meteor trail echoes are much longer than that of the head echoes, reaching about a seconds (Ceplecha et al., 1998). Thus, the rejection of meteor trail clutter is an important subject for accurate measurement of wind velocity in middle atmosphere and IS observations in ionosphere. Again, simple data filtering can be used to remove data affected by meteor echoes, as in the aircraft clutter rejection in ST regions (Sato et al., 1989; Tsuda et al., 1985).

It should be noted that meteor echoes are also of important scientific interests. The velocity and direction of meteors can be estimated by observing the meteor head echoes using the pulse-to-pulse correlation (Kero et al., 2012), and background wind velocities can be estimated by using the meteor trails as tracers. Decay time of the intensity of meteor echoes can also be used to estimate the atmospheric temperature (Tsutsumi et al., 1994). Hence, the separation of the desired and other echoes, rather than simple suppression of undesired signals, is the more preferable solution in these cases. This is one of the motivations of using the adaptive beamforming techniques in the mesosphere observation (Hashimoto et al., 2014).

### **Field aligned irregularities**

Another possible application of adaptive beamforming is the incoherent scattering observation at the Syowa Station, Antarctic. Syowa Station has a large atmospheric radar called Program of Antarctic Syowa MST/IS (PANSY) radar (Sato et al., 2014). Detailed specifications of the PANSY radar is later mentioned in section 4.3. Besides the MST radar capability, the PANSY radar can observe the IS echoes in ionosphere region from about 100 km to 500 km. Strong coherent echoes from the field aligned irregularities (FAIs) are also observed in the same ranges at the Syowa station (Koustov et al., 2001; Ogawa, 1997). Figure 1.8 shows an illustration of the IS observation and the FAI echo contamination in the PANSY radar. The FAI echoes are observed at a direction where the line-of-sight is perpendicular to the geomagnetic field of the Earth, where auroral electrons are aligned by the Lorentz force. The elevation angles for these directions are about  $20^\circ$  for the PANSY radar. In the VHF band, the E-region FAIs satisfy the perpendicularity at the height of about 90 – 130 km. The distances to these points then become about 250 – 600 km, making the observation ranges of IS and FAI echoes overlapped.

Figure 1.9 shows the observed data from the PANSY radar in these high region. The

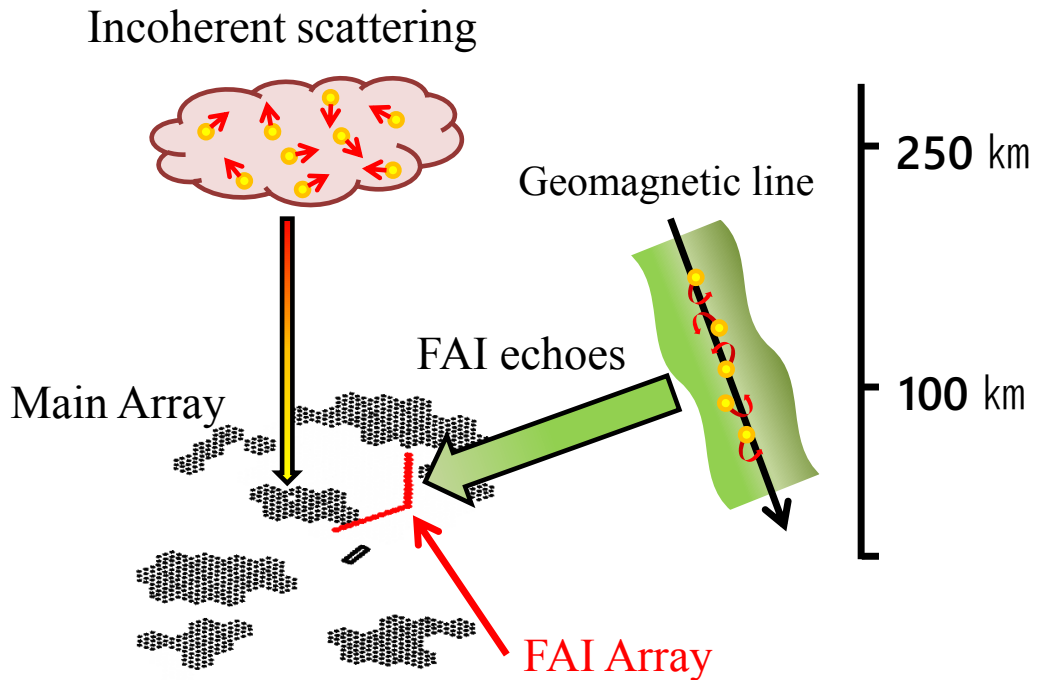


Figure 1.8: Illustration of the IS observation and the FAI echo contamination in the PANSY radar.

horizontal axis is the time, vertical axis is the range, and color indicates the echo intensity. Upper panel shows the incoherent scattering observed by the PANSY radar on May 15 2015 (around 300 km). It should be noted that this is the first IS observation of the PANSY radar, and in the Antarctic region. As in this panel, the coherent echoes from FAIs are not observed on this day. The lower panel shows the coherent FAI echoes in the same ranges observed on August 27 2015. The observation parameters are exactly the same. As in this panel, the intensity of the FAI echoes are much stronger than the IS signals to completely obscure them. The quasi-periodic structure of the E-region FAIs reported by Yamamoto et al. (1991) is also clearly seen in this figure.

Because both the IS and FAI echoes are of great interest for the polar atmospheric research, the separation of these echoes are necessary. For this purpose, the PANSY radar has a supplemental antenna array with 24 Yagi antennas directed at the geomagnetic south pole with the elevation angle of  $30^\circ$ , called the FAI array, as shown in Fig. 1.8. The detailed antenna arrangement and the pattern characteristics of the PANSY radar is presented in Figs. 4.4 and 4.5. Currently, the adaptive beamforming algorithm that uses the main and FAI array simultaneously is being studied. The partial adaptive array using

the gain-weighted constraints, which is presented in Chapter 3, is expected to become the breakthrough in this case.

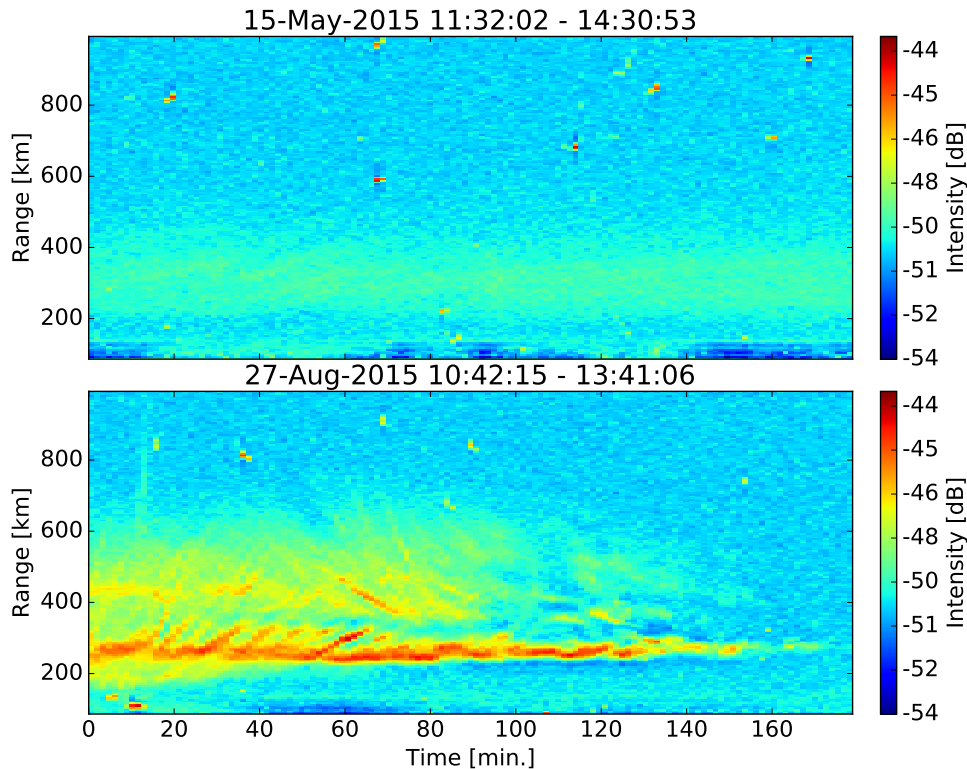


Figure 1.9: Range-time-intensity plot for the incoherent scattering (upper) and FAI echoes (lower) observed by the PANSY radar.

### 1.4.3 Galactic Noise

As mentioned in sections 1.4.1 and 1.4.2, atmospheric echoes are very weak and can be contaminated by various clutter. Another inevitable disturbance in the MST radar observation is the galactic noise, which is originating outside of the Earth's atmosphere. Its characteristics are similar to those of the thermal noise. However, they have much larger intensity at the VHF band, e.g., the noise temperature is usually more than 5000 K. The principal mechanism of the galactic noise is called synchrotron radiation, which is

caused by the relativistic electrons accelerated by the Lorentz force with strong magnetic field in interstellar medium. The frequency distribution of the synchrotron radiation is very wide, which is derived from the energy distribution of the electrons. However, due to the existence of ionized electrons in Earth's ionosphere, lower frequency components below about 10 MHz are reflected. Likewise, atmospheric attenuation becomes significant in higher frequencies above 1 GHz. Thus, the intensity of the galactic noise is frequency-dependent, and the VHF band, which is the common selection for the MST radars, is the most sensitive frequency band to it. The intensity of the galactic noise also has dependences on time due to the Earth's rotation and revolution and the radar beam direction, because particular regions in the sky have the more celestial objects that strongly emit radio waves, e.g., pulsars and quasars, compared with the other regions.

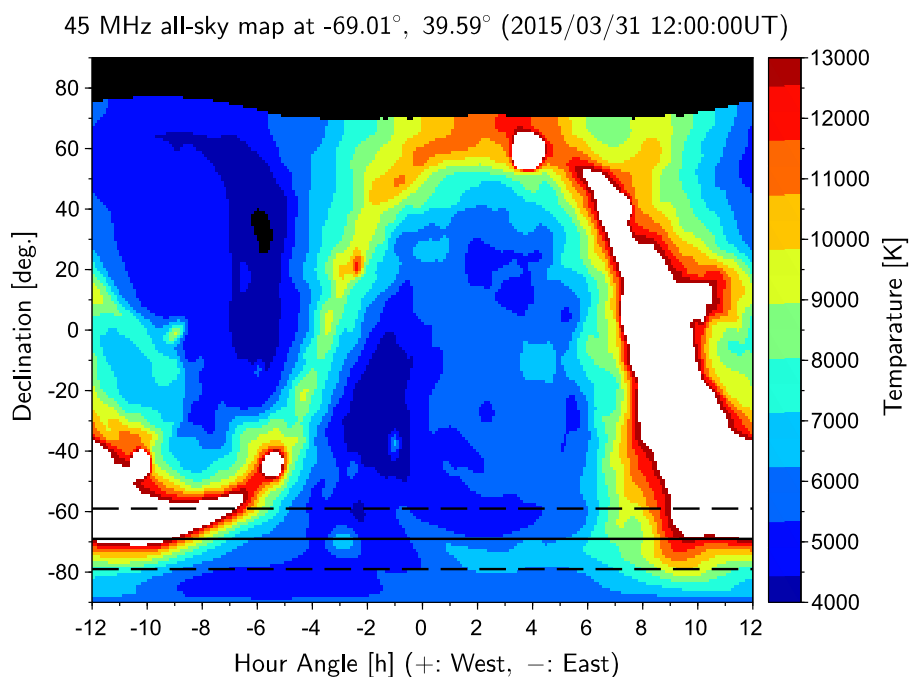
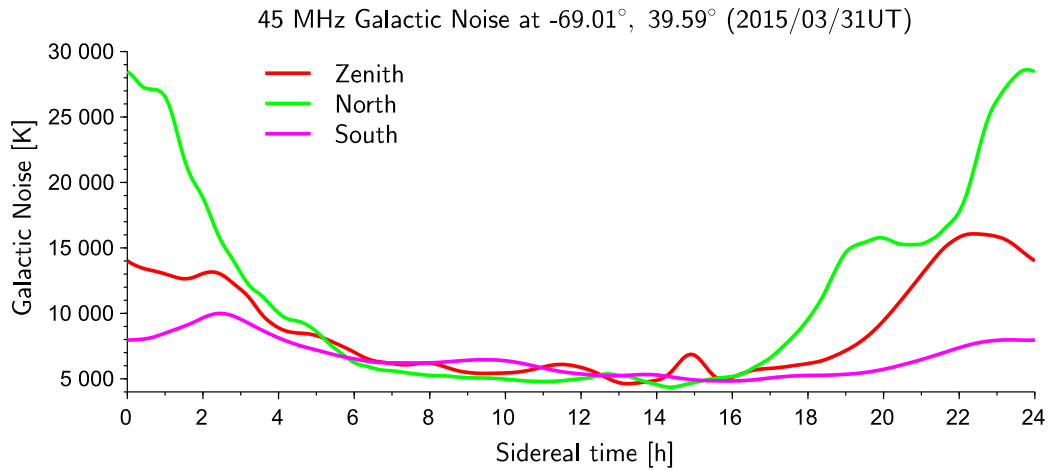


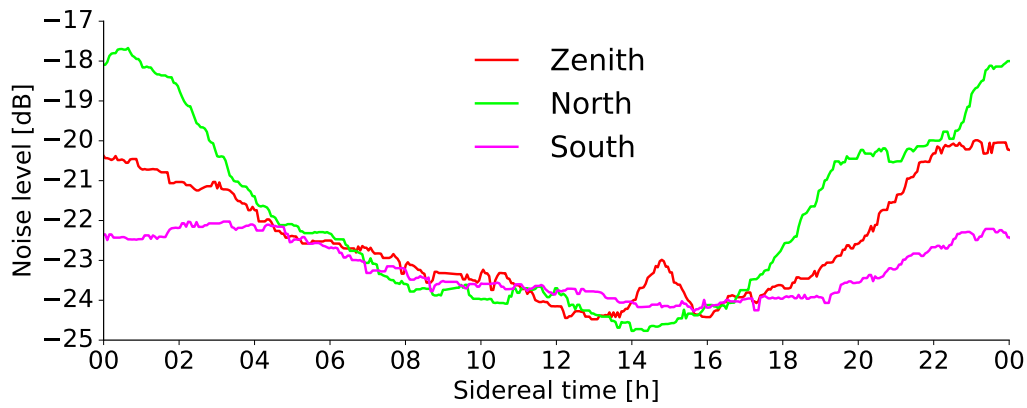
Figure 1.10: All-sky map of the galactic noise at 12:00 UTC (15:00 LT), March 31 2015. Modified after Guzmán et al. (2011).

The all-sky galactic radiation map in 45 MHz studied by Guzmán et al. (2011) clearly shows these variations. This map is created using two individual surveys; northern sky

map by Maeda et al. (1999), and southern sky map by Alvarez et al. (1997). These two surveys use instruments with similar characteristics; Maeda et al. (1999) uses the MU radar and Alvarez et al. (1997) uses the array at Maipú Radio Astronomy Observatory (May et al., 1984).



(a)



(b)

Figure 1.11: (a) Noise temperature extracted from Fig. 1.10, and (b) observed noise floor level for zenith, north, and south beams of the PANSY radar.

Figure 1.10 shows an example of the all-sky map of the galactic noise above the

PANSY radar at  $69.00^{\circ}\text{S}$ ,  $39.58^{\circ}\text{E}$ , on 12:00 UTC (15:00 LT), March 31 2015. As mentioned above, the galactic noise shows the temporal variation, thus requiring the specific date and time as well as the location of which the observation is made. The horizontal axis is the hour angle, which is defined as the difference between the local time and right ascension. Negative and positive values represent the time before and after passing above the radar, respectively. The vertical axis is the declination angle, and colors represent the noise temperature. White area is above 13 000 K, and black area is not covered in this map. A solid line parallel to the horizontal axis indicates the latitude of the PANSY radar, or equivalently, the pointing angle of the zenith beam. Upper and lower dashed lines around it are two off-vertical beam directions, north ( $+10^{\circ}$ ) and south ( $-10^{\circ}$ ), respectively. Figure 1.11a shows the noise temperatures extracted along with these three lines. The horizontal axis is the Greenwich sidereal time, which has an offset of about +34 min from UTC in this case. The vertical axis is the galactic noise temperature. Figure 1.11b shows the actual noise power observed by the PANSY radar for these beams. Each point is obtained by the average of about 92 s, and smoothed by the 5-point median filter to remove outliers. By comparing Figs. 1.11a and 1.11b, the observed noise power is consistent with the all-sky map by Guzmán et al. (2011). The small peak in the zenith beam at about 15:00 in these figures is from the supernova SN 1987A (Arnett et al., 1989).

Monitoring of the noise power is an important operation not only for the threshold to pick the weak atmospheric signals up from the noise floor, but also for the better understanding of the polar atmosphere and the health check of the radar system. For example, if the observed diurnal variation of the galactic noise power was strange, it may imply the existence of some solar events, exterior interference, or other system failure. The detailed estimation procedure of the noise power is given in section 1.5.4.

## **1.5 Wind velocity measurement using atmospheric Doppler radars**

The basic concept of the pulse Doppler radar is already mentioned in section 1.2. Here, actual procedure of data acquisition and signal processing on atmospheric radars are explained using Fig. 1.12.

### **1.5.1 Data acquisition and signal processing overview**

As mentioned in section 1.2, pulse Doppler radar periodically transmits the radio waves. The time interval between each consecutive pulse pair is called pulse repetition interval

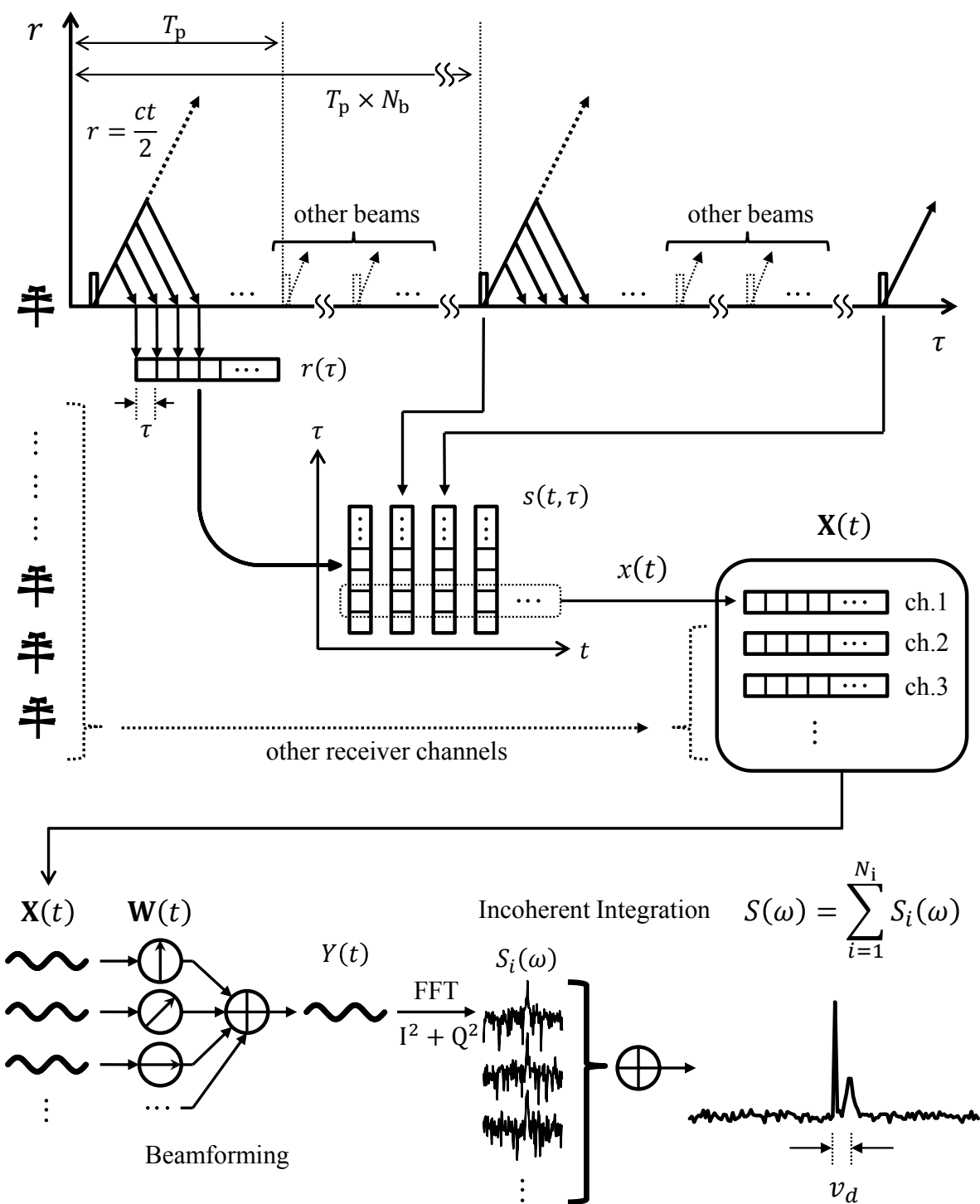


Figure 1.12: Schematic flow of data acquisition and signal processing of atmospheric radars to obtain the radial Doppler velocity.

(PRI) or inter pulse period (IPP), which is written as  $T_p$ . The transmitted radio wave travels by the speed of light, and backscattered in each range. After a pulse has been transmitted, receivers start sampling to observe backscattered echoes in each range, obtaining a range sequence  $r(\tau)$ . The sampling interval is equal to the pulse width  $\Delta T$ , which determines the range resolution  $\Delta r$ , as in Eq. (1.3). The maximum number of samples in  $r(\tau)$  is limited by IPP, because the acquisition of a range sequence  $r(\tau)$  must be finished before the next pulse is transmitted. Hence,  $\Delta r$ ,  $T_p$ , and  $N_h$  must be chosen to satisfy the following relationship:

$$r_{\max} = N_h \Delta r \leq \frac{c}{2} T_p, \quad (1.28)$$

where  $r_{\max}$  is the maximum observable distance.

As mentioned in section 1.2.4, the observed Doppler velocity shift using a pulse Doppler radar only contains the information about the radial component of the background wind along with the radar beam. Hence, to reconstruct the three-dimensional wind field, multiple-beam observation is generally used. In this case, the beam direction is changed in every IPP to ensure that the wind field is not changing among the beams. The range sequence  $r(\tau)$  in the same beam direction is thus taken by the interval of  $\Delta t = T_p N_b$  when the number of beams is  $N_b$ . Note that this is also effective on mitigating the range aliasing, because Tx and Rx beam patterns become different in succeeding pulses. A range-time matrix  $s(t, \tau)$  is then obtained by arranging  $N_t$  set of  $r(\tau)$  in the same beam direction, as in Fig. 1.12.  $s(t, \tau)$  has the size of  $N_t$  time points and  $N_h$  range points.  $\tau$  and  $t$  both have the dimensions of time, called fast time and slow time, respectively.

Modern atmospheric radars commonly have multiple receiver channels for the purpose of the adaptive beamforming. Because the beamforming is usually done in a range-by-range manner, time series extracted from a specific range,  $x(t)$ , is collected for each receiver channel to make the input signal matrix  $\mathbf{X}(t)$ , as in Fig. 1.12. The weight vector  $\mathbf{W}(t)$  is then applied to  $\mathbf{X}(t)$  using Eq. (1.21) to obtain the synthesized output  $Y(t)$ . Detailed adaptive beamforming methods are explained in section 1.7 and later chapters.

Finally, the power spectrum  $S(\omega)$  is estimated from  $Y(t)$ , and the spectral peak of the atmospheric echo is searched in the averaged spectrum to measure the radial Doppler velocity  $v_d$ . Detailed procedure of spectral processing is explained in the next section.

## 1.5.2 Power spectrum and periodogram

To obtain the mean Doppler frequency shift from the combined time series  $Y(t)$ , the Fourier transform of the received time-domain signal is generally used to obtain the

atmospheric power spectrum  $S(\omega)$  (e.g., Richards et al., 2010):

$$S(\omega) = |\mathcal{F}[Y(t)]|^2 = \left| \int_{-\infty}^{\infty} Y(t) e^{-j\omega t} dt \right|^2, \quad (1.29)$$

where  $\omega = 2\pi f$  is the Doppler angular frequency.

In reality, a finite time series is used in Eq. (1.29) to estimate the spectrum  $S(\omega)$ . The square of the Fourier transform using finite time series is called a periodogram. A periodogram generally has a large statistical fluctuation attributed to the noise. To decrease this fluctuation, the incoherent integration is commonly performed using  $N_i$  successive periodograms:

$$\bar{S}(\omega) = \frac{1}{N_i} \sum_{i=1}^{N_i} S_i(\omega). \quad (1.30)$$

Here, the amount of the fluctuation decreased by this incoherent integration is considered. The noise in both I and Q components can be assumed to follow the standard normal distribution. A periodogram is the sum of squares of both I and Q components, thus making it to follow the  $\chi^2$  distribution with two degrees of freedom. For the  $\chi^2$  distribution with  $k$  degrees of freedom, or written as  $\chi_k^2$  hereafter, the mean  $\mu_k$  and standard deviation  $\sigma_k$  are (e.g. Kay, 1998):

$$\mu_k = k, \quad \sigma_k = \sqrt{2k}. \quad (1.31)$$

Thus, both mean and standard deviation are 2 for  $k = 2$ . If  $N_i$  successive periodograms are added, the resultant periodogram follows  $\chi_{2N_i}^2$ . The mean and standard deviation in this case become  $\mu_{2N_i} = 2$  and  $\sigma_{2N_i} = 2/\sqrt{N_i}$  using Eq. (1.31) with the normalization by  $N_i$ . Compared with the standard deviation before the incoherent integration ( $\sigma_2 = 2$ ), the standard deviation of the noise is multiplied by  $1/\sqrt{N_i}$ . That is,  $N_i$ -time incoherent integration reduces the noise fluctuation by  $1/\sqrt{N_i}$  (Fukao et al., 1985a). On the other hand, the mean is unchanged after incoherent integration for the noise, while it is also the case for the peak of the desired signal. Therefore, the spectral peak height of the desired signal from the noise floor level is not changed by the incoherent integration. Instead, decreasing the fluctuation of noise enables the detection of small peaks which were obscured by noise before the incoherent integration. Sections 1.5.3 and 1.5.4 further discuss the detection of weak atmospheric signal from the Doppler spectrum.

### 1.5.3 Detectability

To find the weak signal which has the power close to noise, a threshold is needed to distinguish the desired signal and noise. In atmospheric radars, the detectability thresholding is generally used (Fukao et al., 2014; Gage and Balsley, 1978) to find the spectral

peak in the Doppler spectrum. The detectability is defined as the ratio between the peak height of the atmospheric spectrum and the standard deviation of the noise, or equivalently, the mean noise power  $P_N$ . The detectability threshold  $T_D$  after  $N_i$ -time incoherent integration is given by:

$$T_D = P_N \left(1 + D_t / \sqrt{N_i}\right), \quad (1.32)$$

where  $D_t$  is the detectability level. Using  $D_t = 3$  in Eq. (1.32) will assume those peaks in the periodogram with three times or more larger power spectral density than  $P_N$  to be valid echoes.

### 1.5.4 Noise floor level estimation

In detectability thresholding, the mean noise power  $P_N$  is required. It is also an important value in spectral fitting, because it can cause a bias without subtracting it from the observed power spectrum (Woodman, 1985). As in Eq. (1.31), the standard deviation and mean of random numbers following the  $\chi^2$  distribution can be converted to each other using the degrees of freedom. Therefore, the mean noise power spectral density  $P_N$  is first calculated from the observed periodogram. There are several approaches to do this.

#### Iterative algorithm

Algorithm proposed by Hildebrand and Sekhon (1974) iteratively decreases a threshold, and removes points in a periodogram which are larger than this threshold. At each iteration, the mean and variance are calculated using the remaining points of periodogram  $\omega_r$ , and are tested whether they satisfies the following equation:

$$R = \frac{\langle \bar{S}(\omega_r) \rangle^2}{N_i [\langle \bar{S}^2(\omega_r) \rangle - \langle \bar{S}(\omega_r) \rangle^2]} = 1, \quad (1.33)$$

because the ratio  $R$  between squared mean and variance of the noise spectrum after  $N_i$ -time incoherent integration theoretically equals to 1, as mentioned in section 1.5.2; see Eq. (1.31). Here,  $\langle (\cdot) \rangle$  denotes the ensemble average. The estimation of the noise power  $P_N$  can be obtained by  $\langle \bar{S}(\omega_r) \rangle$  using remaining periodogram points  $\omega_r$ .

This technique requires relatively a larger computational cost than the segment method below attributed to its iterative procedure. However, the obtained noise power is usually better estimation of the true value (Petitdidier et al., 1997). Thus, this technique is widely used in MST radars. Similar technique has been proposed by Urkowitz and Nesper (1992) which focuses on the flatness of the noise spectrum.

## Segment method

Another approach is called segment method proposed by Sato et al. (1989). First, the spectrum with  $N_i$ -time incoherent integration,  $\bar{S}(k_h, k_f)$ , is divided into equal-sized  $N_d$  segments including  $N_s = N_f/N_d$  points each, and the average power spectral densities of these segments are calculated, followed by selecting the lowest average power  $\hat{S}_m$  out of these segment-wise averages:

$$\hat{S}_m = \min_{k_h, k_d} \frac{1}{N_s} \sum_{k_s=1}^{N_s} \bar{S}(k_h, k_s + N_s(k_d - 1)), \quad (1.34)$$

for  $k_f = 1, \dots, N_f$ ,  $k_d = 1, \dots, N_d$ , and  $k_h = 1, \dots, N_h$ . By the procedure so far, the resultant minimum average  $\hat{S}_m$  is always an underestimation of the true noise level  $P_N$ . However, this can be corrected considering the probability of a random choice from a set being the minimum value (Tsuda, 1989). Suppose a population with its parameter  $p$  has the probability distribution function (PDF)  $\Phi(x)$  for random variables  $x$ . The probability of a sample  $x$  being the minimum value,  $\Psi(x)$ , can be written using the right-tail probability  $Q(x)$  of the PDF  $\Phi(x)$ :

$$Q(x) = \int_x^{\infty} \Phi(y) dy, \quad (1.35)$$

$$\Psi(x) = p [Q(x)]^{p-1} \Phi(x). \quad (1.36)$$

Here, factor  $p$  appears in Eq. (1.36), because there are  $p$  possible permutations.  $Q(x)$  in Eq. (1.35) can be interpreted as the probability of exceeding a given value  $x$ . The expectation value of Eq. (1.36),  $e$ , can be computed from the first moment of  $\Psi(x)$ :

$$e = \int_{-\infty}^{\infty} x \Psi(x) dx = \int_{-\infty}^{\infty} p x [Q(x)]^{p-1} \Phi(x) dx. \quad (1.37)$$

In the current case, the PDF  $\Phi(x)$  follows the  $\chi^2$  distribution with  $2\nu$  degrees of freedom, where  $\nu = N_i N_s$ . The PDF  $\Phi(x)$  and its right-tail probability  $Q(x)$  is then written as (e.g., Kay, 1998):

$$\Phi(x) = \frac{1}{2^\nu \Gamma(\nu)} x^{\nu-1} \exp\left(-\frac{1}{2}x\right), \quad (1.38)$$

$$Q(x) = \exp\left(-\frac{1}{2}x\right) \sum_{k=0}^{\nu-1} \frac{\left(\frac{x}{2}\right)^k}{k!}, \quad (1.39)$$

for  $x > 0$ . Function  $\Gamma(x)$  is the Gamma function, which is defined as:

$$\Gamma(x) = \int_0^{\infty} z^{x-1} \exp(-z) dz. \quad (1.40)$$

Substituting Eqs. (1.38) and (1.39) into Eq. (1.37) yields the theoretical expectation value of the minimum for  $\chi_{2\nu}^2$ , or  $e_{2\nu}$ . On the other hand, the theoretical mean for  $\chi_{2\nu}^2$  is  $\mu_{2\nu} = 2\nu$ , as in Eq. (1.31). Therefore, using  $e_{2\nu}$  and  $\mu_{2\nu}$  as the correction factors, the true noise level  $P_N$  can be calculated from the minimum value of the block-wise average  $\hat{S}_m$ :

$$P_N = \frac{\mu_{2\nu}}{e_{2\nu}} \hat{S}_m = \frac{2\nu}{e_{2\nu}} \hat{S}_m. \quad (1.41)$$

The clear advantage of this segment method is the smaller calculation cost compared with the iterative algorithm by Hildebrand and Sekhon (1974). As in Eq. (1.34), the calculation of  $\hat{S}_m$  requires only fixed number of steps. In addition, the correction factor  $e_{2\nu}$  only depends on the observational settings; the number of incoherent integration and points in each segment,  $N_i$  and  $N_s$ , respectively. Therefore,  $e_{2\nu}$  is calculated only once at the beginning of the observation, enabling the estimation of  $P_N$  by the simple block-wise average and a single multiplication in Eq. (1.41).

To further decrease the calculation complexity, Sato et al. (1989) used an additional approximation on  $\Phi(x)$ , i.e., for sufficiently large  $\nu$ ,  $\Phi(x)$  can be approximated to the Gaussian distribution with its mean and standard deviation properly normalized. With this approximation, the noise power can be estimated using the expected minimum value  $e'$  of this Gaussian approximated PDF instead of  $e_{2\nu}$ . Figure 1.13 shows an example of the Gaussian approximation of the  $\chi^2$  distribution. The black solid line is the PDF of the  $\chi_{224}^2$ , and the red solid line is the Gaussian-approximated PDF  $\mathcal{N}(224, \sqrt{448})$ , which is the normal distribution with its mean 224 and standard deviation  $\sqrt{448}$ . Note that this setting frequently appears in the standard observations of the MU radar. The black and red dashed lines are  $\chi_{32}^2$  and  $\mathcal{N}(32, \sqrt{64})$ , respectively. This corresponds to the case when the number of incoherent integration is 1/7 times of  $\chi_{224}^2$ , and a larger approximation error can be seen compared to  $\chi_{224}^2$ . As shown by this figure, the  $\chi_{2\nu}^2$  can be approximated by  $\mathcal{N}(2\nu, 2\sqrt{\nu})$  when  $\nu$  is sufficiently large.

To compute  $e'$ , the standard normal distribution  $\mathcal{N}(0, 1)$  is first considered. In this case, the right-tail probability function  $Q(x)$  can be simplified to (e.g., Kay, 1998):

$$Q(x) = \frac{1}{2} \left[ 1 - \operatorname{erf} \left( \frac{x}{\sqrt{2}} \right) \right]. \quad (1.42)$$

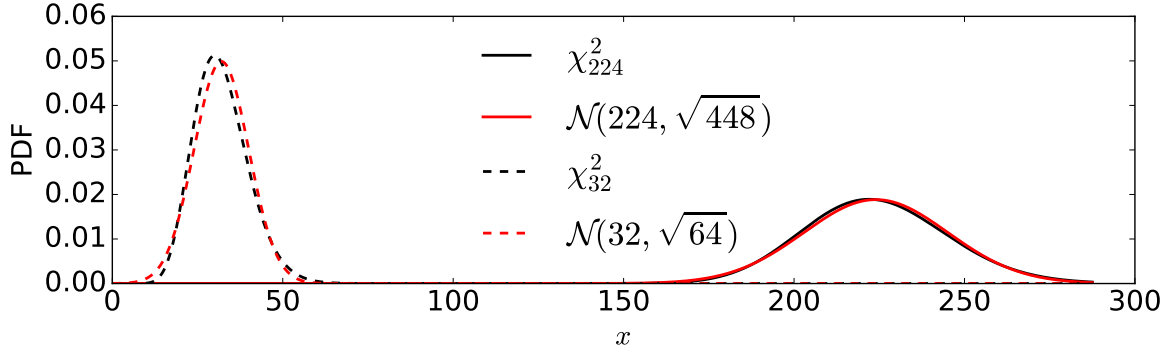


Figure 1.13: An example of the Gaussian approximation for  $\chi^2$  distribution.

Here, function  $\text{erf}(x)$  is the error function, which is defined as:

$$\text{erf}(x) = \frac{2}{\sqrt{\pi}} \int_0^x \exp(-y^2) dy. \quad (1.43)$$

Clearly, the probability of a random value  $e_{0,1} \sim \mathcal{N}(0, 1)$  being the maximum of the population with parameter  $p$  satisfies the following equation:

$$Q(e_{0,1}) = \frac{1}{2} \left[ 1 - \text{erf} \left( \frac{e_{0,1}}{\sqrt{2}} \right) \right] = \frac{1}{p}. \quad (1.44)$$

By solving Eq. (1.44), the expected maximum value  $e_{0,1}$  is obtained. The expected minimum value of  $\mathcal{N}(0, 1)$  is then  $-e_{0,1}$ , because  $\mathcal{N}(0, 1)$  is a symmetric PDF.  $e'$  is then computed as:

$$e' = -2\sqrt{v}e_{0,1} + 2v. \quad (1.45)$$

Substituting  $e'$  in Eq. (1.41) instead of  $e_{2v}$  yields:

$$P_N = \frac{1}{1 - e_{0,1}/\sqrt{v}} \hat{S}_m. \quad (1.46)$$

This is the noise level estimation of the Gaussian-approximated segment method.

As Petitdidier et al. (1997) pointed, however, the Gaussian approximation can be violated for small  $v$ , causing larger biases compared with the iterative algorithm by Hildebrand and Sekhon (1974). To see the accuracy of this approximation, a comparison was made on two implementations of the segment method; strict estimation using Eqs. (1.37) to (1.39), ‘‘Strict’’, and Gaussian approximation in Sato et al. (1989), ‘‘Gaussian’’. Table 1.1 shows the three situations used in this simulation. Case A is based on the standard

observation in ST region of the MU radar. Case B and C have a different number of range points  $N_h = 1$ , or incoherent integration  $N_i = 1$ , respectively, compared with the case A. In this comparison, 100 Monte Carlo simulations are carried out. For each evaluation, a simulated noise spectrum is first generated using random variables following the  $\chi^2$  distribution according to the parameters in Table 1.1. Strict and Gaussian-approximated segment methods are then applied to the generated noise spectrum to estimate the noise power.

Table 1.1: Three test cases used in the simulation. These are based on the standard observation of the MU radar.

Case	$N_f$	$N_h$	$N_i$	$N_d$	$N_s$	$2N_iN_s$	$N_dN_h$
A	128	100	7	8	16	224	800
B	128	1	7	8	16	224	8
C	128	100	1	8	16	32	800

Table 1.2: Comparison of the strict and Gaussian-approximated segment methods.  $a \pm b$  denotes mean  $a$  and standard deviation  $b$ . Cases are defined in Table 1.1.

Case	Truth	Strict	Gaussian
A	14	$13.9 \pm 0.6$	$14.6 \pm 0.6$
B	14	$14.0 \pm 0.8$	$14.5 \pm 0.8$
C	2	$1.96 \pm 0.2$	$3.68 \pm 0.5$

Table 1.2 summarizes the results. In cases A and B, the degrees of freedom of the underlying  $\chi^2$  distribution in averaged segments are 224. As in Table 1.2, the Gaussian approximation by Sato et al. (1989) is enough accurate in these cases, although the strict one gives slightly better estimations. Hence, the variation in population parameter,  $N_hN_d$ , seems not dominant between these two cases. This implies that after enough number of incoherent integration, the Gaussian approximation can safely be applied even in range-by-range manner, which is a consistent result with that in Petitdidier et al.

(1997). However, results in Table 1.2 are based on the spectrum only containing the noise, and not every range gate can be assumed to have an enough number of “clean” segments, i.e., without atmospheric, clutter, or other interference spectrum. Therefore, range-wise estimation as in case B should be avoided in actual observed spectrum. In case C, the estimated noise power is severely biased using the Gaussian-approximated segment method, while correct using the strict one. This is naturally understood with the approximation error of  $\chi_{32}^2$  shown in Fig. 1.13.

From these results, it can be concluded that the strict segment method can be applied in the wider range of the situations than that using Gaussian approximation. Since the calculation cost of  $e_{2v}$  using Eqs. (1.37) to (1.39) should never be a problem on modern computers, the strict segment method is used in this thesis.

### 1.5.5 Estimation of radial Doppler velocity

The mean Doppler angular frequency shift  $v_d$  can be obtained, for example, by taking the first moment of the spectrum of backscattered echoes (Woodman, 1985; Zrnic, 1979):

$$P_r = \int_{-\infty}^{\infty} \bar{S}(v) dv, \quad (1.47)$$

$$v_d = \frac{1}{P_r} \int_{-\infty}^{\infty} v \bar{S}(v) dv, \quad (1.48)$$

where  $v = -4\pi\omega/\lambda$  is the Doppler velocity (see Eq. (1.8)) and  $P_r$  is the zero-th moment of the power spectrum, i.e., the received echo power. Note that the noise power  $P_N$  is estimated employing the segment method in section 1.5.4 and subtracted from  $\bar{S}(v)$  in advance.

Another technique for estimating the mean Doppler velocity is the spectral fitting. In this thesis, the least-squares fitting method is used (Sato and Woodman, 1982; Yamamoto et al., 1988). This method fits a Gaussian spectrum model to the observed spectrum  $\bar{S}(v)$ . The model spectrum  $S'(v; P_s, v_d, \sigma_d)$  is written as:

$$S'(v; P_s, v_d, \sigma_d) = \frac{P_s}{\sqrt{2\pi}\sigma_d} \exp\left[-\frac{(v - v_d)^2}{2\sigma_d^2}\right], \quad (1.49)$$

where  $v$  is the radial wind velocity,  $P_s$  is the echo intensity of the atmospheric echo,  $P_N$  is the noise floor level,  $v_d$  is the mean Doppler velocity of the wind, and  $\sigma_d$  is the spectral width. The fitting procedure is done by finding a set of  $P_s$ ,  $v_d$ , and  $\sigma_d$  such that the root-mean-square (RMS) of the residue between  $S'(v; P_s, v_d, \sigma_d)$  and  $S(v)$  is minimized:

$$P_s, v_d, \sigma_d = \operatorname{argmin}_{P_s, v_d, \sigma_d} \sqrt{\sum_v [\hat{S}(v) - S'(v; P_s, v_d, \sigma_d) - P_N]^2}. \quad (1.50)$$

## 1.5.6 3-D wind field measurement

To evaluate the horizontal wind velocity, the Doppler beam swing (DBS) method can be used. The technique is also called velocity azimuth display (VAD) method in weather radars using rotating dish antennas (Browning and Wexler, 1968). Figure 1.14 illustrates the schematic example of the DBS method applied on a phased array. As shown in Fig. 1.14, five beam directions are usually used when applied to the phased arrays: zenith (Z), north (N), east (E), west (W), and south (S). The DBS method collects the radial Doppler velocities over all the steered beams to reconstruct the 3-D wind field in the scanned volume. Note that the vertical wind velocity obtained by the zenith beam is also used in the horizontal wind velocity estimation to remove the contamination of the vertical wind component into the horizontal winds (Strauch et al., 1987). To apply the DBS method, the radar beam width must be sufficiently narrow, and the beam scanning for multiple beams must be finished in a sufficiently short time; otherwise, the observed Doppler velocity will become the sum of the various wind components in the radar volume illuminated by the wide beam, and the wind field may be changed while scanning the beam, resulting in an inaccurate estimation of wind field (Fukao et al., 2014).

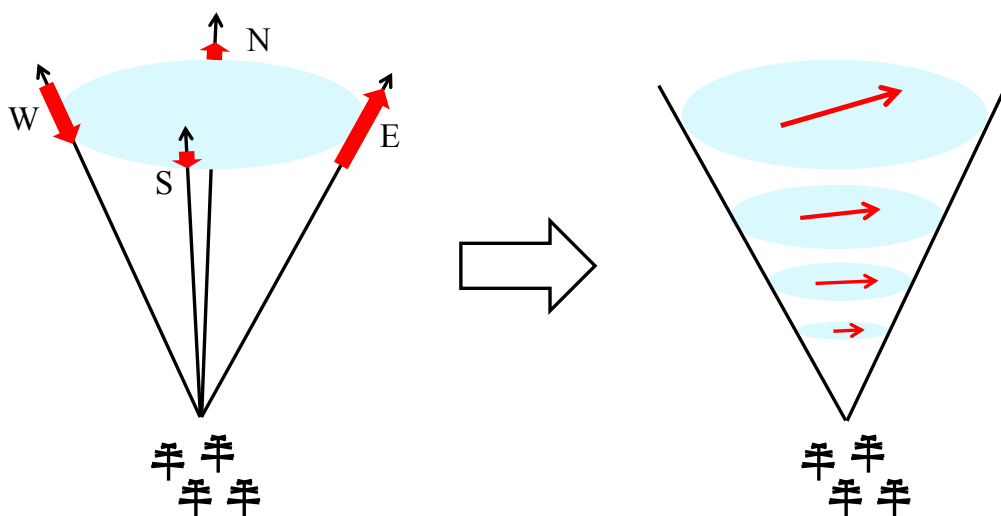


Figure 1.14: Illustration of the Doppler beam swing method for phased arrays.

## 1.6 Conventional clutter suppression techniques for atmospheric radars

In this section, various conventional clutter suppression techniques are reviewed, including MTI processing, Doppler spectral filtering, and nonlinear fitting using models of atmospheric and clutter spectra.

### 1.6.1 Moving target indication

Moving target indication (MTI) is a radar operation to detect a moving target under stationary clutter interference. MTI processing generally applies a time-domain high-pass filter to the observed signal. The filtered data are then passed to the amplitude thresholding process to detect the existence of the target. Hence, neither discrimination of multiple targets nor estimation of the target's velocity can be done through the pure MTI processing (Richards et al., 2010). Similar ground clutter suppression techniques using time-domain high-pass filter is widely used in weather radars. In this case, the MTI filter is first applied to suppress the ground clutter. Afterwards, the received signal is converted to the spectrum to estimate the wind parameters.

MTI filter is usually a simple finite or infinite impulse response (FIR or IIR) filter. For example, the operational meteorological radar in the United States, WSR-88D, uses a fifth-order elliptic IIR filter for the ground clutter suppression (Crum et al., 1993; Heiss et al., 1990). The regression filter is also used to improve the frequency response (Torres and Zrnica, 1999).

As mentioned above, the MTI filter cuts the frequencies near the zero Doppler component. However, this may also lose the desired weather echoes that have the radial velocities close to zero. Hence, a decision of applying the clutter filter is first made using the echo characteristics in the modern weather radar (Hubbert et al., 2009). This procedure is called clutter mitigation decision (CMD) algorithm. The CMD algorithm checks the fluctuation and discontinuity of the echo intensity between adjacent range gates and beams. The fluctuation of the phase is also used, since the ground clutter has relatively slow phase rotation. The MTI clutter filter is then applied only to ranges and beams those determined by the CMD algorithm.

### 1.6.2 Pulse Doppler processing

In atmospheric radars and wind profilers using pulse Doppler radar system, the ground clutter suppression is usually done in the frequency domain. The simplest way is to replace the zero Doppler component of the observed spectrum by the average of those in

both adjacent bins range by range (May and Strauch, 1998). This procedure is used in, for example, the operational wind profiler network in Japan, called wind profiler network and data acquisition system (WINDAS) (Ishihara et al., 2006). Similar technique is also routinely used as a part of spectral fitting algorithm in the MU radar (Fukao et al., 1985a,b), and the PANSY radar (Sato et al., 2014). In this case, the radial wind velocity is estimated by the least-squares fitting method without the zero Doppler component when computing the residual errors (Yamamoto et al., 1988).

The problem of this method is that they cannot distinguish the clutter and the actual atmospheric spectrum that happens to be close to zero Doppler component. This can cause biases especially in estimating zonal wind velocities. Typically, vertical wind velocity is very small, e.g., mostly about  $0.4 \text{ m s}^{-1}$  in the PANSY radar (Sato et al., 2014) in the ST region. Since the resolution of the Doppler velocity is comparable to this value, the peak of the atmospheric spectrum mostly exists at the zero Doppler component. Hence, such a simple filtering can cause biases to the peak position depending on the values of adjacent bins in the spectrum. This is the motivation of the use of adaptive beamforming techniques on clutter suppression.

## 1.7 Clutter suppression techniques using adaptive beamforming

Recently, phased array has been widely used for the antenna structures of atmospheric radars. Phased antenna arrays have a number of advantages compared with antennas having mechanical scanning, e.g., rapid beam steering, as mentioned in section 1.3. In particular, by dividing the array into multiple subgroups, one can use adaptive beamforming techniques to mitigate clutter contamination. As mentioned in the previous section, temporal or spectral filtering can cause biases, especially in vertical wind measurements, because they cannot distinguish the atmospheric spectrum and clutter spectrum in zero Doppler components. In contrast, adaptive beamforming techniques use the spatial distribution of targets. The desired signal of atmospheric backscattering is considered to come only from the beam pointing direction, i.e., near the zenith. On the other hand, clutter signals are usually at low elevation angles. Adaptive beamforming can distinguish signals from these different directions, and improve the accuracy of vertical wind velocity measurements (Kamio and Sato, 2004; Nishimura et al., 2012). In this section, basic methodologies of the adaptive beamforming are introduced.

### 1.7.1 Directionally constrained minimization of power

The DCMP algorithm is an adaptive beamforming method that minimizes the average output power under the constraint of the desired direction (Capon, 1969; Takao et al., 1976). The DCMP algorithm can be written as a convex optimization problem:

$$\underset{\mathbf{W}}{\text{minimize}} \quad \mathbf{W}^H \mathbf{R} \mathbf{W} \quad \text{subject to} \quad \mathbf{C}^H \mathbf{W} = 1, \quad (1.51)$$

where  $\mathbf{R} = E[\mathbf{X}\mathbf{X}^H]$  is the covariance matrix and  $\mathbf{C}$  is the directional constraint.  $\mathbf{C}$  is usually calculated using Eq. (1.19) with the desired direction  $(\theta_o, \phi_o)$ , i.e.,  $\mathbf{C} = \mathbf{A}(\theta_o, \phi_o)$ , assuming a uniform power directional gain for each channel. The solution to Eq. (1.51) is given in the following section.

The DCMP algorithm is quite often used for adaptive clutter rejection because of its simplicity and effectiveness. However, the major problem of this method is that the obtained beam pattern can have large sidelobes, and their levels are uncontrollable. The reception beam direction may also be largely changed to suppress clutter, leading to a severe degradation in the signal-to-noise ratio (SNR), as well as the error in estimating the wind velocity using the DBS method. This is because the beam pattern can be modified without changing the response to the desired direction as illustrated in Fig. 1.15. The beam direction is largely changed although the response to the desired direction is kept at a constant, causing a large beam directional error without the loss of the desired signal power, especially when the desired signal source is a point-like target. These problematic points of the DCMP algorithm are further discussed in section 4.2.

### 1.7.2 Norm-constrained DCMP algorithm

As mentioned in section 1.7.1, the DCMP algorithm causes severe SNR degradations in various situations, e.g., using poorly estimated covariance matrices, using wrong steering vectors, or when applied to high SNR signals. Thus, to control the amount of SNR degradation, the norm-constrained DCMP (NC-DCMP) algorithm has been introduced (Cox et al., 1987; Hudson, 1981). The NC-DCMP algorithm is a modified DCMP that adds to Eq. (1.51) the constraint:

$$\|\mathbf{W}\|^2 \leq U, \quad (1.52)$$

where  $\|(\cdot)\|$  denotes the Euclidean norm and  $U$  is the norm constraint. This method is known to be effective in actual observations from the MU radar at Shigaraki, Japan (Hashimoto et al., 2016, 2014; Kamio and Sato, 2004; Nishimura et al., 2012). More recently, Curtis et al. (2016) applied the same algorithm to observations from the National Weather Radar Testbed Phased Array Radar.

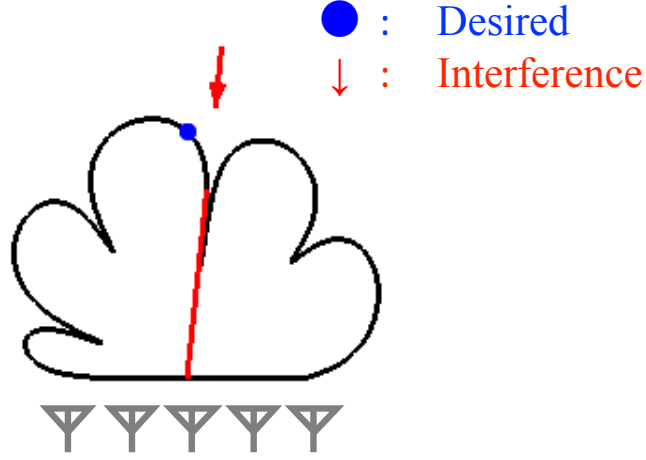


Figure 1.15: Beam directional error in the DCMP algorithm.

Although it is generally difficult to determine  $U$ , Kamio et al. (2004) showed that  $U$  can be computed from the permissible SNR degradation caused by signal processing. Ideally, the desired signal is assumed to be unchanged by the DCMP algorithm. However, the average noise power is multiplied by  $\|\mathbf{W}\|^2$ , because the primary noise source in VHF band is galactic noise, which is random and independent of the antenna gain. Therefore, the SNR degradation factor  $L_{\text{SNR}}$  given by the standard DCMP algorithm is written as:

$$L_{\text{SNR}} = \frac{1}{\|\mathbf{W}\|^2}. \quad (1.53)$$

Thus, to limit the SNR degradation to within  $L_{\text{dB}}$  dB,  $U$  can be set to  $U = 10^{-L_{\text{dB}}/10}$ .  $L_{\text{dB}}$  is usually set to a small value, such as  $L_{\text{dB}} = 0.5$  dB (corresponding to  $U \sim 1.12$ ), which allows the algorithm to suppress the clutter at the cost of a SNR degradation of less than 0.5 dB.

The optimal weight vector for the NC-DCMP algorithm can be obtained using the Lagrange multiplier and diagonal-loading technique:

$$\mathbf{W}(\alpha) = \frac{(\mathbf{R} + \alpha \mathbf{I})^{-1} \mathbf{C}}{\mathbf{C}^H (\mathbf{R} + \alpha \mathbf{I})^{-1} \mathbf{C}}, \quad (1.54)$$

where  $\alpha$  is the diagonal-loading value and  $\mathbf{I}$  is the identity matrix. Note that  $\alpha = 0$  gives the solution to the DCMP algorithm in Eq. (1.51). As  $\|\mathbf{W}\|^2$  decreases monotonically as  $\alpha$  increases, the optimal  $\alpha$  for the NC-DCMP algorithm is calculated as follows (Nishimura et al., 2012):

1. Set  $\alpha$  to a small value.
2. Calculate  $\mathbf{W}$  using Eq. (1.54). If  $f(\alpha) = \|\mathbf{W}\|^2 - U \leq 0$  is satisfied, then this is the solution.
3. Otherwise, increase  $\alpha$  and go to step 2.

Note that the analytical gradient of  $f(\alpha)$  can be calculated as:

$$\frac{\partial f(\alpha)}{\partial \alpha} = \frac{\partial \mathbf{W}^H}{\partial \alpha} \mathbf{W} + \mathbf{W}^H \frac{\partial \mathbf{W}}{\partial \alpha}, \quad (1.55)$$

$$\frac{\partial \mathbf{W}}{\partial \alpha} = (\mathbf{W}\mathbf{C}^H - \mathbf{I})(\mathbf{R} + \alpha\mathbf{I})^{-1}\mathbf{W}. \quad (1.56)$$

The problem with the NC-DCMP algorithm is that the selection of the user-defined parameter  $L_{\text{dB}}$  is empirical. For example, Nishimura et al. (2012) used  $U = 1.2, 1.5,$  and  $2.0$ , which correspond to the permissible SNR degradations having  $L_{\text{dB}} = 0.79, 1.76,$  and  $3$  dB. As they pointed out, this parameter depends on the electromagnetic environment around the radar system, i.e., the background noise level, clutter characteristics, and power directionality of the antennas. In addition, these conditions also vary for each range, making selection of the norm constraint difficult. Therefore, adaptive determination of the diagonal loading value using the observed data has been desired. This is the motivation of the work presented in Chapter 4.

## 1.8 Organization of this thesis

So far, the fundamentals of pulse Doppler radar, phased antenna array, and the basics of the signal processing techniques for atmospheric radars are reviewed, followed by the explanation of clutter suppression techniques including adaptive beamforming.

The remaining part of this thesis is organized into four chapters. In Chapter 2, an example of applying the adaptive beamforming techniques to the mesosphere wind observations of the MU radar is presented. In Chapter 3, the optimal array design for atmospheric radars with adaptive beamforming is discussed. In Chapter 4, a novel adaptive ground clutter suppression algorithm for atmospheric radars is presented. Finally, in Chapter 5, the results are summarized and concluding remarks are made.

# Chapter 2

## Meteor clutter rejection and accurate measurement of the wind velocity in Mesosphere

### 2.1 Introduction

As mentioned in section 1.4.2, strong meteor echoes often contaminate spectra in observations of mesosphere wind employing Doppler radars. Meteor trail echoes are returned from ionized electrons left along the paths of meteoroids. These trails usually remain at most a second with 50 MHz and provide strong backscattering. For example, the echo power from these trails may reach 80 dB over the noise level (McKinley, 1961). In radar observations of the mesosphere, successive spectra are usually averaged to reduce statistical fluctuations. Although these meteor trails fade out in less than a second, their strong intensity contaminates the spectra severely even after the incoherent integration. Thus, these spectra with meteor echoes are usually automatically detected by their discontinuity in time and height and are discarded before the incoherent integration and wind velocity estimation are made (Tsuda et al., 1985). However, only outstanding echoes can be removed employing this method. Additionally, decreasing the number of spectra for incoherent integration increases the fluctuations of spectra, which introduces estimation errors of the wind velocity of weak mesosphere echoes.

In this chapter, the NC-DCMP algorithm is applied to the mesosphere wind observations to reduce interference from meteor trail echoes. As mentioned in section 1.7.2, the NC-DCMP algorithm has been shown to be a good solution for the rejection of interference from the ground and accurate estimation of the vertical wind velocity (Nishimura et al., 2012). However, this is not the case for rapidly moving objects such as aircraft. Meteor trail echoes are also moving objects and have strong echo intensity, but they are relatively slow and the method works well for them.

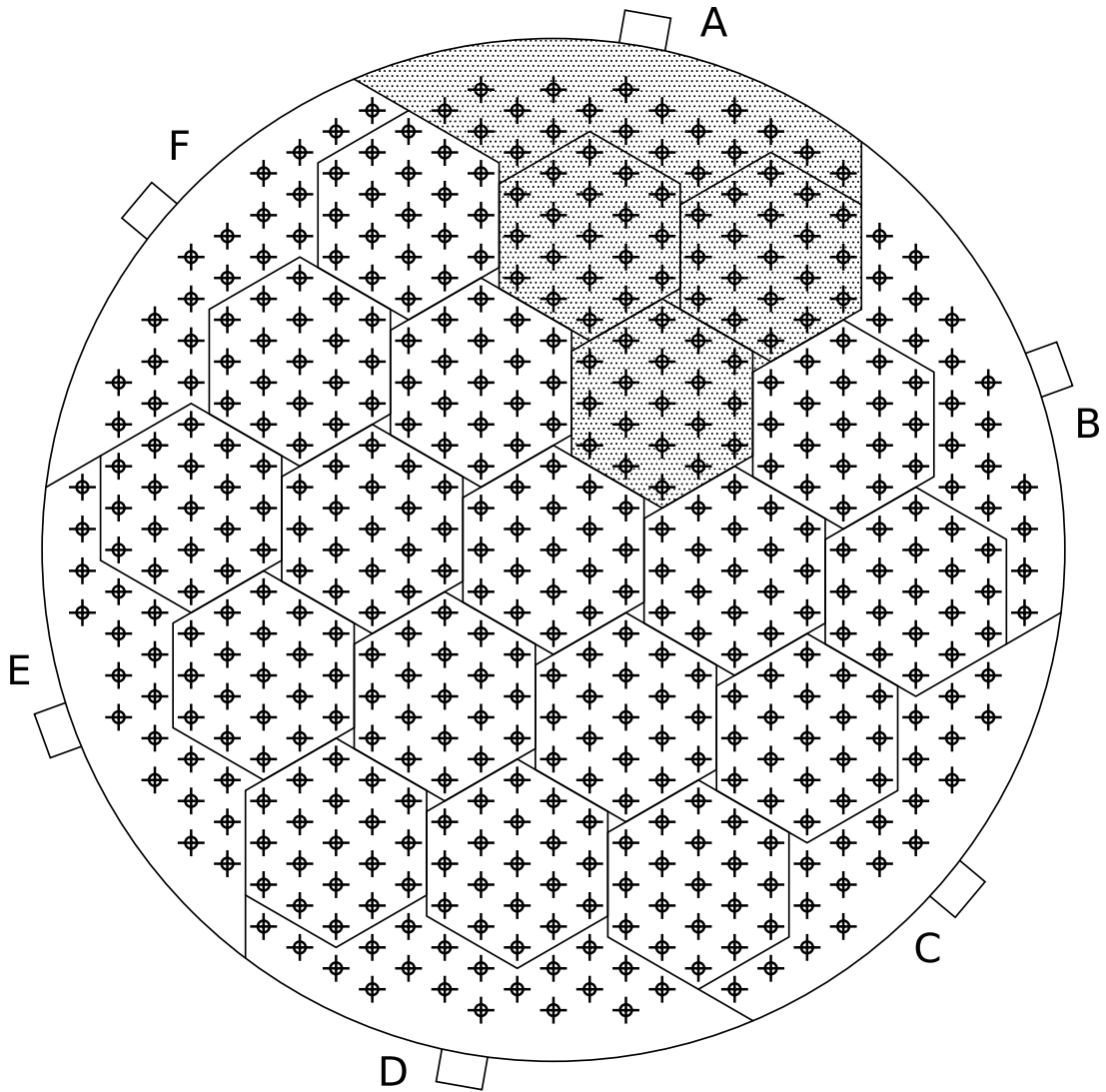


Figure 2.1: The antenna position and channel assignment of the MU radar. Modified after Fukao et al. (1985a).

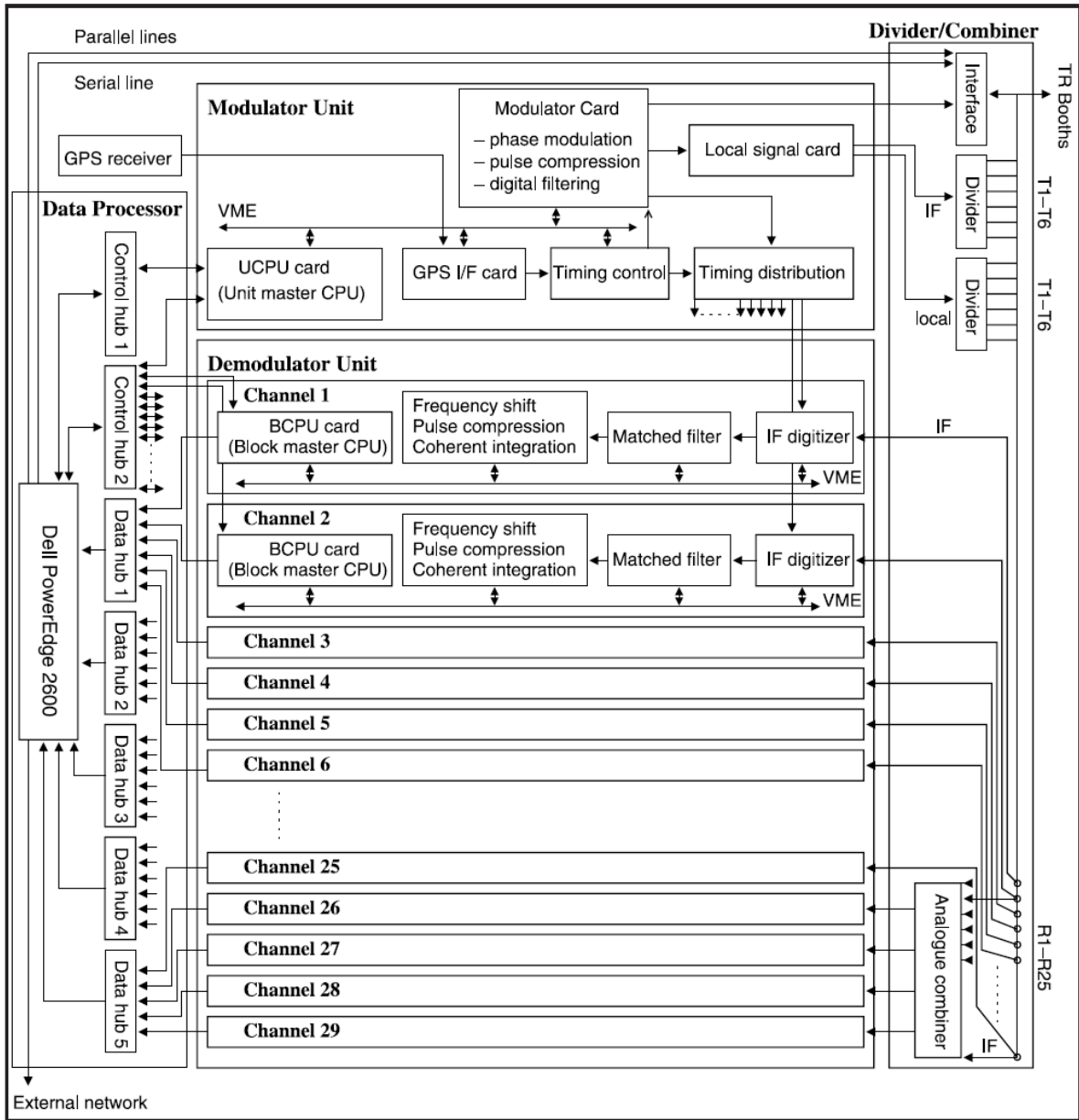


Figure 2.2: The block diagram of of the MU radar (Hassenpflug et al., 2008).

## 2.2 System model

In this chapter, the target radar system is the middle-and-upper atmosphere (MU) radar (Fukao et al., 1985a,b), which is a large MST radar at Shigaraki, Japan (34.85°N, 136.10°E). The center frequency of the MU radar is 46.5 MHz in the VHF band. This radar consists of a phased antenna array of 475 three-element crossed-Yagi antennas arranged in a circle with its diameter of 103 m. Figure 2.1 is the antenna position and channel assignment of the MU radar. Each 19 antennas indicated by polygonal frames in Fig. 2.1 is a subarray channel. This radar first started its operation in 1984 with the capability of dividing the entire array into 4 individual channels (Fukao et al., 1985a,b). Later, in 2004, the MU radar was upgraded with the digital multichannel receiver system that enables maximum of 25 channel adaptive array signal processing (Hassenpflug et al., 2008). In the upgraded system, the signals received from each of the 19 antennas are handled by an individual demodulator, as shown in Fig. 2.2.

## 2.3 Methods for generating simulated signals of atmospheric radar observation

Throughout this thesis, numerical simulations of atmospheric radar observations are used for the quantitative comparison of signal processing algorithms. For this purpose, the complex time series at each receiver channel is needed for the atmospheric echoes, clutter signal, and noise. Here, the methods for generating these simulated signals are explained.

### 2.3.1 Some representative quantities in a Doppler spectrum

In simulations and observations, the clutter suppression capability of an arbitrary algorithm should be numerically evaluated for the quantitative comparison. For this purpose, some quantities in a spectrum are defined as in Fig. 2.3. These values are also used to generate simulated signals. Here, the spectrum after sufficient number of incoherent integration is written as  $\bar{S}(v)$ , the atmospheric peak power  $P_S$ , clutter peak power  $P_I$ , and the noise floor level  $P_N$ .

**SNDR** The signal-to-noise density ratio, i.e., the peak height of the atmospheric spectrum above the noise floor level:

$$\text{SNDR} = P_S/P_N = \bar{S}(v_d)/P_N. \quad (2.1)$$

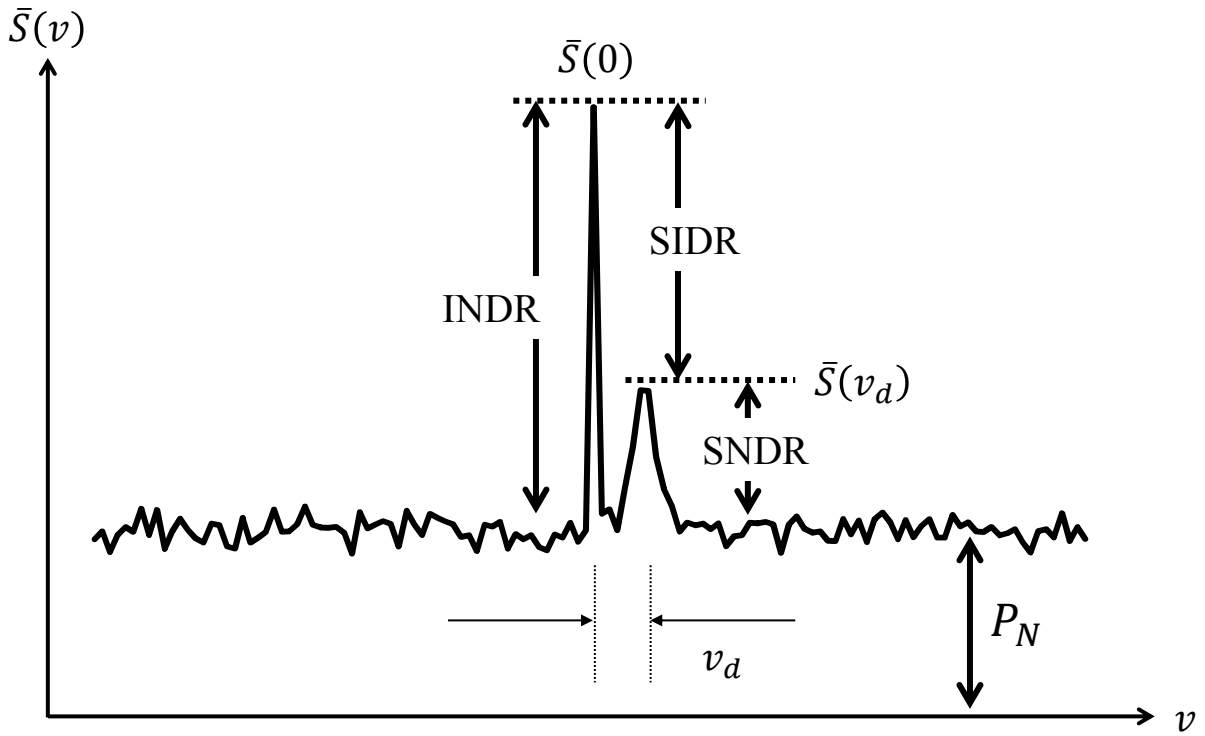


Figure 2.3: Representative quantities in a Doppler spectrum.

**INDR** The interference-to-noise density ratio, i.e., the peak height of the clutter spectrum above the noise floor level. This is mainly used to specify the clutter power. For the ground clutter, it is defined as:

$$\text{INDR} = P_I/P_N = \bar{S}(0)/P_N. \quad (2.2)$$

**SIDR** The signal-to-interference density ratio, i.e., the peak height difference between the atmospheric and clutter spectrum. For the ground clutter, it is defined as:

$$\text{SIDR} = P_S/P_I = \bar{S}(v_d)/\bar{S}(0). \quad (2.3)$$

**SINDR** The signal-to-interference-plus-noise density ratio. This is defined in the same manner with the signal-to-interference-plus-noise ratio (SINR) (e.g., Takao and Kikuma, 1986). For example, the SINDR related to the ground clutter is:

$$\text{SINDR} = \frac{P_S}{P_I + P_N} = \frac{\bar{S}(v_d)}{\bar{S}(0) + P_N}. \quad (2.4)$$

## 2.3.2 Atmospheric signal generation

There are two major methods for simulating the time series of atmospheric signal. The first one uses the inverse Fourier transform on the desired spectrum to obtain the complex time series. The received signal at each receiver channel is then generated using the array manifold vector. The second one is the more realistic simulation that sums up all the backscattered signals from a large number of distributed scatterers in the target radar volume. The turbulent motions of scatterers are also simulated in this model. Detailed procedures of these methods are explained below.

### Use of the inverse Fourier transform on the desired spectrum

This method was first introduced by Zrnic (1975) to generate the Doppler spectrum in weather radars. As mentioned in section 1.5.5, the shape of atmospheric spectrum can be approximated by a Gaussian function. Thus, the desired spectral shape  $S(\omega; P_s, v_d, \sigma_d)$  is first designed using Eq. (1.49). Additionally, the time series of complex outputs at each receiver has random fluctuations following a Gaussian distribution for both real and imaginary components. This results in the model spectrum having the statistical fluctuation following the  $\chi^2$  distribution with two degrees of freedom, because the power spectra are the squared sum of complex received signals. The spectrum with this fluctuation,  $\hat{S}(\omega)$ , can be simulated using the random numbers  $X_r(\omega)$  that follows  $\chi_2^2$ :

$$\hat{S}(\omega) = S(\omega; P_s, v_d, \sigma_d) X_r(\omega). \quad (2.5)$$

To generate complex time series at the phase origin,  $s_o(t)$ , the inverse Fourier transform  $\mathcal{F}^{-1}[(\cdot)]$  is used on Eq. (2.5):

$$s_o(t) = \mathcal{F}^{-1} \left[ \sqrt{\hat{S}(\omega)} \angle U_r(\omega) \right], \quad (2.6)$$

where  $U_r(\omega)$  represents the random numbers following the uniform distribution in  $[0, 2\pi)$ , and notation  $A \angle B$  means a complex number with amplitude  $A$  and argument  $B$ .

The time series at each receiver  $s_i(t)$  can then be calculated from  $s_o(t)$ , using the gain of each receiver  $g_i(\theta_o, \phi_o)$  and the array manifold vector  $\mathbf{A}(\theta_o, \phi_o)$ :

$$s_i(t) = A_i(\theta_o, \phi_o) g_i(\theta_o, \phi_o) s_o(t), \quad (2.7)$$

where  $(\theta_o, \phi_o)$  is the main beam direction.

The advantage of this method is its simplicity. The desired spectral shape can easily be designed by this method, and the resultant spectrum well simulates the nature

of atmospheric spectrum. Hence, this technique is used in various applications (e.g., Nishimura et al., 2012; Yamamoto et al., 1988). In Chapters 2 and 3, this is the method for generating atmospheric echoes.

One of the problems of this method is the lack of continuity between successive spectra. Difficulties in describing the nature of distributed targets also arises, although this can be overcome by the model introduced by Valaee et al. (1995), that uses the generalized array manifold vector  $\bar{\mathbf{A}}(\theta, \phi)$  instead of  $\mathbf{A}(\theta, \phi)$  in Eq. (2.7):

$$\bar{\mathbf{A}}(\theta, \phi) = \iint \mathbf{A}(\theta, \phi) \delta(\theta, \phi) d\theta d\phi, \quad (2.8)$$

where  $\delta(\theta, \phi)$  is the angular distribution of the scatterer. In this case, this is determined by the power directional pattern of the main beam.

### Distributed scatterer model

This method is proposed by Holdsworth and Reid (1995). At the beginning of a simulation, point scatterers are randomly placed in the enclosing volume, which is defined by a cylindrical volume enclosing the effective beam width and the target range gate. This must be sufficiently larger than the actual radar volume shown in Fig. 1.3.

The amplitude of the signal from each scatterer is determined from the random reflectivity ratio assigned to each scatterer as well as the weighting function for the position of the scatterer, defined by the effective beam width and the range weighting function. The phase is determined by the distance between each receiver and each scatterer. Each scatterer is characterized by its reflectivity ratio  $0.5 \leq p_k \leq 1$ , and three-dimensional location  $\mathbf{l}_k(t)$ . Let the location of  $i$ -th receiver be  $\mathbf{L}_i$ , and the phase center be  $\mathbf{L}_o$ . The two-way distance  $d_{ik}(t)$  and the direction  $(\theta_{ik}(t), \phi_{ik}(t))$  from  $i$ -th receiver to  $k$ -th scatterer are computed as:

$$\mathbf{V}_{ik}(t) = \mathbf{l}_k(t) - \mathbf{L}_i = [x_{ik}(t), y_{ik}(t), z_{ik}(t)], \quad (2.9)$$

$$d_{ik}(t) = \|\mathbf{V}_{ik}(t)\| + \|\mathbf{l}_k(t) - \mathbf{L}_o\|, \quad (2.10)$$

$$\theta_{ik}(t) = \arccos \frac{z_{ik}(t)}{\|\mathbf{V}_{ik}(t)\|}, \quad (2.11)$$

$$\phi_{ik}(t) = \arctan \frac{x_{ik}(t)}{y_{ik}(t)}, \quad (2.12)$$

where  $\mathbf{V}_{ik}(t)$  is the radial vector from  $i$ -th receiver to  $k$ -th scatterer. The range weighting function  $\mathcal{R}_k(t)$  is defined as a Gaussian function (Cheong et al., 2004):

$$\mathcal{R}_k(t) = \exp \left[ -\frac{(d_{ik}(t) - r_o)^2}{4\sigma_r^2} \right], \quad (2.13)$$

where  $\sigma_r = 0.34c\Delta T/2$  is a typical selection for the rectangular Tx pulse (Doviak et al., 1979). The power weighting function  $\mathcal{P}_k(t)$  is defined as follows:

$$\mathcal{P}_k(t) = \exp \left[ -\frac{\sin^2(\theta_{ik}(t) - \theta_o)}{\sin^2 \theta_b} \right], \quad (2.14)$$

where  $\theta_o$  is the zenith angle of the beam direction, and  $\theta_b$  is the half power half width of the radar beam; see Fig. 1.3. The time series from  $k$ -th scatterer measured at  $i$ -th receiver channel then becomes:

$$s_i(t) = g_i(\theta_{ik}(t), \phi_{ik}(t)) p_k \mathcal{R}_k(t) \mathcal{P}_k(t) \exp \left[ j2\pi \frac{d_{ik}(t)}{\lambda} \right], \quad (2.15)$$

where  $g_i(\theta, \phi)$  is the gain of  $i$ -th receiver.

For every sample time, the position of each scatterer is updated along with the background wind, and the turbulent motion generated by mutual interaction among scatterers:

$$\mathbf{l}_k(t + \Delta t) = \mathbf{l}_k(t) + [\mathbf{v}_{bk} + \mathbf{v}_{tb,k}(t)] \Delta t, \quad (2.16)$$

where  $\mathbf{v}_{bk}$  is the background-wind velocity vector, and  $\mathbf{v}_{tb,k}(t)$  is the turbulent velocity vector.  $\mathbf{v}_{tb}(t)$  is calculated using the random turbulent motion vector  $\mathbf{v}_j$  assigned to  $j$ -th scatterer:

$$\mathbf{v}_{tb,k}(t) = \sum_{j=1}^{N_p} \mathbf{v}_j \exp \left[ -\frac{\|\mathbf{l}_k - \mathbf{l}_j\|^2}{C_{tb}} \right], \quad (2.17)$$

where  $N_p$  is the number of scatterers,  $C_{tb}$  is the turbulent scale factor.  $C_{tb} = 1$  is used in this thesis. After each update, scatterers that have moved outside of the enclosing volume are reentered from the opposite side, with new values for random reflectivity  $p_k$  and their turbulent motion vector  $\mathbf{v}_k$ . Each component of  $\mathbf{v}_k$  is given by random numbers following the Gaussian distribution with its standard deviation determined by the required spectral width of the atmospheric spectrum.

The advantage of this model is the realistic characteristics of generated signals compared with the inverse Fourier transform method, including the continuity of time series between each periodogram and physical parameters of the radar system. This technique was originally developed for spaced antenna method (Holdsworth and Reid, 1995), and also used in the simulation of adaptive clutter suppression and range imaging (Yu et al., 2010). In Chapter 4, this is used to generate atmospheric signals instead of the method using the inverse Fourier transform, because the signal loss must be strictly handled in the proposed algorithm. As mentioned above, the use of the inverse Fourier transform

and array manifold vector results in the backscattered echo from point-like target instead of the distributed sources. As mentioned in section 1.7.1, the beam directional error can be larger than actual in these cases. Therefore, the discussion in Chapter 4 needs the realistic model introduced herein, especially in evaluating the beam directional error in section 4.4.4.

The major drawback of this method is its large calculation cost in updating the positions of scatterers, especially in high frequencies, because the more scatterer density is needed to accurately represent the distributed scatterer volume with the shorter wavelengths. Cheong et al. (2008, 2004) address this problem by using the precalculated random turbulent motion grids and interpolation technique. However, in VHF band, not so many scatterers are needed because of its relatively long wavelength. Hence, the interpolation technique is not used in this thesis.

### 2.3.3 Clutter signal generation

The clutter sources can be assumed as point targets. Suppose a point scatterer exists at the 3-D location  $\mathbf{l}(t) = [x_u(t), y_u(t), z_u(t)]$ . Note that for the stationary clutter,  $\mathbf{l}(t) = \mathbf{l}(0)$ . The two-way distance  $d_i(t)$  and direction  $(\theta_u(t), \phi_u(t))$  to the target from the  $i$ -th receiver position  $\mathbf{L}_i$  are calculated as the same manner in Eqs. (2.9) to (2.12). Let  $P_u$  be the power of the clutter signal. The time series  $u_i(t)$  for this receiver channel is then written as:

$$u_i(t) = \sqrt{P_u} g_i(\theta_u(t), \phi_u(t)) \exp \left[ j2\pi \frac{d_i(t)}{\lambda} \right]. \quad (2.18)$$

In actual, the clutter power  $P_u$  is selected such that the SIDR or INDR becomes the required value.

### 2.3.4 Noise generation

Noise is modeled as a complex random number, having real and imaginary parts following a normal distribution. For the  $i$ -th receiver channel, the noise  $n_i(t)$  is defined as:

$$n_i(t) = \frac{1}{\sqrt{2}} [\mathcal{N}(0, 1) + j\mathcal{N}(0, 1)], \quad (i = 1, \dots, M) \quad (2.19)$$

where  $\mathcal{N}(0, 1)$  denotes a random number generator that obeys the normal distribution with a mean of 0 and standard deviation of 1. Note that the average noise power spectral density generated by Eq. (2.19),  $P_N$ , becomes 1, owing to scaling by  $1/\sqrt{2}$ .

## 2.4 Simulation of adaptive meteor clutter rejection

In this section, the result of numerical simulations of the adaptive meteor clutter rejection technique for mesospheric radar observations are presented.

### 2.4.1 Signal generation

In this simulation, each spectrum contains two kinds of echoes, atmospheric and meteor echoes, as well as the galactic noise. Signal generation procedure for atmospheric echoes are already mentioned in section 2.3.2. In this simulation, the method based on the inverse Fourier transform is used. The noise is also generated using Eq. (2.19). Here, the detail of the generation of meteor trail echoes is presented.

In this simulation, a meteor trail echo is modeled as a backscattering from a linearly shaped hard target with exponentially decreasing echo power that is moved by the background wind; i.e. underdense meteor trail. Phases of meteor echoes at  $i$ -th receiver,  $\omega_{M,i}(t)$ , are calculated through the procedure in section 2.3.3. Amplitudes are the square root of the meteor echo power  $P_M(t)$ , which is known to decay exponentially as (Cep-lecha et al., 1998):

$$P_M(t) = P_M(0) \exp \left[ -\frac{32\pi^2 D_a t}{\lambda^2} \right], \quad (2.20)$$

where  $D_a$  is the ambipolar diffusion coefficient.  $D_a$  varies with seasons, latitude, and ranges. Here,  $D_a \sim 1 \text{ m}^2 \text{ s}^{-1}$  at 80 km is used in this simulation. Consequently the time series of meteor trail echoes  $s_i(t)$  can be obtained as:

$$s_i(t) = \sqrt{P_M(t)} \exp j\omega_{M,i}(t). \quad (2.21)$$

### 2.4.2 Adaptive signal processing

After generating received signals for both atmospheric and meteor echoes, the complex time series  $\mathbf{X}(t) = [X_1(t), X_2(t), \dots, X_M(t)]^T$  is constructed with the sum of them for each receivers. The covariance matrix  $\mathbf{R}$  for sample number  $k_t$  is generated and updated using the following set of expressions:

$$\mathbf{R}(0) = \mathbf{X}(0)\mathbf{X}^H(0), \quad (2.22)$$

$$\mathbf{R}(k_t) = \gamma\mathbf{R}(k_t - 1) + (1 - \gamma)\mathbf{X}(k_t)\mathbf{X}^H(k_t), \quad (2.23)$$

where  $k_t = 1, 2, \dots$  and  $0 \leq \gamma < 1$  is the forgetting factor. In this simulation,  $\gamma = 0.995$  is used, which is the equivalent of accumulating received signals of about 1500 samples

to obtain one covariance matrix. The time series of received signals  $\mathbf{X}(t)$  is synthesized employing two methods to make a comparison, the NC-DCMP algorithm (NC) and nonadaptive beamforming. For each renewal of the covariance matrix, an optimal weight vector  $\mathbf{W}(t)$  is calculated using Eq. (1.54). The permissive SNR loss  $L_{\text{SNR}}$  is set as an increasing sequence of five equal intervals in the range from 0.5 to 3 dB. For the nonadaptive beamforming,  $\mathbf{W}(t) = \mathbf{A}(\theta_o, \phi_o)$  using an array manifold, where the desired direction  $(\theta_o, \phi_o)$  is set to  $(0^\circ, 0^\circ)$ . The beam synthesis of the received signals using the weight vector  $\mathbf{W}$  is performed through Eq. (1.21).

### 2.4.3 Incoherent integration and meteor trail echo rejection

After the beam synthesis of the received signals and calculation of spectra, the incoherent integration is performed by accumulating  $N_i$  successive spectra. As mentioned in section 1.5.2, fluctuation of amplitudes is expected to be reduced to  $1/\sqrt{N_i}$  in this manner. In practice, spectra with strong meteor clutters should be removed from the integration. A threshold  $B_t$  is thus set to 3.5 dB over the peak power of atmospheric echo  $P_S$  for deciding which spectrum contains a clutter and should be discarded. In this simulation, the peak power of an atmospheric echo is known; e.g., +10 dB over the noise level. The probability of random fluctuations being at least +3.5 dB over the actual peak power, e.g. +13.5 dB over the noise level in this case, is less than 5% in the  $\chi^2$  distribution with two degrees of freedom. Any peak over  $B_t$  is thus assumed to be a clutter.

### 2.4.4 Detailed simulation settings

#### Radar system

The target radar system is based on the MU radar at Shigaraki MU Observatory, Japan. Detailed specifications of the MU radar is mentioned in section 2.2. In this simulation, all 25 receiver channels in Fig. 2.1 are separately used, forming an adaptive array with 25 degrees of freedom. Observational parameters are listed in Table 2.1. Note that using  $N_i = 38$  successive spectra for incoherent integration is equivalent to averaging over about 1 minute.

#### Experimental parameters

Two types of simulations were conducted. First, assuming an arbitrary range with both atmospheric and meteor echoes observed, the SNDR were varied and the RMS error of

Table 2.1: Radar settings used in the simulation of meteor clutter rejection.

IPP	3120 $\mu$ s
Time resolution	3.12 ms
Range resolution	900 m
Ranges	75 – 127 km
No. of frequency samples $N_f$	128
No. of range samples $N_h$	59
No. of incoherent integration $N_i$	38

the wind velocity estimation were calculated at each SNDR. This is referred to as “simulation 1”. In this simulation, the meteor clutter was designed to have a echo intensity of 15 dB over the noise level, and a radial velocity of  $5 \text{ ms}^{-1}$ . Appearance rate of meteor echoes was 100 %, i.e. each spectrum contains a meteor echo. Note this is not a realistic setting about the number of meteor trails, but this simulation is intended to test the maximum capability of the method and the more realistic situation is given to simulation 2. The SNDR of the atmospheric echo was changed from 0 to 30 dB over the noise level, in steps of 5 dB. The SIDR was then moved from  $-15 \text{ dB}$  to  $15 \text{ dB}$ . Above procedures were repeated 100 times to obtain the averaged RMS error of the wind velocity estimations. The thresholding of the contaminated spectra stated in section 2.4.3 is not used in simulation 1.

Second, the same procedure were applied to multiple ranges and records assuming actual mesosphere observations. This is referred to as “simulation 2”. Again, 100 successive records of simulation data are generated, and results are averaged. The thresholding of the spectra explained in section 2.4.3 is introduced in this simulation to conform to the actual observations. Several additional variabilities are also considered. Appearance rate of meteor echoes is set to 33 % in this case, i.e., one-third of all spectra contain a meteor echo. The height distribution of meteor echoes is known to have a Gaussian form, and has a maximum range at about 90 km (e.g., Nakamura et al., 1991). Hence, the range distribution of each meteor is simulated as a random variable that follows a Gaussian distribution with mean of 90 km and standard deviation of 6.7 km. The power distribution is also introduced as the same manner. For the atmospheric echoes, decays of the echo power  $P_S$  with range from the radar and the cyclic variations of the mean

wind velocity  $v_d$  assuming a gravity wave are introduced:

$$P_S(r) = P_S(r_m)D_S^{|r-r_m|}, \quad (2.24)$$

$$v_d(t) = v_d(0) + v_g \sin\left(\frac{2\pi}{T_g}t\right), \quad (2.25)$$

where  $r_m$  is the range having maximum echo power,  $D_S$  is the decay factor for echo power and  $v_g$  and  $T_g$  are the amplitude and wave period of the gravity wave, respectively. Tables 2.2 and 2.3 give the detailed parameters for generating atmospheric and meteor echoes in simulation 2. Note that decibel values are against the noise level.

Table 2.2: Parameters for generating atmospheric echoes in simulation 2.

Decay factor for ranges $D_S$	$-3 \text{ dB km}^{-1} \sim 0.5$
Range at the maximum power $r_m$	78 km
Maximum echo power $P_S(r_m)$	15 dB
Spectral width $\sigma_d$	$1 \text{ m s}^{-1}$
Amplitude of the gravity wave $v_g$	$5 \text{ m s}^{-1}$
Wave period of the gravity wave $T_g$	33 min

Table 2.3: Parameters for generating meteor echoes in simulation 2.

Center of initial power distribution $P_M(0)$	20 dB
Standard deviation of power distribution	2.5 dB
Center of range distribution	90 km
Standard deviation of range distribution	6.7 km
Appearance rate	33 %
Radial velocity	$0 - 25 \text{ m s}^{-1}$
Diffusion coefficient $D_a$	$1.0 \text{ m}^2 \text{ s}^{-1}$
Orientation	Uniformly random

## 2.4.5 Results and discussion

Figure 2.4 is an example of the spectra generated in simulation 1. The horizontal axis is the Doppler velocity and the vertical axis is the echo intensity. In this case, the SNDR of the atmospheric echo is set to 10 dB. Lines are the spectra of the atmosphere only, meteor only, and the synthesized spectra of the nonadaptive beamforming and the NC-DCMP algorithm. Marks show the peak powers and Doppler velocities of the Truth and those obtained by the nonadaptive beamforming and NC-DCMP algorithm. Figure 2.5 is the RMS error in the Doppler velocity estimations for each SIDR averaged 100 times, obtained employing the nonadaptive beamforming and the NC-DCMP algorithm. The horizontal axis is the SIDR from  $-15$  to  $15$  dB, and the vertical axis is the RMS error at each SIDR.

Next, Fig. 2.6 shows the relationship between the accuracy of wind velocity estimations and the echo intensities of the desired or undesired signals for each beam synthesis method. The left panel of Fig. 2.6 shows the averaged RMS error of the estimated wind velocity in simulation 2. The horizontal axis is the RMS error of the estimated Doppler velocity. The solid line is for the case of no meteor clutter, the dashed line is for the nonadaptive beamforming, and the dotted line is for the NC-DCMP algorithm. The right panel shows the maximum echo intensity of the atmospheric and meteor echoes averaged in simulation 2. The solid line is for the atmospheric echoes and the dotted line is for the meteor echoes. Here, the atmospheric echo has peak power around 78 km, while the intensity of meteor echoes increases with range. The vertical axes of these two panels have units of kilometers.

In simulation 1, all spectra are used without thresholding. In such a case, the adaptive meteor clutter rejection technique is found to improve the accuracy of the wind velocity estimations especially when the interference is stronger than or almost equal to the atmospheric echoes. As seen in Fig. 2.4, the meteor clutter is suppressed well by the NC-DCMP algorithm. Thus, wind velocities are estimated near the true peak by the NC-DCMP algorithm, while the nonadaptive beamforming gives wrong values contaminated by meteor clutters. Consequently, Fig. 2.5 shows that with SIDRs under 0 dB, as in Fig. 2.4, the echo intensity of meteor clutters is stronger than that of atmospheric echoes and the nonadaptive beamforming gives incorrect estimations of wind velocity because of the interference. As a result, the observable echo intensity improves by about 15 dB when employing the NC-DCMP algorithm. In addition, it should be noted that meteor trail echoes can be extracted employing the same method if needed, by simply subtracting the obtained meteor-suppressed signals from the original received ones.

In simulation 2, strong interference is suppressed by spectral thresholding. Employing this procedure, the initial guess of the peak search is made accurate to some extent by

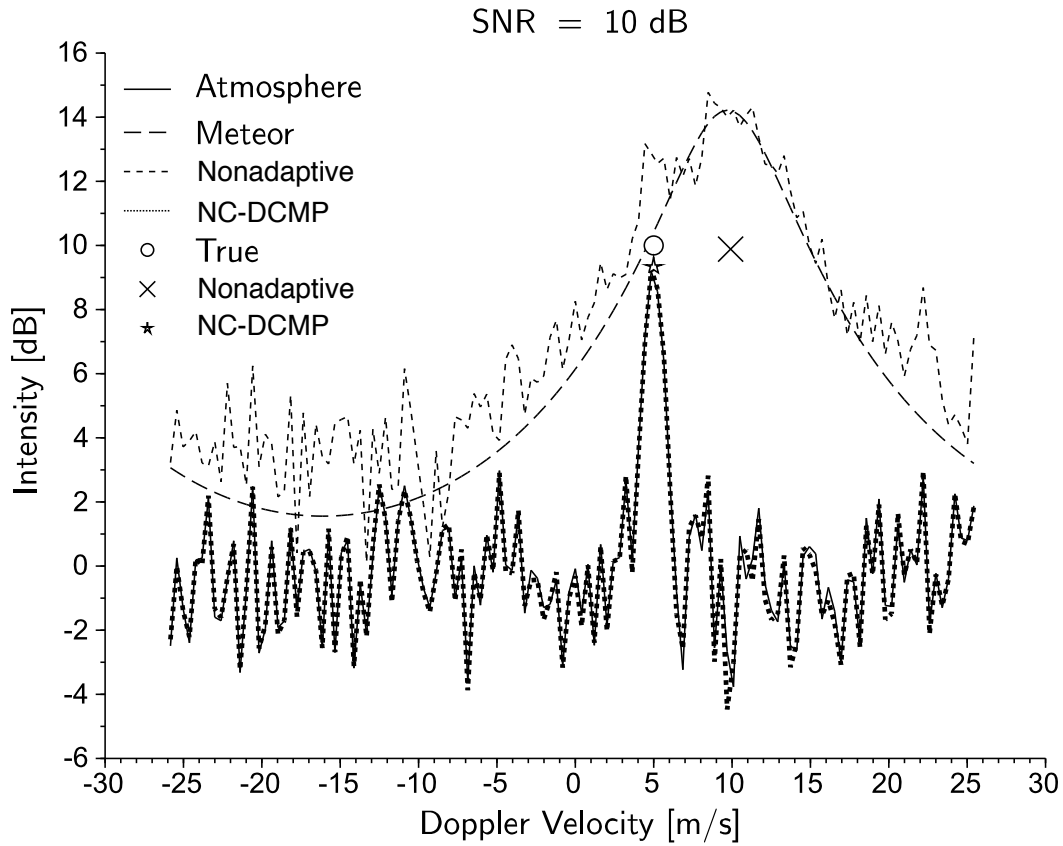


Figure 2.4: Example of the spectra generated in simulation 1. SIDR is  $-5$  dB.

discarding contaminated spectra in incoherent integration, while fewer spectra result in more fluctuation in the integrated spectra, which can bring low accuracy. Additionally, interferences below the threshold remain with no change with the nonadaptive beamforming, and this leads to an increase in the RMS error in the spectral fitting for the nonadaptive beamforming. On the contrary, the NC-DCMP algorithm suppresses interferences automatically in advance, and improves both the number of spectra discarded in incoherent integration and the RMS error in the spectral fitting. These trends are clearly shown in Fig. 2.6. Here, the NC-DCMP algorithm discards only 1.3% of spectra, while 10.9% with the nonadaptive beamforming. The average RMS errors at 78 km are  $1.5 \text{ ms}^{-1}$  for the NC-DCMP algorithm and  $10.1 \text{ ms}^{-1}$  for the nonadaptive beamforming. As seen in Fig. 2.6 (b), the average SIDR of simulation 2 is at most  $-10$  dB at 78 km. Figure 2.5 shows that even the NC-DCMP algorithm give low accuracy with

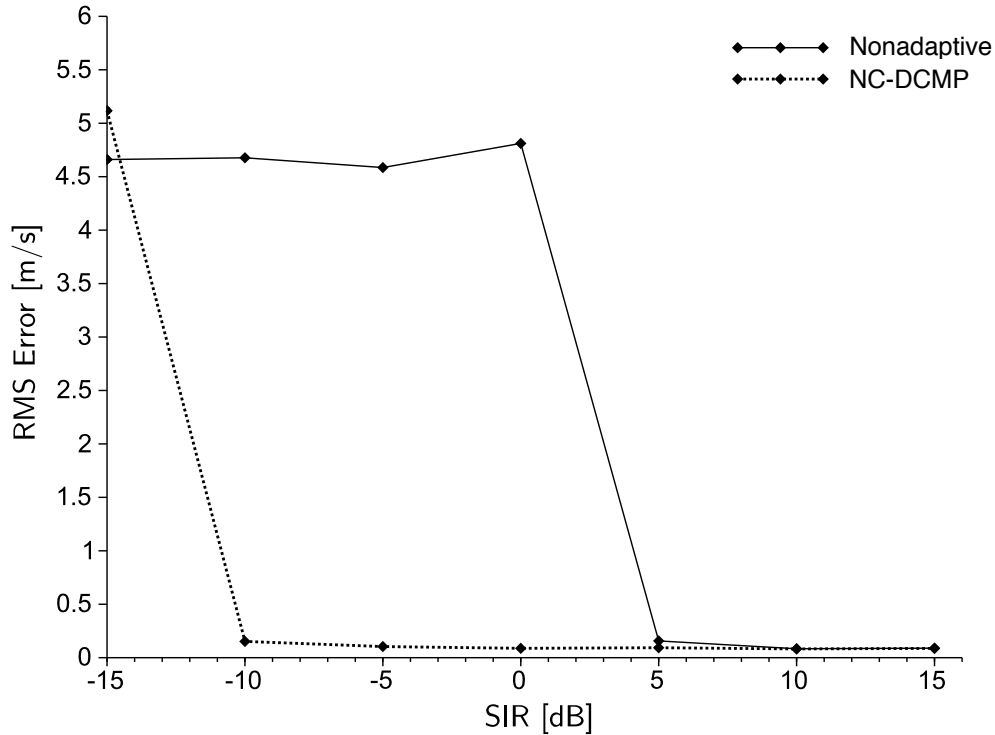


Figure 2.5: RMS errors of wind velocity estimated with the nonadaptive beamforming and NC-DCMP algorithm.

the SIDR under  $-10$  dB and thus the result is consistent with simulation 1. At higher ranges, where there are more meteor echoes, the accuracy of the estimated wind velocity is low for both methods, but the error is about  $8 \text{ m s}^{-1}$  less for the NC-DCMP algorithm. Additionally, the RMS error has a flat floor from 76 to 78 km with the NC-DCMP algorithm, which is about four times as wide as that with the nonadaptive beamforming. This is the benefit of the adaptive clutter rejection technique and implies the effectiveness of the technique in mesosphere observations.

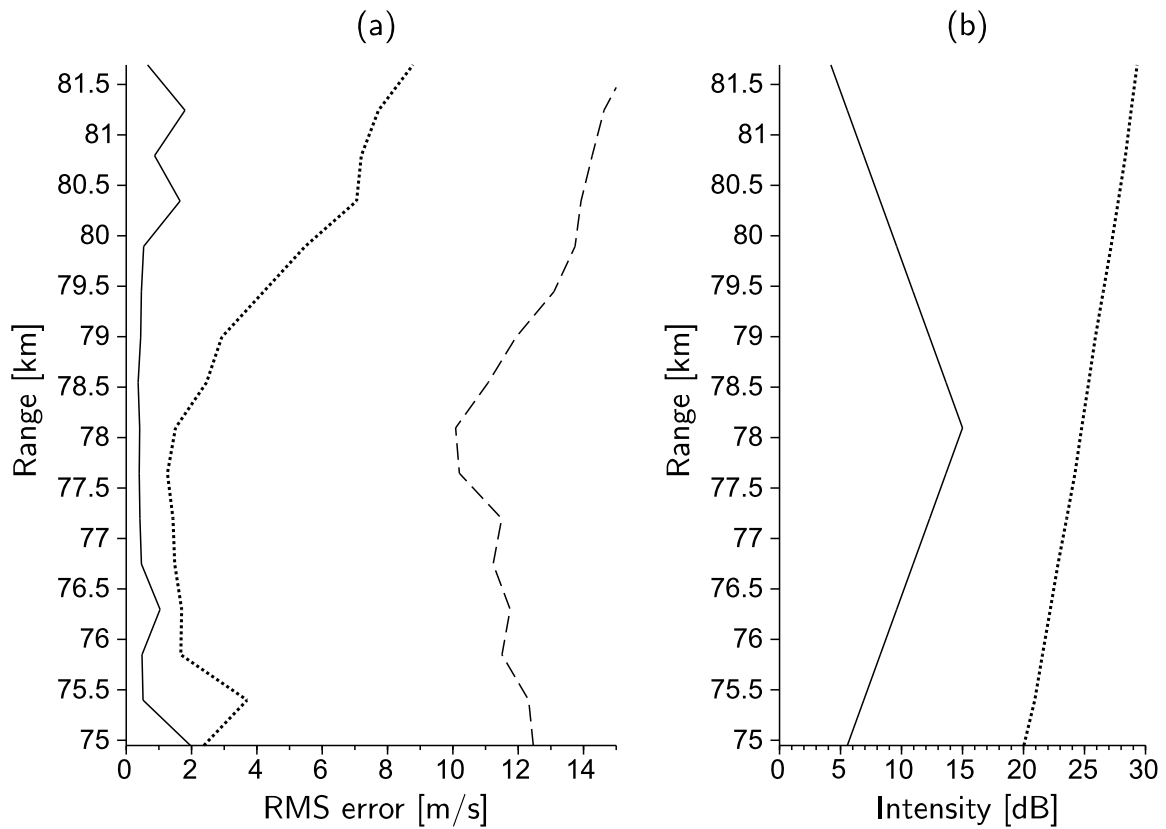


Figure 2.6: (a) RMS errors of the wind velocity estimations of the nonadaptive beamforming and NC-DCMP algorithm. (b) Intensities of the atmospheric and meteor echoes for each range.

## 2.5 Applying the adaptive meteor clutter rejection technique to an actual observation

In the previous section, the effectiveness of the NC-DCMP algorithm has been shown in numerical simulations. This section presents the results of applying the adaptive meteor clutter rejection technique to actual mesospheric observations.

### 2.5.1 Observational settings of the radar system

A series of mesosphere observations was made on October 8, 2011 at Shigaraki MU Observatory, Japan.  $N_R = 100$  successive records taken from 14:05 to 15:46. The ob-

servational parameters are listed in Table 2.4. Figure 2.7 shows the whole observed data taken by the MU radar. As done in simulation 2 of section 2.4, the time resolution of the adaptive beam synthesis is 3.12 ms. After the clutter cancellation,  $N_i = 38$  successive spectra are used for incoherent integration to obtain each record, which is equivalent to averaging over about 1 minute.

Table 2.4: Radar system settings for the observation made by the MU radar on 14:05 to 15:46 (UTC), October 8, 2011.

IPP	3120 $\mu$ s
Time resolution	3.12 ms
Range resolution	900 m
Valid ranges	75 – 127 km
No. of time samples $N_f$	512
No. of range samples $N_h$	59
No. of incoherent integration $N_i$	38

## 2.5.2 Signal processing

The nonadaptive beamforming and the NC-DCMP algorithm were applied to the same observed data sequence to compare the ability of the two methods to suppress clutter. Procedures of the signal processing are exactly the same as those described in section 2.4. Additionally, thresholding and accumulation of spectra were performed as in the previous section. However, the threshold  $B_t$  for removing contaminated spectra is not known for the actual observation, thus determined as follows. First, adaptive beam synthesis were performed on all received signals employing the nonadaptive beamforming and the NC-DCMP algorithm. Afterwards, the Fourier transform was applied to obtain synthesized spectra  $S(k_i, k_h, k_f)$ , where  $k_i = 1, \dots, N_i N_R$  is the spectral index,  $k_h$  is the range index, and  $k_f$  is the frequency index. The frequency-wise sum of  $S(k_i, k_h, k_f)$  is taken by:

$$\hat{S}(k_i, k_h) = \sum_{k_f=1}^{N_f} S(k_i, k_h, k_f). \quad (2.26)$$

Finally, the threshold  $B_t$  is selected such that satisfies the following relationship:

$$p[\hat{S}(k_i, k_h) > B_t] \leq 5\%. \quad (2.27)$$

14:05.11 - 16:02.32 10/08/2011

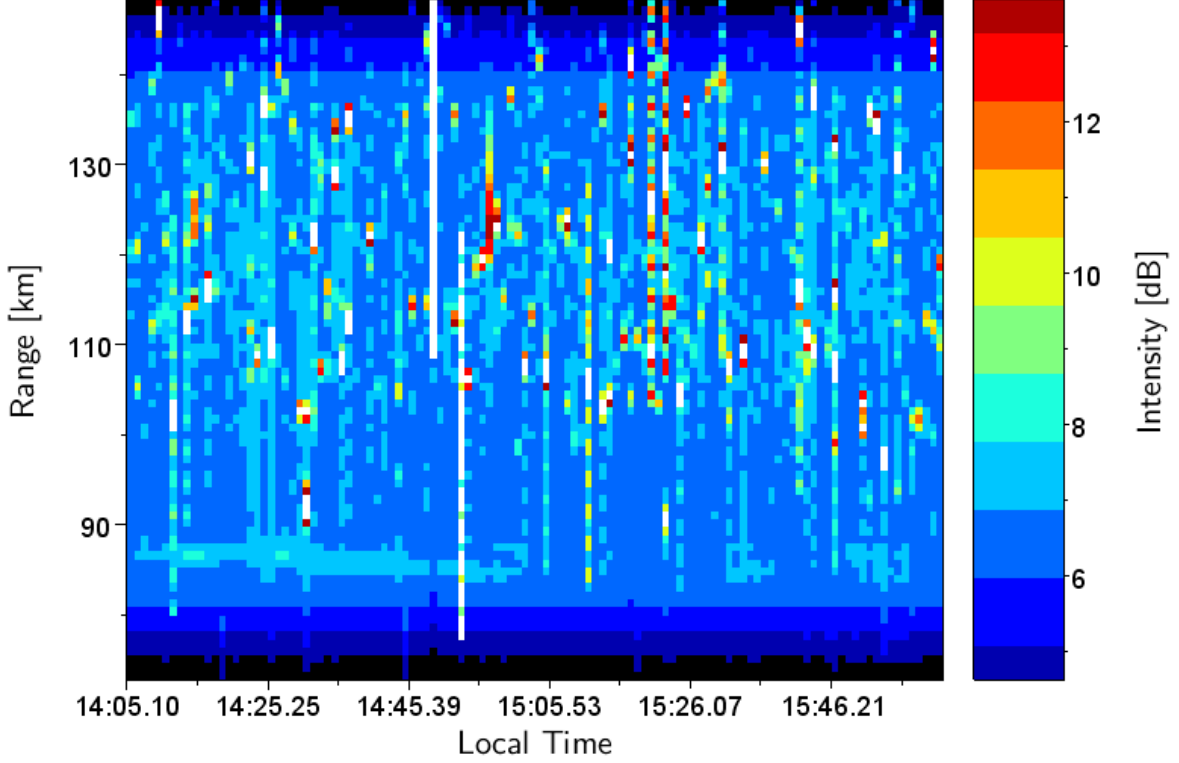


Figure 2.7: The range-time-intensity plot for the whole observed data.

for all  $k_h$  that correspond to 74 – 80 km. Here,  $p[\hat{S}(k_i, k_h) > B_t]$  denotes the probability of peaks in  $\hat{S}(k_i, k_h)$  being larger than the current threshold  $B_t$ . The purpose of Eq. (2.27) is to make the number of discarded spectra the same as the number in the simulation of the previous section. To compute  $B_t$ , its value is iteratively enlarged to find the minimum value that satisfies Eq. (2.27). The overlaid spectral peaks are shown in Figs. 2.8 and 2.9 for the nonadaptive beamforming and the NC-DCMP algorithm, respectively. The horizontal axis is the peak power for each range and the vertical axis is the range. Dashed lines are the threshold  $B_t$  for the spectra of processed employing the two methods.

### 2.5.3 Results and discussion

Table 2.5 shows the threshold  $B_t$ , the deflection ratio  $R_d$ , and the equivalent number of incoherent integration  $\hat{N}_i$  after discarding contaminated spectra. Figure 2.10 shows

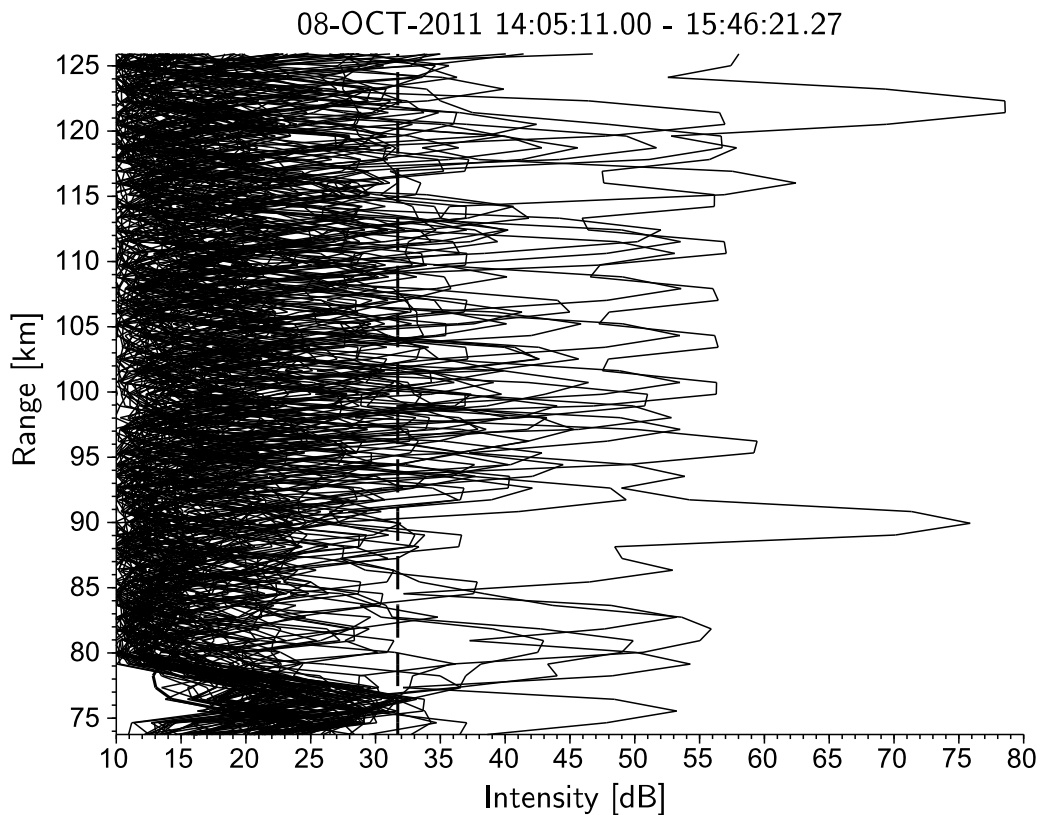


Figure 2.8: Overlaid spectral peaks processed by the nonadaptive beamforming and its threshold  $B_t$ .

the average estimation errors of wind velocity versus the range processed with the nonadaptive beamforming and the NC-DCMP algorithm, respectively. Note that ranges in 74 – 84 km are extracted in this figure. Thin lines shows the standard deviation of the estimation error for each range.

### Comparison of the deflection ratio

Table 2.5 shows that the NC-DCMP algorithm discards only about one-third of the spectra discarded by the nonadaptive beamforming through thresholding in incoherent integration. Additionally, comparing Figs. 2.8 and 2.9, it is clear that the number of peaks in spectra processed by the NC-DCMP algorithm that are considered to be meteor clutters is much less than that in the case of the nonadaptive beamforming. The average suppres-

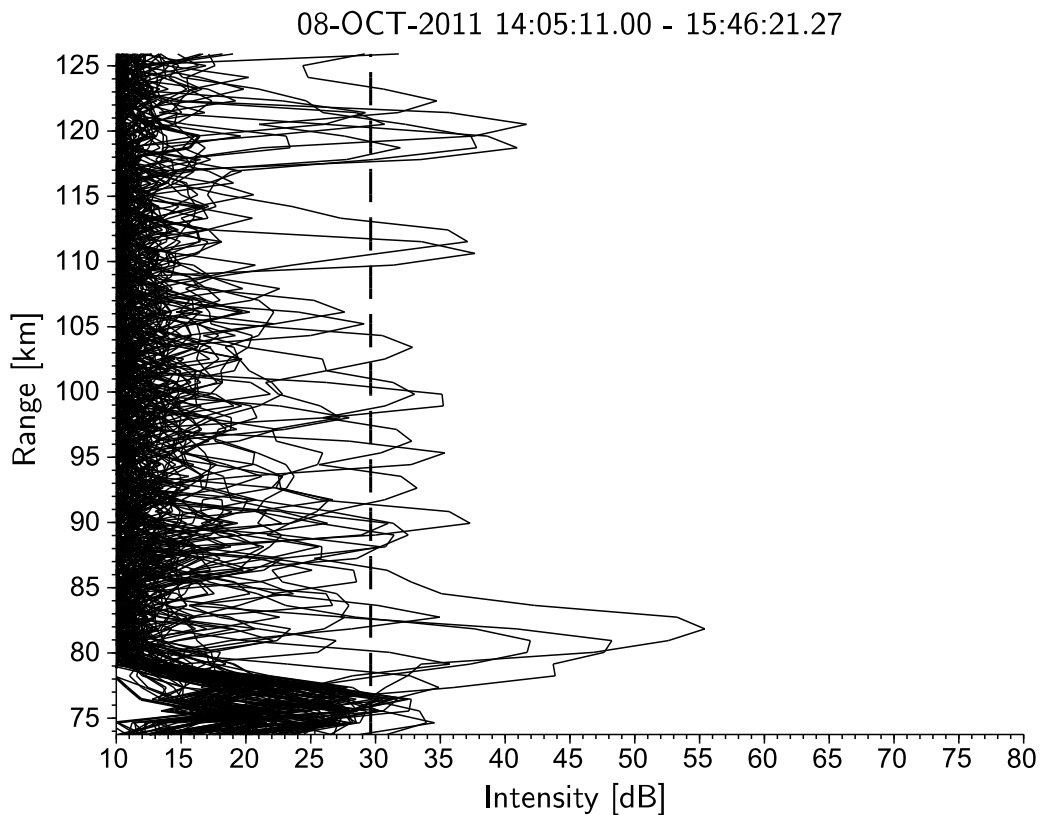


Figure 2.9: Overlaid spectral peaks processed by the NC-DCMP algorithm and its threshold  $B_t$ .

sion ratio of meteor clutters is nearly 15 dB, which is the same result as for simulation 1 in section 2.4.

### Differences in wind velocity estimation

As seen in Fig. 2.10, the standard deviations of the average wind velocities estimated with the NC-DCMP algorithm are much lower than those estimated with the nonadaptive beamforming at 73.7 km and 78 – 80 km. These ranges are considered to be the boundary regions where atmospheric echoes are weak and meteor clutters are dominant. Above these regions, atmospheric echoes cannot be observed because of the limitation of the current radar system. Therefore, it can be concluded that the NC-DCMP algorithm recovered the whole observable ranges that were not available with the conventional

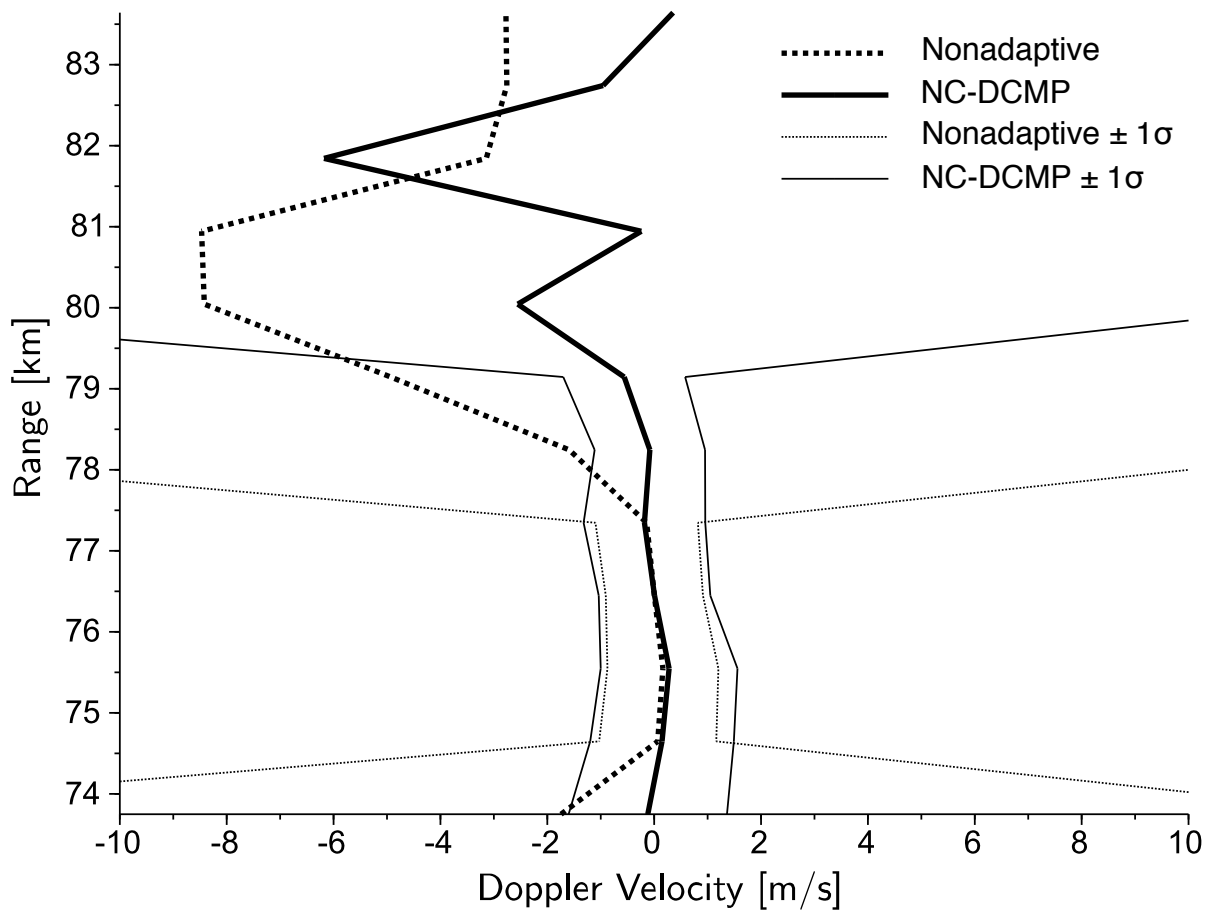


Figure 2.10: Estimated wind velocity for each range obtained by the nonadaptive beam-forming and NC-DCMP algorithm.

Table 2.5: Threshold  $B_t$  for discarding contaminated spectra in incoherent integration, the defection ratio  $R_d$  with thresholding and the equivalent number of incoherent integration  $\hat{N}_i$  for the observation.

	nonadaptive	NC-DCMP
$B_t$	31.4 dB	28.6 dB
$R_d$	13.5 %	4.37 %
$\hat{N}_i$	$\simeq 32.9$	$\simeq 36.3$

spectral thresholding.

## 2.6 Summary and concluding remarks

In this chapter, the result of applying an adaptive meteor-clutter rejection technique to an actual mesosphere observation has been presented.

In section 2.4, results from two numerical simulations are presented. The first one examined the clutter suppression capability of the NC-DCMP algorithm in a simplified situation. The NC-DCMP algorithm reproduced the desired signals well at the SNDRs above 5 dB, i.e., SIDR of  $-5$  dB, which is an improvement of 15 dB compared with the result of the ordinary non-adaptive beamforming method. The second one was a more realistic simulation of a mesosphere observation. In this case, the wind velocity estimated using the NC-DCMP algorithm were with RMS error of less than  $1.5 \text{ m s}^{-1}$  with the SIDR of  $-10$  dB, and the spectral fitting was successful for ranges four times as wide as in the case of the nonadaptive beamforming method.

In section 2.5, the NC-DCMP algorithm was applied to an actual observation made on October 8 th 2011 by the MU radar. The NC-DCMP algorithm suppressed meteor clutters by about 15 dB on average, and the number of spectra discarded through spectral thresholding in incoherent integration with the NC-DCMP algorithm was about one-third of the number for the nonadaptive beamforming method. Additionally, the standard deviation of the wind velocity estimation was less than  $2 \text{ m s}^{-1}$  for ranges twice as wide those for the conventional method; i.e., the observable range doubled.

The above simulation and observational results show that the NC-DCMP algorithm is a good solution for mesosphere observations contaminated by meteor clutters.

# Chapter 3

## Adaptive sidelobe cancellation technique for atmospheric radars containing arrays with nonuniform gain

### 3.1 Introduction

As shown in Chapter 2, the NC-DCMP algorithm is effective method to suppress meteor trail echoes in mesosphere. In this case, the main array is divided into equal-sized subgroups, and outputs of these subarrays are synthesized using a weight vector with each component aligned with the same order of magnitude, since each subarray has a similar directional gain function. Such systems are referred to as the uniform-gain configuration hereafter. Modern atmospheric radars commonly have the uniform-gain subarrays, e.g., Hassenpflug et al. (2008); Latteck et al. (2012); Sato et al. (2014).

However, clutter is usually present at low elevation angles. In addition, the noise power increase caused by adaptive beamforming is known to become large as the degree of freedom of the array increases Compton (1982). Therefore, it is considered to be more efficient to add a small number of supplemental antennas that have a high response to low elevation angles, instead of dividing a large array into uniform shapes. Adaptive arrays for such nonuniform-gain configurations are known as partially adaptive arrays (Chapman, 1976; Morgan, 1978; Van Veen and Roberts, 1987), and were first applied to atmospheric radar observations by Kamio and Sato (2004). Although their developed method (hereafter referred to as the Kamio method) shows that partial adaptivity is effective for atmospheric radars, it requires the gain differences between the main and sub array to be large enough. Hence, the systems that can use the Kamio method has been limited. In addition, the performance difference between the configurations with

uniform and nonuniform gain has not yet been studied.

To address these problems, this chapter provides the design and performance evaluation of an adaptive clutter suppression technique for nonuniform-gain array configurations. In section 3.2, the method for applying the NC-DCMP algorithm on partial adaptive arrays is presented. The developed method is based on the NC-DCMP algorithm (Kamio and Sato, 2004), with the gain weighting determined by the gain differences in the desired direction. In section 3.3, the NC-DCMP algorithm on uniform-gain and nonuniform-gain configurations are compared using numerical simulations. In section 3.4, these configurations are examined in actual observations from the MU radar.

## 3.2 Adaptive beamforming technique for nonuniform-gain array

In this section, two adaptive beamforming methods for atmospheric radars with nonuniform-gain array are introduced; the original NC-DCMP algorithm introduced by Kamio and Sato (2004) and the gain-weighted NC-DCMP algorithm (Hashimoto et al., 2016).

### 3.2.1 Kamio's Method

Kamio and Sato (2004) first applied the NC-DCMP algorithm to the atmospheric radar with the nonuniform-gain configuration. The target system has a high-gain main array supplemented by additional low-gain antennas. In such a system, the weight for the main array is kept at 1, and only the sub-array weights are changed. This constraint prevents the use of the simple diagonal loading technique, so they used the penalty function method (e.g., McWhirter, 2000) to obtain the solution.

The problem of the penalty function method is its high computational cost. However, several authors have shown that the solution can be simplified according to the assumption on which the method is based; the gain differences between the main and sub arrays are large enough (e.g., Curtis et al., 2016; Hashimoto et al., 2016). By using this assumption, the alternative directional constraint  $C = [1, 0, 0, \dots]$  and constraint response  $H = 1$  can be adopted in Eq. (1.51). This enables the diagonal loading approach again, which is mentioned in Eq. (1.54). The method is described as the norm-constrained PIAA algorithm in this case (Compton, 1979).

### 3.2.2 Gain-weighted NC-DCMP algorithm

If the assumption about the gain difference in section 3.2.1 fails, the norm constraint for the sub array may become too large, causing the increase of the noise level, or the cancellation of the desired signal. Therefore, the target radar system has been limited to those with large gain differences for the Kamio method.

Here, the NC-DCMP algorithm is extended to work with any nonuniform gain array by introducing proper gain weighting into the directional constraint. Suppose there are multiple receiver channels with arbitrary gains to the desired direction  $(\theta_o, \phi_o)$ :

$$\mathbf{G}(\theta_o, \phi_o) = [G_1(\theta_o, \phi_o), G_2(\theta_o, \phi_o), \dots]^T \quad (3.1)$$

By integrating Eq. (3.1) into Eq. (1.51), each element  $\hat{C}_i (i = 1, \dots, M)$  of the modified directional constraint  $\hat{\mathbf{C}} = [\hat{C}_1, \hat{C}_2, \dots]^T$  is defined as follows:

$$\hat{C}_i = \sqrt{\frac{G_i(\theta_o, \phi_o)}{\|\mathbf{G}(\theta_o, \phi_o)\|}} A_i(\theta_o, \phi_o), \quad (3.2)$$

$$\|\mathbf{G}(\theta_o, \phi_o)\| = \frac{1}{M} \sum_{i=1}^M G_i(\theta_o, \phi_o).$$

Note that  $\hat{\mathbf{C}}$  is still appropriately normalized, so Eq. (3.2) can be used with Eq. (1.51) without any modification. It can also be shown that  $\hat{\mathbf{C}} \rightarrow [1, 0, \dots, 0]^T$  when  $G_1 \gg G_2 \dots G_M$ .

The gains of the sub-array antennas to the clutter direction is another important design factor for the algorithm. Since the gain weighting reduces the contribution of the sub array, the clutter suppression capability depends on the gains of them to the clutter direction. Therefore, it is more preferable that the gains between the main and sub array are orthogonal, i.e., the sub-array antennas do not have the response to the desired direction, and have high gain to low elevation angles. With such gain differences, the method will better realize the original sub-array NC-DCMP algorithm (Kamio et al., 2004; Kamio and Sato, 2004).

## 3.3 Performance evaluation with numerical simulations

### 3.3.1 System model

The simulation model has two antenna arrays, the “main array” and “sub array”. Figure 3.1 shows the arrangement of antennas of the radar system. This is based on the MU

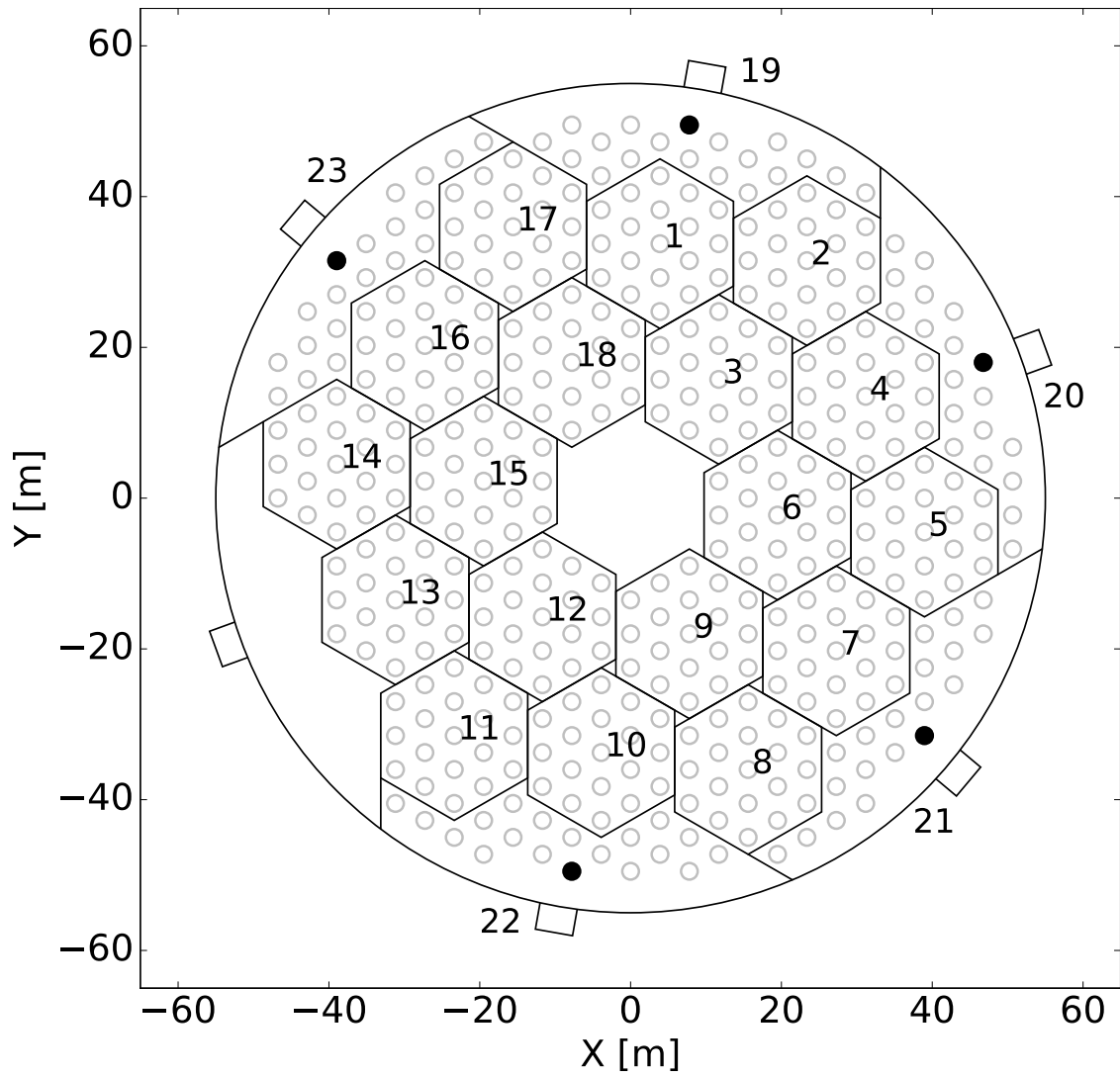


Figure 3.1: Antenna position and channel number assignment of the MU radar for both simulation and observation. The five black circles in the outer groups are sub-array antennas used in types B and C.

radar in section 2.2.

For the main array, 18 groups from the center of the MU radar is selected, which are indicated by the hexagons in Fig. 3.1. Each element is a three-element crossed Yagi antenna, and the receiver outputs from each of 19 elements in a group are combined in-phase. The total directional gain of the main array in the azimuth section at  $\phi = 0^\circ$  is shown as the solid line (Main) in Fig. 3.2. The dotted line (Hex) represents the directional gain of a hexagonal sub array in the main array. The main array is used as a six-channel uniform-gain array, or one high-gain array. For the six-channel uniform-gain array, each of the nearest three groups arranged in a regular triangle  $3i - 2, 3i - 1, 3i$  ( $i = 1, 2, \dots, 6$ ) are synthesized in-phase. For the high-gain array, outputs from all hexagons are uniformly synthesized.

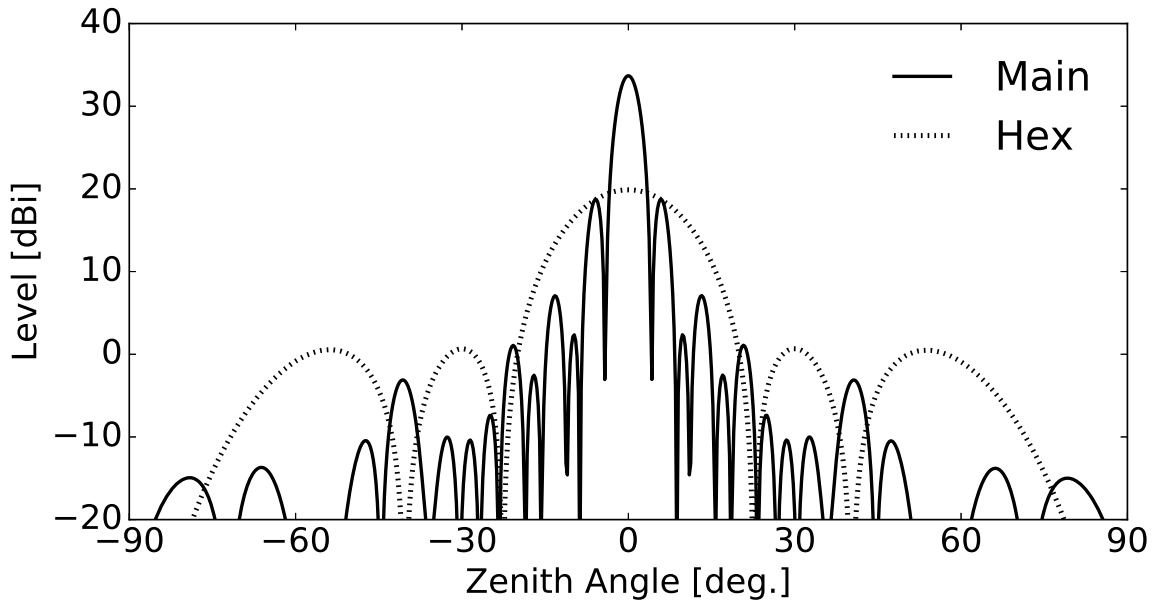


Figure 3.2: Azimuth section of one-way directional gains at  $\phi = 0^\circ$  for the main array (Main), and one of the main array channels consisting of 19 crossed Yagi antennas indicated by a hexagon in Fig. 3.1 (Hex).

For the sub array, three different configurations, A, B and C are considered in this simulation. The directional gain in the azimuth section at  $\phi = 0^\circ$  for the channel number 19 of configurations A, B, and C are shown by the dotted (A), solid (B), and dashed (C) lines in Fig. 3.3, respectively. Type A uses outer five groups of the MU radar as the

sidelobe canceller array, which are indicated as 19 – 23 in Fig. 3.1. Each sub-array group consists of 19 elements, which uses the same element as the main array. Type B uses only one element from each outer group, indicated by black circles in Fig. 3.1. Each element is the same as that of the main array. Type C also uses the same element arrangement as type B, except that each element is modeled as a half-wavelength turnstile antenna placed at half wavelength above the ground. Note that type C is considered in this simulation because the ideal element gain function for the sub array should have an orthogonal response in the beam pattern of the main array, as mentioned in section 3.2.2. As illustrated in Figs. 3.2 and 3.3, the directional gains of main and type C element are roughly orthogonal.

Other radar settings are listed in Table 3.1. Details about these observation parameters are explained in section 3.3.2.

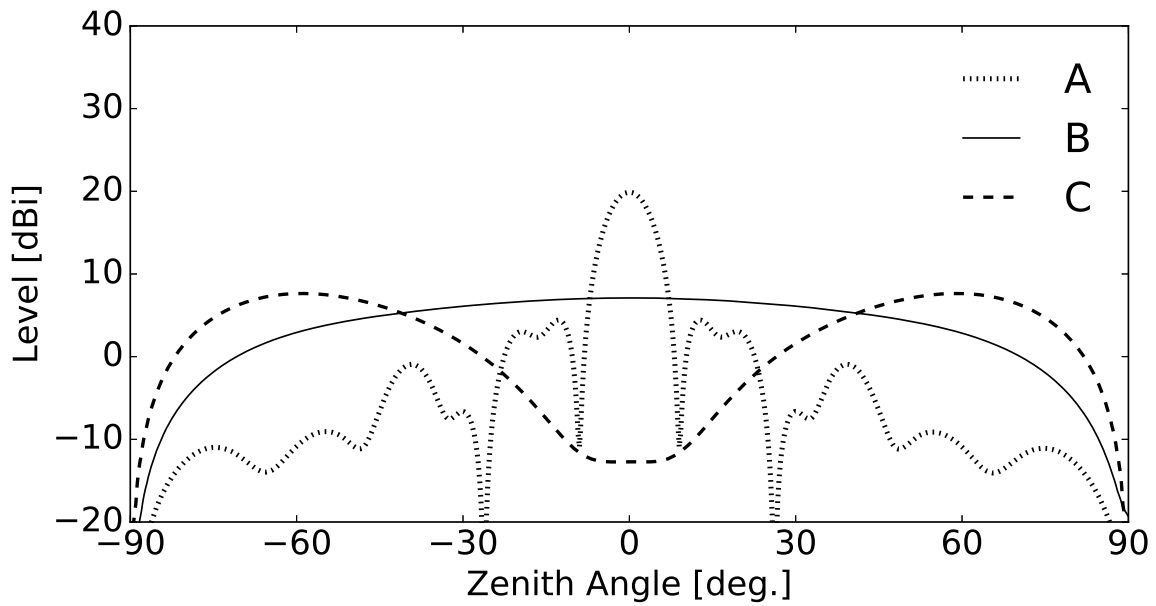


Figure 3.3: Azimuth section of one-way directional gains at  $\phi = 0^\circ$  for one of the sub-array groups of type A (dotted), B (solid), and C (dashed).

Table 3.1: Observational parameters of the MU radar.

Center frequency	46.5 MHz
IPP	400 $\mu$ s
No. beams	5
Pulse code	8-bit Spano codes
No. pulse sequence	16
Time resolution	32 ms
Range resolution	150 m
Ranges	1.5 – 25 km
No. time samples $N_t$	1024

### 3.3.2 Signal generation

In this simulation, there are three kinds of signals: atmospheric echoes, ground clutter and noise. For the atmospheric echoes, the desired direction  $(\theta_o, \phi_o)$  is set to  $(0^\circ, 0^\circ)$ , and the average peak power of atmospheric echoes  $P_S$  is set to 20 dB over the noise floor level  $P_N = 1$ . The spectral width  $\sigma_d$  is  $1 \text{ ms}^{-1}$ , and the Doppler shift  $v_d$  is set to  $1 \text{ ms}^{-1}$ . For the ground clutter, five point-like sources around the radar are designed. The average power from each source  $P_{T,i}$  ( $i = 1, \dots, 5$ ) is 60 dB over the noise floor level  $P_N$ . The distance from the radar to each source is 10 km. Directions to each source  $(\theta_i, \phi_i)$  are determined by the uniform random numbers for each observation:  $[60^\circ, 80^\circ]$  for  $\theta_i$  and  $[0^\circ, 360^\circ)$  for  $\phi_i$ . Noise is modeled as complex random numbers which follows the Gaussian distribution with averaged power  $P_N = 1$ , assuming galactic noise. For the detailed signal generation procedure, see section 2.3. Note that the clutter signal only depends on the incident angle  $(\theta_j, \phi_j)$ , because each ground clutter signal is modeled as a stationary source and its location is independent of time.

#### Time series of received signals and covariance matrix

Time series of input signals are sampled at discrete intervals for digital signal processing. Input signals  $\mathbf{X}(k)$  at sample time  $k = 1, 2, \dots$  are defined by the sum of signals from all sources:

$$\mathbf{X}(k) = \mathbf{s}(k) + \sum_{j=1}^5 \mathbf{u}_j(k) + \mathbf{n}(k), \quad (3.3)$$

where  $\mathbf{s}(k)$  is the atmospheric time series,  $\mathbf{u}_j$  is the clutter time series from  $j$ -th clutter source, and  $\mathbf{n}(k)$  is the noise time series. The covariance matrix of input signals  $\mathbf{R}(k)$  is

estimated by the time averaging of  $2N_w + 1$  snapshots around the current sample time  $k$ :

$$\mathbf{R}(k) = \sum_{k_i=k-N_w}^{k+N_w} \mathbf{X}(k_i)\mathbf{X}^H(k_i), \quad (3.4)$$

where  $N_w = 512$  in this simulation.

As in Table 3.1, the IPP is  $400 \mu\text{s}$ . For every IPP, the observation direction is changed to five different beam directions, as mentioned in section 1.5.1. In addition, 8-bit Spano code (Spano and Ghebrebrhan, 1996a,b) is used; 16 consecutive pulses are coherently integrated for the pulse compression, making the sampling interval 32 ms. Hence,  $2N_w + 1 = 1025$  snapshots are equivalent to about 32 s.

### 3.3.3 Signal processing

Signals generated by the following four different configurations are processed by the adaptive beamforming methods explained in section 3.2. The configurations are: the six-channel uniform-gain array, six-channel nonuniform-gain arrays of type A, B, and C. For the uniform-gain configuration, the standard NC-DCMP algorithm is applied. For the nonuniform-gain configurations A, B, and C, both the gain-weighted NC-DCMP algorithms and Kamio method (Kamio et al., 2004) are applied, so seven different configurations in total are compared in this simulation. For the gain-weighted NC-DCMP algorithm, the gain weighting coefficients are determined by the gain differences to the desired direction. The gain difference between the main and a sub-array group is 19 : 1 for type A, 342 : 1 for type B, and 24775.7 : 1 for type C.  $H$  is set to 1, and  $U$  is set to about 1.12, which is equivalent to limiting the SNR loss to less than 0.5 dB.

Once optimal weights are obtained, the power spectrum density is estimated by the incoherent integration using  $N_i = 8$  successive periodograms. As shown in Eq. (1.53), the noise floor increase is proportional to the squared norm of the optimal weight. Because each periodogram uses  $N_f = N_t/N_i$  weight vectors, the factor of the noise floor increase  $\hat{L}_m$ , for the  $m$ -th periodogram  $S_m(v)$  ( $m = 1, \dots, 8$ ), can be estimated as follows:

$$\hat{L}_m = \frac{1}{N_f} \sum_{k_m} \|\mathbf{W}(k_m)\|^2, \quad (3.5)$$

where  $k_m = k + N_f(m - 1)$  for  $k = 1, 2, \dots, N_f$  represents the  $k$ -th index in the  $m$ -th periodogram. The noise floor increase can be corrected by dividing each periodogram  $S_m(v)$  by  $\hat{L}_m$ :

$$\hat{S}_m(v) = S_m(v)/\hat{L}_m, \quad (3.6)$$

where  $\hat{S}_m(v)$  is the periodogram with SNR loss correction. Finally, the periodogram after the incoherent integration of eight successive periodograms,  $\hat{S}(v)$ , is written as:

$$\hat{S}(v) = \sum_{m=1}^8 \hat{S}_m(v). \quad (3.7)$$

### 3.3.4 Statistical evaluation and performance indices

A hundred independent records are generated and the statistical information are collected for all configurations described in the previous section. The clutter suppression ratio (CSR)  $Z$  and SNR loss  $L$  are first calculated from each periodogram and then converted to the performance index  $Q$  by calculating their ratio. The definition of each index is as follows.

$Z$  is defined as the ratio of the clutter peak power compared with that obtained by nonadaptive beamforming:

$$Z = \frac{P_I(\mathbf{W}_{\text{opt}})}{P_I^o}, \quad (3.8)$$

where  $P_I(\mathbf{W}_{\text{opt}})$  and  $P_I^o$  are the clutter power obtained by each signal processing method and nonadaptive beamforming, respectively.  $Z < -60$  dB means that the clutter is completely suppressed, because the clutter peak power is set to 60 dB as mentioned in section 3.3.2.

Meanwhile,  $L$  is defined as the ratio of the decrease of the peak height of atmospheric echoes in the periodogram normalized by the noise level compared with that obtained by nonadaptive beamforming:

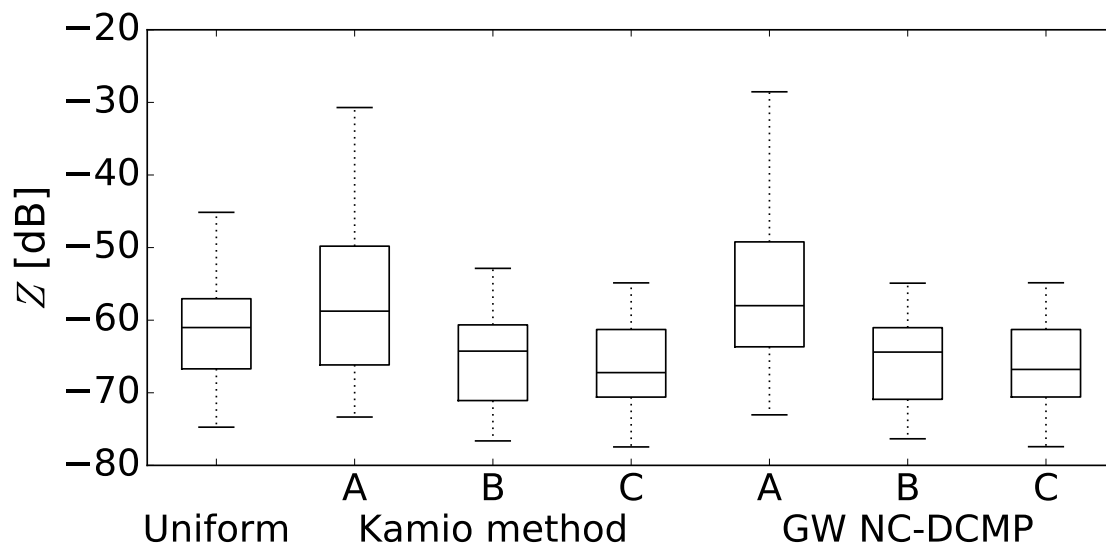
$$L = \frac{P_S^o}{P_S(\mathbf{W}_{\text{opt}})}, \quad (3.9)$$

where  $P_S(\mathbf{W}_{\text{opt}})$  and  $P_S^o$  are the peak power of atmospheric echoes in normalized periodograms obtained by each signal processing method and nonadaptive beamforming, respectively.  $L > 1$  represents the SNR loss factor compared with nonadaptive beamforming, and  $L = 1$  means there is no change in the noise power.

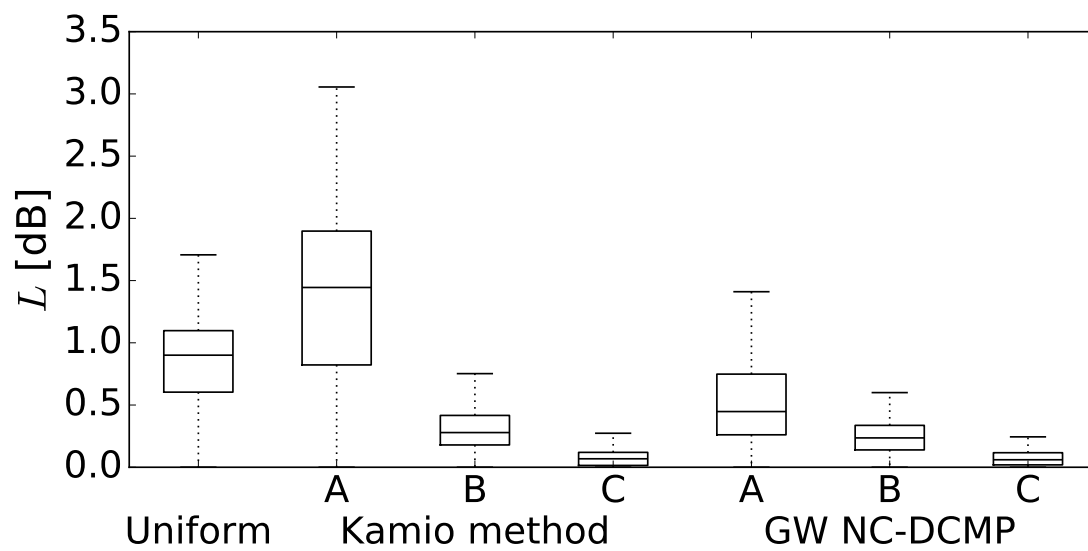
The performance index  $Q$  is defined as:

$$Q = -\log_{10} [Z(L - 1)]. \quad (3.10)$$

Larger  $Q$  represents the better performance.



(a)



(b)

Figure 3.4: (a) Clutter suppression ratio  $Z$  and (b) SNR loss  $L$ .

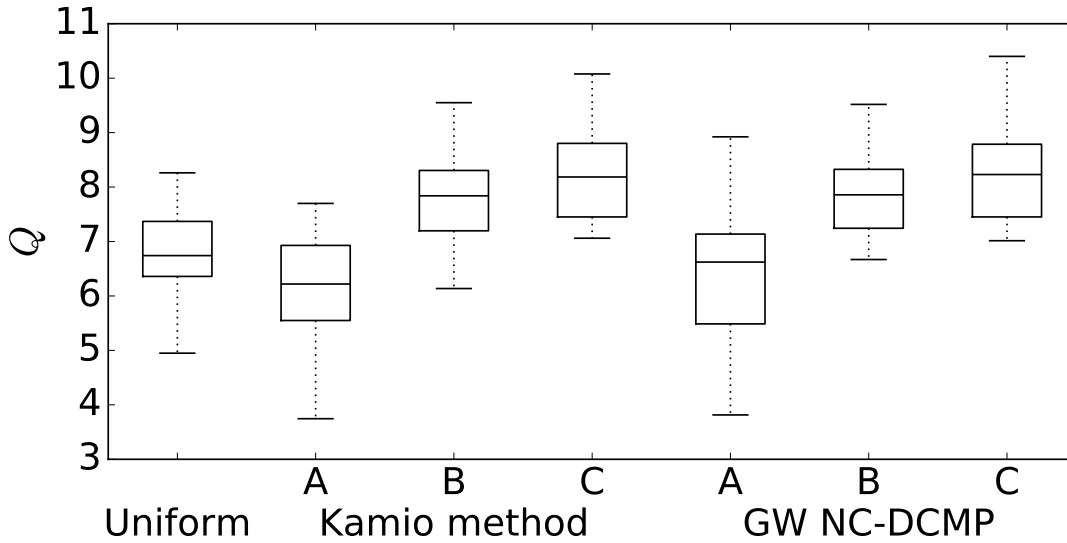


Figure 3.5: Performance index  $Q$ .

### 3.3.5 Results and Discussion

Figures 3.4a, 3.4b and 3.5 display box-and-whisker plots of the clutter suppression ratio  $Z$ , SNR loss  $L$  and performance index  $Q$ , obtained for the seven different configurations, with over 100 results for each configuration. The configurations are, from left to right, uniform-gain NC-DCMP algorithm, Kamio method with the sub-array configurations A, B, and C, and gain-weighted NC-DCMP (GW NC-DCMP) algorithm with A, B, and C. The center line of each box shows the median, the upper and lower edges of the box are the first and third quartiles and whiskers are the upper and lower interquartile ranges.

As shown in Fig. 3.4a, the average clutter suppression ratios are below  $-60$  dB for most of the methods and configurations, which means that the clutter is almost perfectly suppressed. On the other hand, as illustrated in Fig. 3.4b, large SNR losses can be observed in the uniform-gain NC-DCMP algorithm and Kamio method with the nonuniform-gain configuration A. Namely, the average SNR losses are about 0.86 dB and 1.38 dB for the uniform-gain NC-DCMP algorithm and Kamio method A, respectively. The performance indices  $Q$  for these cases are 6.81 and 6.06 for the uniform-gain configuration and the Kamio method A, respectively. In the uniform-gain configuration, each channel of the main array consists of 19 crossed Yagi antennas with the same element gain functions. In addition, the alignment of antennas in a group are almost all the same, which makes the reception beam patterns close to each other. Thus, if there is clutter from a direction where a high sidelobe exists, it is difficult to suppress it within a designated norm constraint. On the other hand, the performance degradation of the

Kamio method with the configuration A is attributed to the directionality pattern of the sub array. As in Fig. 3.3, the directionality pattern of the each group of the type A has lower response to low elevation angles, compared with configurations B or C. This makes it difficult to suppress clutter in low elevation angles within a small norm constraint. In addition, the response to the desired direction of the sub array is relatively high in this configuration. As mentioned in sections 3.2.1 and 3.2.2, the gain differences between the main and sub arrays must be large for the Kamio method, which is not satisfied in this case.

In contrast, the gain-weighted NC-DCMP algorithm with the configuration A exhibits low SNR losses, namely about 0.5 dB in average, which is the same order as the permissive SNR loss designated in this simulation. Therefore, the gain-weighted NC-DCMP algorithm can limit the SNR loss as desired with any nonuniform-gain arrays. However, it should be noted that an SNR loss of 0.5 dB is equivalent to a transmitter power loss of 11 %, which is roughly proportional to the total cost of the radar system. For atmospheric radars that detect extremely weak scattering echoes, the SNR loss of 0.5 dB is not satisfactorily small.

The configuration B is more preferable in this point of view. The average SNR losses are 0.31 and 0.24 dB for the Kamio method and the gain-weighted NC-DCMP algorithm, respectively, as shown in Fig. 3.4b.  $Q$  results in 7.80 and 7.92 for these methods, as shown in Fig. 3.5. Above difference of  $Q$  is caused by the treatment of the antenna gains of the sub array. As shown in Figs. 3.2 and 3.3, the main array and a sub-array antenna of type B have a gain difference of about 30 dB. However, it is not large enough for the Kamio method in terms of the assumption about the gain difference stated in section 3.2.1. In contrast, the gain-weighted NC-DCMP algorithm tolerates such a gain difference.

Of course, the configuration C is the best system design, if available, because the sub array is working as an ideal sidelobe canceller. The configuration C shows  $Q = 8.41$  for the Kamio method and  $Q = 8.44$  for the gain-weighted NC-DCMP algorithm, as shown in Fig. 3.5. This result is consistent with the original concept of the Applebaum sidelobe canceller (Applebaum and Chapman, 1976). However, not all systems may have such ideal gain differences. It is usually difficult to change the element pattern of an existing radar system. Even with non-ideal gain-differences, however, the gain-weighted NC-DCMP algorithm works properly, as seen in the configurations A and B.

From the above discussion, it can be concluded that the gain-weighted NC-DCMP algorithm can sufficiently suppress the clutter at low elevation angles with smaller SNR loss than the uniform-gain NC-DCMP algorithm or the Kamio method. In addition, the gain-weighted NC-DCMP algorithm is shown to have a great flexibility to be applied to

any radar systems with non-ideal gain differences. These characteristics are confirmed in the next section by an actual observation obtained with the same settings as this simulation.

## 3.4 Application to actual observations

### 3.4.1 Observation Settings

An observation was made on July 2, 2015 by the MU radar at Shigaraki, Japan. The observation settings are exactly the same as those mentioned in section 3.3.1. There are five-element sidelobe-canceller array with type B element whose directional gain is shown as B in Fig. 3.3. Note that these sub-array antennas are chosen from existing parts of the array, so the element gain function cannot be changed as in the simulation in section 3.3.

As mentioned in section 3.3.2, the duration of each record is about 32 s. 110 records taken from 18:00 to 19:00 (LT) are used. The observation has five beam directions, and the north beam is used, i.e. the beam direction (zenith, azimuth) =  $(10^\circ, 0^\circ)$ .

### 3.4.2 Signal Processing

Two array configurations are considered: the six-channel uniform-gain array and the six-channel nonuniform-gain array with type B elements. The uniform-gain NC-DCMP, the sub-array NC-DCMP developed by Kamio et al. (2004), and gain-weighted NC-DCMP algorithms are applied to each configuration. Note that signals for each channel are normalized by its noise level before each signal processing method is applied. For this observation, the norm constraint of  $U = 1.5$  is used, which is equivalent to a permissive SNR loss of about 1.76 dB. This is the same selection as in Kamio et al. (2004). Other signal processing parameters are the same as those described in section 3.3.1.

### 3.4.3 Performance Evaluation Method

Similar performance indices to those introduced in section 3.3.4 can be defined for the observation. The most important difference is that there are ranges where the detectable signals or clutter do not exist. To filter these ranges out, the detectability threshold  $T_D$  in Eq. (1.32) is first applied to find the ranges with signal of interest.

The CSR,  $Z$ , is then calculated using Eq. (3.8) for the ranges where  $P_I^o > T_D$ . The SNR loss,  $L$ , can also be defined as Eq. (3.9) for the ranges where  $P_S^o > T_D$ . However, the peak positions of the atmospheric echoes need to be estimated, unlike those of the stationary

clutter. To do this, the periodograms obtained by the uniform-gain NC-DCMP algorithm are used, because the ground clutter are sufficiently suppressed in this configuration. For each periodogram obtained by the uniform-gain NC-DCMP algorithm, the position of the largest peak is searched. Then,  $L$  is calculated by Eq. (3.9) using the peak power at this position. The performance index  $Q$  is calculated using Eq. (3.10).

### 3.4.4 Results and Discussion

Figure 3.6 is an example of the range profiles of the DC component extracted from the periodogram obtained by the nonadaptive beamforming, uniform-gain NC-DCMP algorithm and gain-weighted NC-DCMP algorithm. The horizontal axis shows the intensity of the ground clutter, and the vertical axis is the range in km. The result of the Kamio method is almost the same as that of the gain-weighted NC-DCMP algorithm, so it is omitted for simplicity. Figure 3.7 is an example of the range section at 5 km. The range is indicated by a horizontal line in Fig. 3.6. The horizontal axis is the Doppler velocity and the vertical axis is the intensity. Bases of the decibel values are the noise level in Figs. 3.6 and 3.7. Figure 3.8 summarizes the CSR  $Z$ , SNR loss  $L$  and performance index  $Q$  for each signal processing method throughout the observation. The center line of each box shows the median, marks are the means, upper and lower edges of the box are the first and third quartiles, and whiskers are the upper and lower interquartile ranges. To obtain statistical results, 94 ranges from each record are used, so 10340 periodograms in total are averaged.

First, in Fig. 3.6, the gain-weighted NC-DCMP algorithm and uniform-gain NC-DCMP algorithm show similar range profiles of the DC components. Figure 3.8 also reveals that  $Z$  is reasonably similar for all three methods.

In contrast, the peak power of the atmospheric echo obtained by the uniform-gain configuration is about 1 dB lower than that of the gain-weighted NC-DCMP algorithm, as shown in Fig. 3.7, Therefore, the uniform-gain NC-DCMP algorithm gives a higher SNR loss by about 1 dB, or 21 % in the linear scale, than the gain-weighted NC-DCMP algorithm, which is a substantial difference in sensitivity.

Also, Fig. 3.8 shows that the averaged SNR loss  $L$  obtained by the gain-weighted NC-DCMP algorithm is 1.7 dB, which is 1.0 and 0.3 dB smaller than the corresponding values of the uniform-gain configuration and Kamio method, respectively. The performance index  $Q$  of the gain-weighted NC-DCMP algorithm exhibits in the highest value of 1.20, which is 0.52 and 0.14 higher than those of the uniform-gain configuration and Kamio method, respectively. Note that  $Q$  takes smaller values than the simulation in section 3.3 because of smaller  $Z$ . However, the difference among methods are consistent with those obtained by the simulation in section 3.3.

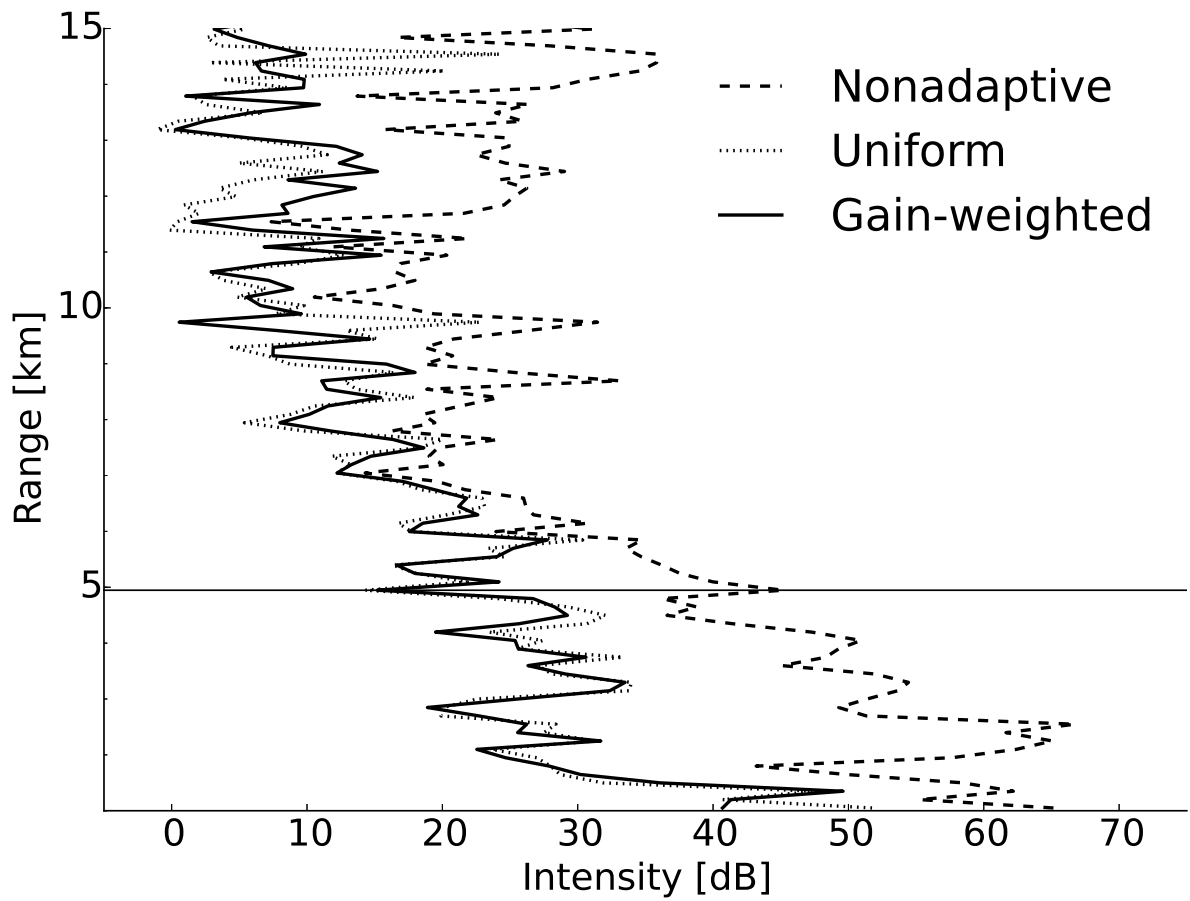


Figure 3.6: Range profile of the DC component obtained by the uniform and gain-weighted NC-DCMP algorithms.

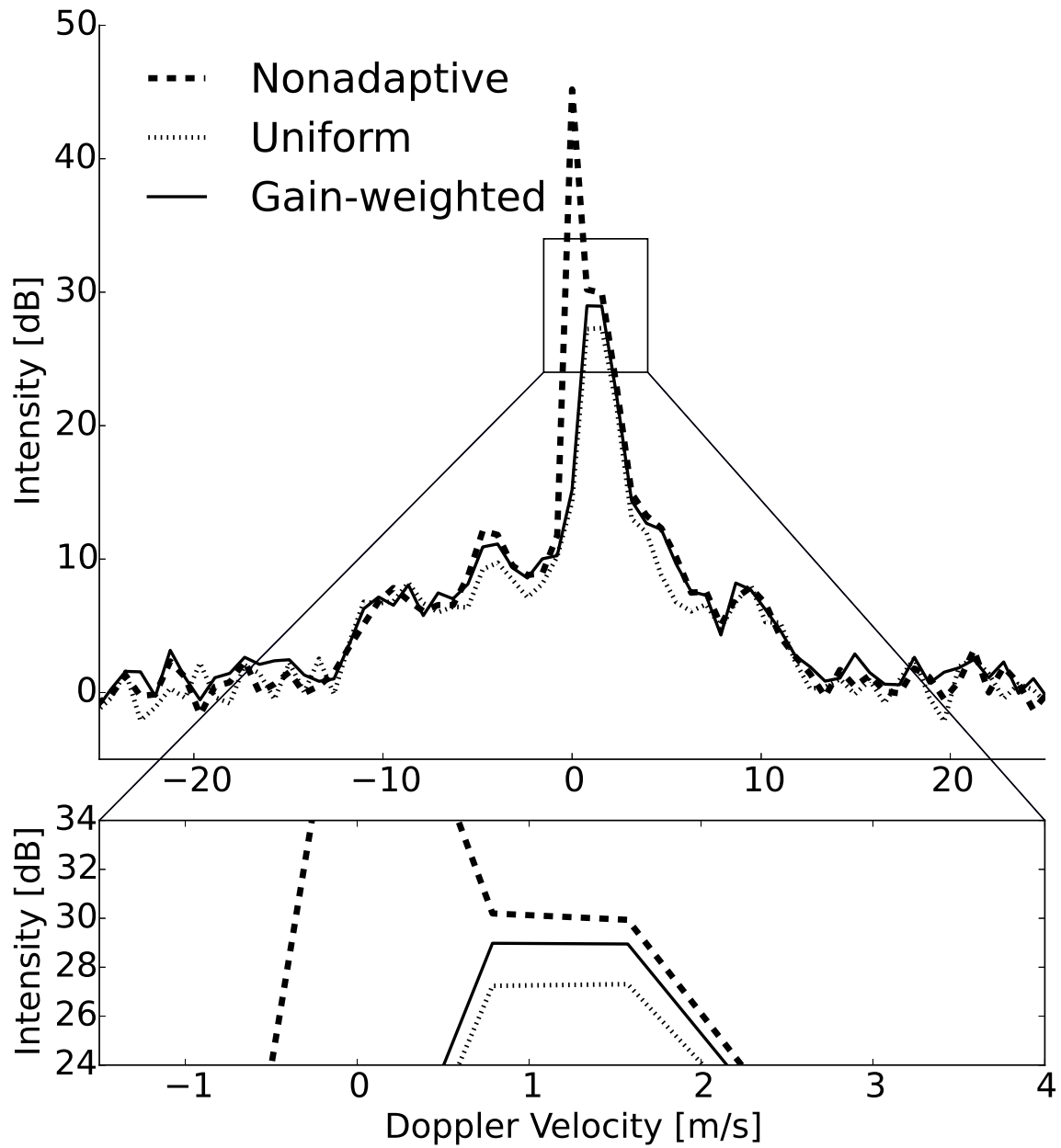


Figure 3.7: Example of the range section at 5 km, which is indicated by a horizontal line in Fig. 3.6.

From the discussion above, it can be concluded that the gain-weighted NC-DCMP algorithm is the best solution for suppressing the ground clutter in actual observations among the three signal processing methods considered herein. The gain-weighted NC-DCMP algorithm can readily suppress the clutter from low elevation angles in actual observations, and the gain weighting limits the SNR loss to a smaller amount than those in other methods. As shown in Fig. 3.5, the best element gain function for the sub-array configuration is the one with the orthogonal directional gain pattern against the main array. However, this is not tested in actual observations of the MU radar, thus requiring the further experiments using such sub-array configurations.

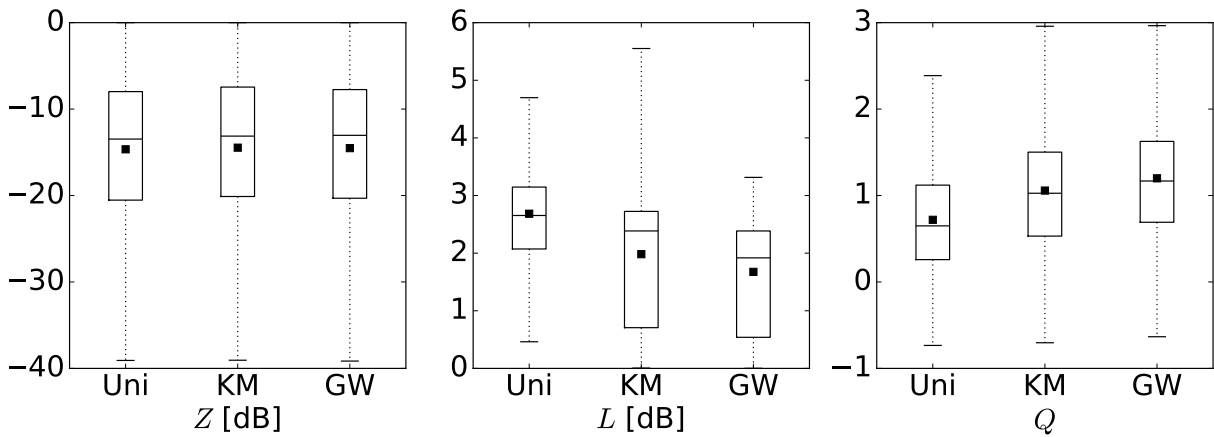


Figure 3.8: Comparison of the performance indices  $Z$ ,  $L$  and  $Q$  for the uniform NC-DCMP algorithm (Uni), the Kamio method (KM), and the gain-weighted NC-DCMP algorithm (GW) throughout the roughly 1-hour duration of observations.

### 3.5 Summary and concluding remarks

An adaptive sidelobe cancellation technique for atmospheric radars with gain weighting on a nonuniform array has been presented. The method introduces gain weighting into the NC-DCMP algorithm in accordance with the gain differences in the desired direction among the receivers.

In section 3.3, the results of the gain-weighted NC-DCMP algorithm was compared with those of the uniform-gain NC-DCMP algorithm and the Kamio method using nu-

merical simulations. The gain-weighted NC-DCMP algorithm gave sufficient clutter suppression capability with smaller SNR loss than the other two methods, even with non-ideal gain differences between the main array and sub-array. In section 3.4, the performance of the gain-weighted NC-DCMP algorithm was also tested using actual observations from the MU radar. The gain-weighted NC-DCMP algorithm gave the best performance compared with the uniform NC-DCMP algorithm or the Kamio method. In particular, the improvement in the average SNR loss given by the developed algorithm is 1 dB (21 %) compared with that of the nonuniform-gain NC-DCMP algorithm, which is substantially different in terms of system sensitivity.

From these results, it can be concluded that the proper gain weighting is effective on suppressing clutter at low elevation angles in atmospheric radars. Also, the flexibility of the algorithm, which handles arbitrary gain differences between the main array and sub-arrays, is suitable for any existing atmospheric radar system.

# Chapter 4

## User parameter-free diagonal-loading scheme for clutter rejection on atmospheric radars

### 4.1 Introduction

In Chapter 3, the gain weighting is introduced to the NC-DCMP algorithm for applying the method on any arrays with nonuniform-gain configurations. Recently, the automatic determination of the diagonal loading level has been extensively studied in the pursuit of robust beamforming; a thorough review was given by Du et al. (2009). According to this article, previous algorithms have mainly focused on robustness against steering vector errors or the poorly estimated covariance matrix using a small number of snapshots. For wind profilers, however, these problems are not as critical. Indeed, the backscattered signals are assumed to be returned solely from the volume in the very sharp mainlobe, and the direction of the center of the volume is that in which the transmitting beam pattern is directed. Therefore, the steering vector for reception is exactly the same as what is used for transmission. Similarly, the duration over which the covariance matrix is averaged can be relatively long (e.g., 1 min), so the number of snapshots is sufficient for estimating the covariance matrix with enough accuracy. Instead, keeping the white noise gain and beam directional errors as small as possible has more impact on wind profilers, which are expected to detect extremely weak signals. For such purposes, however, there are currently no suitable adaptive beamforming techniques that can automatically determine the optimal diagonal loading level.

In this chapter, a novel method to automatically determine the diagonal loading level for robust adaptive beamforming on atmospheric radars is presented. The developed

algorithm estimates the output powers of interference and noise simultaneously, and automatically determines the optimal diagonal loading level that balances the increase in the remaining clutter power with the increase in noise power to maximize the total detectability of the desired signal.

## 4.2 Proposed power balance algorithm

As described in section 1.7.2, the NC-DCMP algorithm has a user-defined parameter  $L_{\text{dB}}$  to obtain the diagonal-loading level. This is not optimal in terms of the signal-to-interference ratio (SIR). Here, a novel algorithm is proposed that automatically determines the optimal diagonal-loading level to balance the SNR and SIR degradations in power spectral density ratios. In this section, the derivations of the SIR and SNR degradations are presented followed by the formulation of the proposed algorithm.

### 4.2.1 Estimation of SNR and SIR degradations

Figure 4.1 shows the output power diagram of the desired signal  $P_S$ , interference  $P_I(\alpha)$ , and noise  $P_N(\alpha)$  obtained using nonadaptive beamforming ( $\alpha_\infty$ ), the standard DCMP algorithm ( $\alpha_0$ ), and an intermediate diagonal-loading level  $\alpha$  in the range  $\alpha_\infty > \alpha > \alpha_0$ . Here,  $\alpha_\infty$  and  $\alpha_0$  are abstract values denoting that results are processed by nonadaptive beamforming and the DCMP algorithm. These notations are used because the nonadaptive beamforming and the DCMP algorithm can be considered as special cases of the diagonal-loading beamformer, in which their weight vectors are calculated using Eq. (1.54) with  $\alpha = \infty$  and  $\alpha = 0$ , respectively. The total output power of the beamformer,  $P_O(\alpha)$ , is written as follows (see also Eq. (1.51)):

$$\begin{aligned} P_O(\alpha) &= P_S + P_I(\alpha) + P_N(\alpha) \\ &= \mathbf{W}^H(\alpha) \mathbf{R} \mathbf{W}(\alpha), \end{aligned} \quad (4.1)$$

where  $\mathbf{W}(\alpha)$  is the optimal weight vector calculated using Eq. (1.54), with a specific diagonal-loading value  $\alpha$ . Note that  $P_S$  is not a function of  $\alpha$ . As mentioned in section 1.7.2, the desired signal is considered to be unchanged by beamforming, especially when applied to a nonuniform-gain configuration. Hence:

$$P_S = P_S(\alpha) = P_S(\alpha_\infty) = P_S(\alpha_0). \quad (4.2)$$

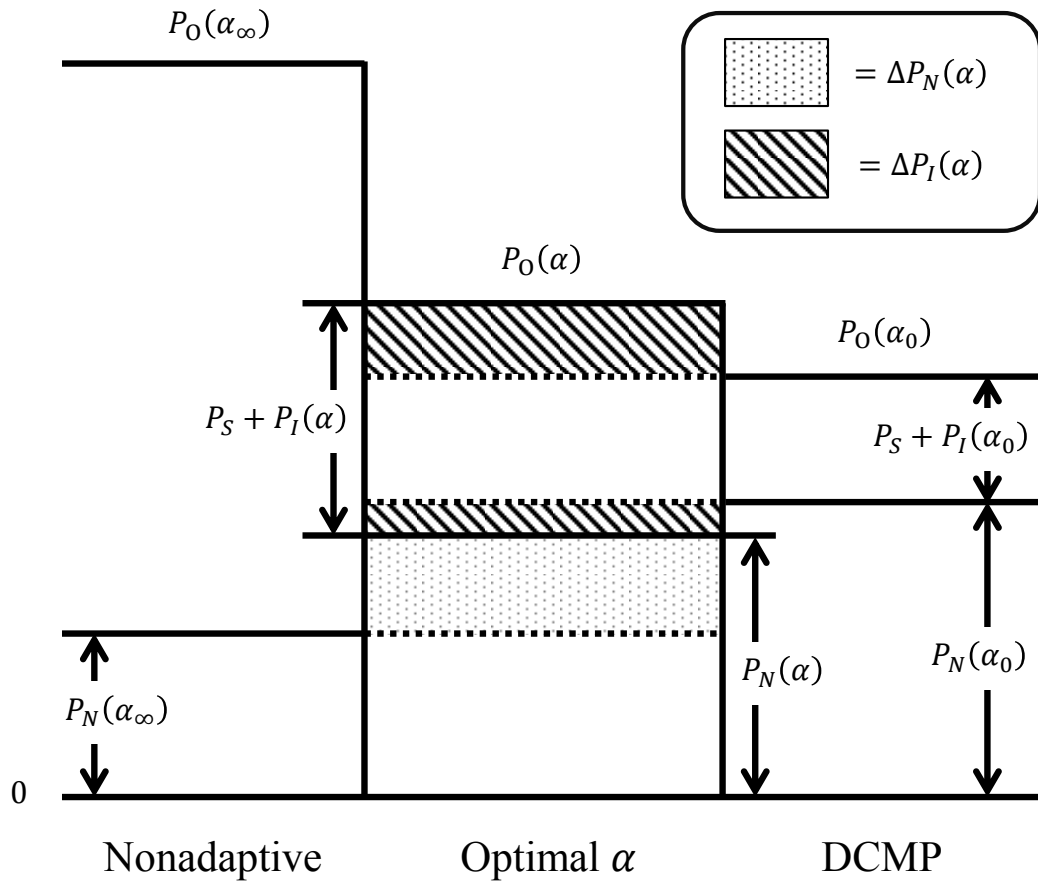


Figure 4.1: Output power diagram for nonadaptive beamforming, the standard DCMP algorithm, and an intermediate diagonal-loading value  $\alpha$ , respectively. Hatched area indicates the SIR degradation compared with the standard DCMP algorithm, and dotted area denotes the SNR degradation compared with nonadaptive beamforming.

## Problems of the DCMP algorithm

One way of maximizing the SINR is to minimize the total output power in Eq. (4.1), because the signal power is unchanged, as stated in Eq. (4.2). Obviously, this describes the DCMP algorithm. Although the DCMP algorithm maximizes the SINR, it is not always optimal in terms of signal detectability. As stated in section 1.5, wind profilers generally use the Doppler spectrum to estimate radial wind velocity. In such applications, it is clearly important to retain detectability of the desired signal, i.e., to ensure that the peak heights of the atmospheric echoes above the noise floor level (Gage and Balsley, 1978) are as high as possible. According to Kamio and Sato (2004), the DCMP algorithm can cause a severe increase in the sidelobe level, when the desired signal is strong. This markedly degrades the detectability of the desired signal because of high white noise gain. Thus, the standard DCMP algorithm is not suitable for atmospheric radar applications.

To address this problem, the residual clutter power and increased noise power must be evaluated separately. In Fig. 4.1, the dotted area denotes the SNR degradation compared with nonadaptive beamforming,  $\Delta P_N(\alpha)$ ; while the hatched area indicates the SIR degradation compared with the standard DCMP algorithm,  $\Delta P_I(\alpha)$ . Below, the derivations of these two quantities are explained.

### SNR degradation

As shown in section 1.7.2, the output noise power is proportional to the norm of the weight vector. Therefore, the noise power obtained using the diagonal-loading value  $\alpha$ ,  $P_N(\alpha)$ , can be written as:

$$P_N(\alpha) = \|\mathbf{W}(\alpha)\|^2 P_N(\alpha_\infty). \quad (4.3)$$

Using Eq. (4.3), the SNR degradation compared to the nonadaptive beamforming,  $\Delta P_N(\alpha)$ , can be written as:

$$\Delta P_N(\alpha) = P_N(\alpha) - P_N(\alpha_\infty) \quad (4.4)$$

$$= (\|\mathbf{W}(\alpha)\|^2 - 1)P_N(\alpha_\infty). \quad (4.5)$$

To calculate  $\Delta P_N(\alpha)$  using Eq. (4.5),  $P_N(\alpha_\infty)$  must be estimated in advance. This is equal to the average power spectral density of the noise, with appropriate normalization. The average power spectral density of the noise  $P_N(\alpha_\infty)$  is estimated using the segment method (Petitdidier et al., 1997), explained in section 1.5.4.

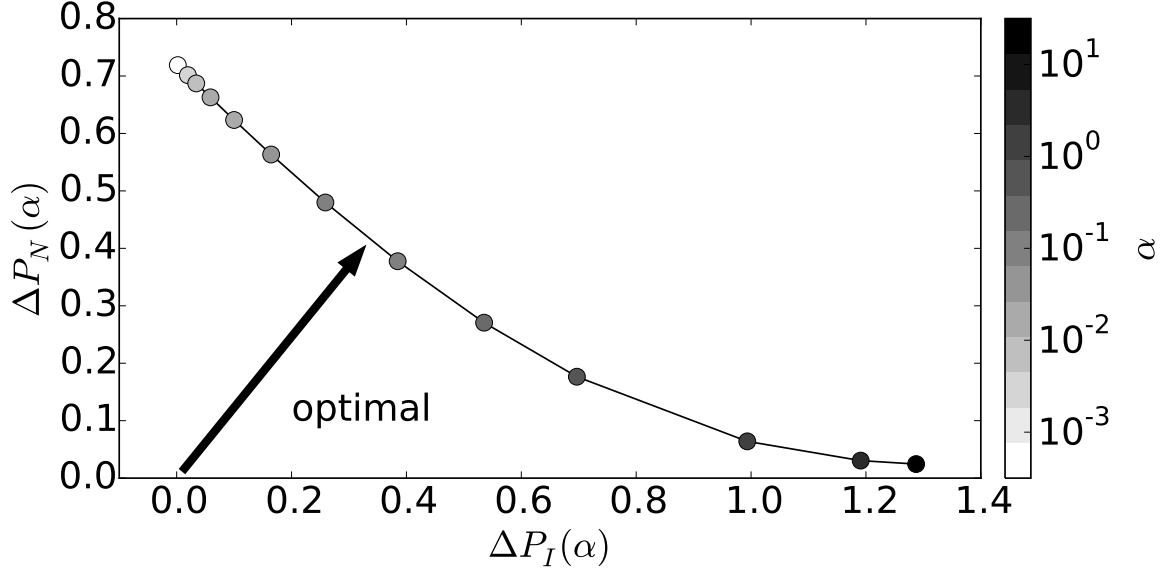


Figure 4.2: Example of the relationship between the SIR degradation factor  $\Delta P_I(\alpha)$  (abscissa) and SNR degradation factor  $\Delta P_N(\alpha)$  (ordinate) for various diagonal-loading values  $\alpha$ . Gray circles indicate the magnitude of  $\alpha$ .

### SIR degradation

The SIR degradation compared with the DCMP algorithm,  $\Delta P_I(\alpha)$ , can be written as:

$$\Delta P_I(\alpha) = P_I(\alpha) - P_I(\alpha_0), \quad (4.6)$$

where  $P_I(\alpha)$  denotes the interference power obtained using the diagonal-loading value  $\alpha$ . In contrast to  $P_N(\alpha)$  in Eq. (4.3),  $P_I(\alpha)$  cannot be directly estimated. However, the difference in the total output power related to the DCMP algorithm can be used to estimate  $\Delta P_I(\alpha)$ :

$$\begin{aligned} P_O(\alpha) - P_O(\alpha_0) &= [P_S(\alpha) + P_I(\alpha) + P_N(\alpha)] \\ &\quad - [P_S(\alpha_0) + P_I(\alpha_0) + P_N(\alpha_0)] \\ &= \Delta P_I(\alpha) + P_N(\alpha) - P_N(\alpha_0). \end{aligned} \quad (4.7)$$

Note that Eq. (4.7) has been simplified using the relationship defined in Eq. (4.2). Rewriting Eq. (4.7) yields:

$$\Delta P_I(\alpha) = [P_O(\alpha) - P_O(\alpha_0)] + [P_N(\alpha_0) - P_N(\alpha)]. \quad (4.8)$$

The first two terms of this equation correspond to the upper hatched area in Fig. 4.1, which is the difference in the total output power. The latter two terms correspond to the lower hatched area in Fig. 4.1, which can be interpreted as the hidden SIR degradation canceled out by the SNR improvement related to employing the larger  $\alpha$ .

### Effects of the diagonal loading on the SNR and SIR degradations

Figure 4.2 shows the relationship between  $\Delta P_N(\alpha)$  and  $\Delta P_I(\alpha)$  for diagonal-loading values  $\alpha$  from  $10^{-3}$  to  $10^{1.5}$ . The horizontal axis represents the SIR degradation compared with the DCMP algorithm,  $\Delta P_I(\alpha)$ , and the vertical axis denotes the SNR degradation compared with the nonadaptive beamforming,  $\Delta P_N(\alpha)$ . The color of the circles on the line represents the magnitude of the diagonal-loading value  $\alpha$ . Note that this example is taken from actual observations of the PANSY radar, outlined further in section 4.5. As in Fig. 4.2, there is a trade-off between the SIR and SNR degradations. Because both have the same dimensions, the residual clutter power and the increased noise power degrade the SINR by the same amount.

### 4.2.2 Formulation of the cost function

In the previous section, the main problem of the DCMP algorithm is first reviewed, and both the SNR and SIR degradations are derived. Now the optimal cost function for the power minimization problem is considered, which is suitable for atmospheric radars.

To balance the clutter suppression capability against signal detectability, the proposed algorithm solves the following minimization problem:

$$\underset{\alpha}{\text{minimize}} \left( f(\alpha) = [\Delta P_N(\alpha)]^2 + [\Delta P_I(\alpha)]^2 \right). \quad (4.9)$$

The optimal solution for Eq. (4.9) is the point on the curve in Fig. 4.2 that minimizes the distance to the origin (labeled as “optimal”). Using this optimal diagonal-loading level, the SNR and SIR degradations are equal, and the SINR in the spectral density ratio, i.e., SINDR, is maximized. Hereafter, this method is called the power balance (PB) algorithm.

As in Eq. (4.9), the sum of squares of the differences between the nonadaptive beamforming,  $\Delta P_N(\alpha)$ , and the DCMP algorithm,  $\Delta P_I(\alpha)$  are used. However, several other cost functions can be considered. One of them is the simple sum of these quantities; in this case, the cost function is written as  $g(\alpha) = \Delta P_N(\alpha) + \Delta P_I(\alpha)$ . Again, this is equivalent to the standard DCMP algorithm, which can be naturally understood by rewriting

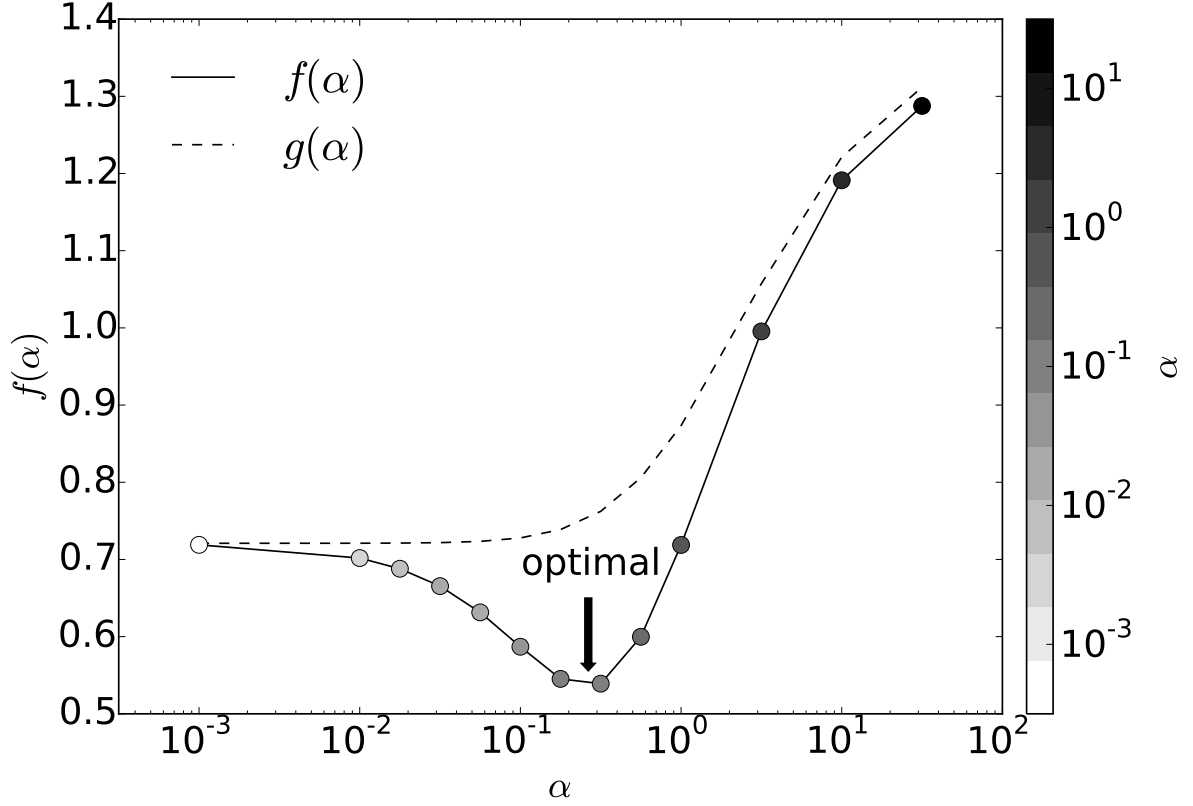


Figure 4.3: Example of the relationship between various diagonal-loading values  $\alpha$  and the cost function of the PB algorithm,  $f(\alpha)$ , and standard DCMP algorithm,  $g(\alpha)$ .

$g(\alpha)$ , using Eqs. (4.4) and (4.8), as follows:

$$g(\alpha) = \Delta P_N(\alpha) + \Delta P_I(\alpha) \quad (4.10)$$

$$= P_O(\alpha) + \delta, \quad (4.11)$$

where  $\delta = -P_O(\alpha_0) + P_N(\alpha_0) - P_N(\alpha_\infty)$  is a constant. Figure 4.3 shows examples of such cost function evaluations for  $f(\alpha)$  and  $g(\alpha)$ . The values used are the same as Fig. 4.2. The abscissa is the diagonal-loading value  $\alpha$ , and the ordinate is the cost function evaluation for the corresponding  $\alpha$ . The solid and dashed lines denote the cost functions  $f(\alpha)$  and  $g(\alpha)$ , respectively. The color of the circles again indicates the magnitude of the diagonal-loading value of  $\alpha$ . As shown in Fig. 4.3, the optimal solution for the standard DCMP algorithm is  $\alpha_0 = 0$ , as  $g(\alpha)$  monotonically decreases as  $\alpha$  de-

creases. As mentioned above, by employing  $\alpha_0$ , the output SINR is maximized, and clutter should be suppressed as well. However, increased noise power density might exceed the peak height of the atmospheric spectrum, and in this case, the signal detectability can be completely lost. In contrast, the proposed PB algorithm evaluates both the amount of the suppressed clutter and the signal detectability separately. As a consequence, the cost function for the proposed algorithm  $f(\alpha)$  reaches a minimum at around  $\alpha \sim 0.3$  (labeled as “optimal”). At this point, signal detectability and clutter suppression are balanced, which eventually maximizes the SINDR.

Another cost function  $h(\alpha)$  can be considered using the fact that the output noise power can be calculated from Eq. (4.3):

$$\begin{aligned} h(\alpha) &= (1 - \gamma) [P_S + P_I(\alpha)]^2 + \gamma P_N(\alpha)^2 \\ &= (1 - \gamma) [P_O(\alpha) - P_N(\alpha)]^2 + \gamma P_N(\alpha)^2, \end{aligned} \quad (4.12)$$

where  $\gamma$  is a scaling factor. The problem with  $h(\alpha)$  is the arbitrariness of  $\gamma$ . In general,  $P_O(\alpha)$  is much larger than  $P_N(\alpha)$  because it contains both powers of the desired signal and clutter. Thus, the scaling factor  $\gamma$  must be set to an appropriate value to balance the clutter suppression against the white noise gain. However, because the ratio of the clutter and desired signal in  $P_O(\alpha)$  is unknown, the scaling factor  $\gamma$  cannot be determined from the radar observations. In contrast,  $\Delta P_I(\alpha)$  and  $\Delta P_N(\alpha)$  are expected to be of the same order, making the PB algorithm free of the scaling factor  $\gamma$ .

### 4.2.3 The procedure for the power balance algorithm

The procedure for the proposed PB algorithm is:

1. Estimate the noise power spectral density ratio using nonadaptive beamforming  $P_N(\alpha_\infty)$ .
2. Calculate the optimal weight of the standard DCMP algorithm  $\mathbf{W}(\alpha_0)$ , the total output power  $P_O(\alpha_0)$ , and the noise power  $P_N(\alpha_0)$ .
3. Find the value of  $\alpha$  that minimizes the cost function  $f(\alpha)$  by solving Eq. (4.9).
4. If  $\alpha$  is greater than the minimum diagonal-loading value  $\alpha_\varepsilon$ , then this is the optimal solution. Otherwise, use  $\alpha_\varepsilon$ .

Here, the minimum diagonal-loading value  $\alpha_\varepsilon$  is used because the loss of the signal power caused by the DCMP algorithm cannot be ignored in some situations, e.g., when the desired signal is very strong and clutter is absent. In these cases, the assumption

about the signal power in Eq. (4.2) will be violated, resulting in an incorrect estimation of the SIR degradation in Eq. (4.8). To inhibit the loss of signal power to a negligible amount,  $\alpha_\varepsilon$  can be calculated as follows:

$$\alpha_\varepsilon = P_N(\alpha_0) - P_N(\alpha_\infty) = \Delta P_N(\alpha_0), \quad (4.13)$$

which is equivalent to the SNR degradation given by the DCMP algorithm. Supposing there is only desired signal and noise, then the loss of signal power is at least larger than  $\alpha_\varepsilon$ , because the total output power of the standard DCMP algorithm must always be smaller than the nonadaptive beamforming. The minimum diagonal-loading value  $\alpha_\varepsilon$  is defined to compensate for this loss.

Now, the computational cost of the proposed PB algorithm is considered. The method is in the class of the nonlinear least-squares problem. Hence, Eq. (4.9) can efficiently be solved using the Levenberg–Marquardt method (Marquardt, 1963). Because Eq. (1.54) is evaluated at every step to find the optimal  $\alpha$ , the difference in the computational cost is proportional to the number of evaluations of Eq. (1.54). In this thesis, the inverse of the diagonally loaded covariance matrix is calculated using the eigendecomposition (Hudson, 1981):

$$(\mathbf{R} + \alpha \mathbf{I})^{-1} = \sum_{i=1}^M \frac{1}{\beta_i + \alpha} \mathbf{U}_i \mathbf{U}_i^H, \quad (4.14)$$

where  $\mathbf{R} = \sum_{i=1}^M \beta_i \mathbf{U}_i \mathbf{U}_i^H$  is the eigendecomposition of the covariance matrix,  $\beta_i$  is the  $i$ -th eigenvalue, and  $\mathbf{U}_i$  is the  $i$ -th eigenvector. Note that in VHF band, galactic noise power is usually large enough to make  $\mathbf{R}$  positive definite, i.e., all  $\beta_i > 0$ . Equation (4.14) enables rapid computation of Eq. (1.54), as eigendecomposition is required only once for each covariance matrix. Thus, the increase in computational complexity for the proposed PB algorithm is small.

Here, an example based on actual observations is presented. Section 4.5 describes the detail of this observation. In this example, each signal block has eight channels, 1024 time samples, and 157 range samples. Because the sampling interval is 51.2 ms, each block must be processed within about 52 s. In the current implementation, the proposed PB algorithm required 2–3 times as many cost function evaluations as the NC-DCMP algorithm. Consequently, the average computational durations were 5.40 s for the PB, 3.68 s for the NC-DCMP, and 2.74 s for the DCMP algorithms on a personal computer capable of 112 billion floating point operations per second. All these computational times were sufficiently shorter than the data interval of 52 s. Therefore, it can be concluded that the computational cost of the proposed PB algorithm is comparable with the conventional NC-DCMP algorithm, and that this method can be used in real-time applications.

In the following section, the performance of the proposed PB algorithm is compared with those of the standard DCMP algorithm and the conventional NC-DCMP algorithm using numerical simulations.

### 4.3 System model

In this chapter, the target radar system is the PANSY radar (Sato et al., 2014). It is a large MST radar at Syowa Station, Antarctic ( $69.01^{\circ}\text{S}$ ,  $39.59^{\circ}\text{E}$ ). The center frequency of the PANSY radar is 47 MHz in the VHF band. The PANSY radar consists of 1045 three-element crossed-Yagi antennas. As shown in Fig. 4.5, the antenna array is divided into 55 subarrays, each consisting of 19 antennas arranged in a hexagon. Output signals from these subarrays can be used separately, as an adaptive array with 55 channels. The block diagram for the signal processing of the PANSY radar is shown in Fig. 4.6. In addition, the PANSY radar has two linear arrays each consisting of 12 three-element Yagi antennas, as shown in Fig. 4.5. Each three antennas are synthesized by nonadaptive beamforming, making the FAI array as eight-channel adaptive array. These are directed to the magnetic south pole to observe the field aligned irregularities, as mentioned in section 1.4.2. Figure 4.4 shows the radiation pattern of each antenna array of the PANSY radar; main, FAI1, and FAI2. This figure shows the azimuth section at  $135^{\circ}$  (SE-NW).

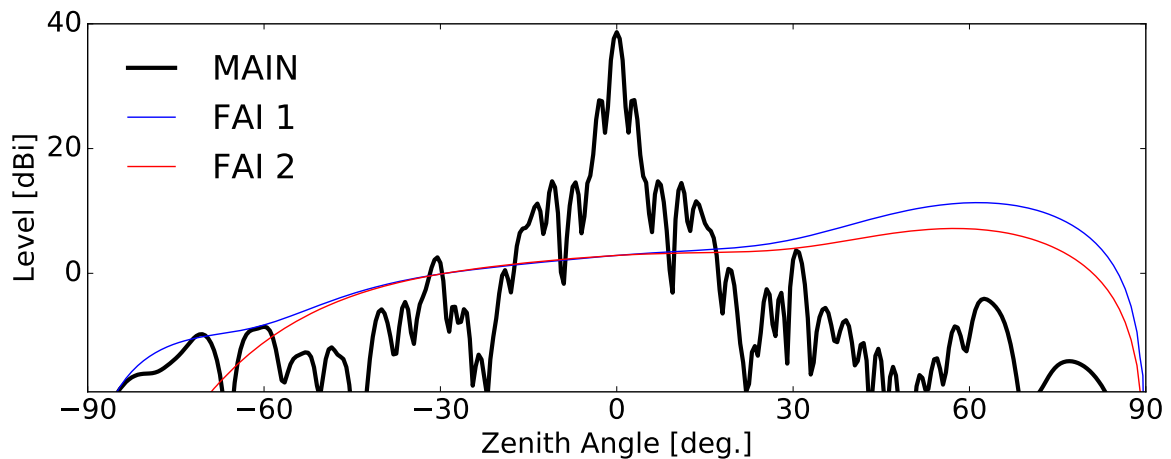


Figure 4.4: The radiation pattern of the PANSY radar.

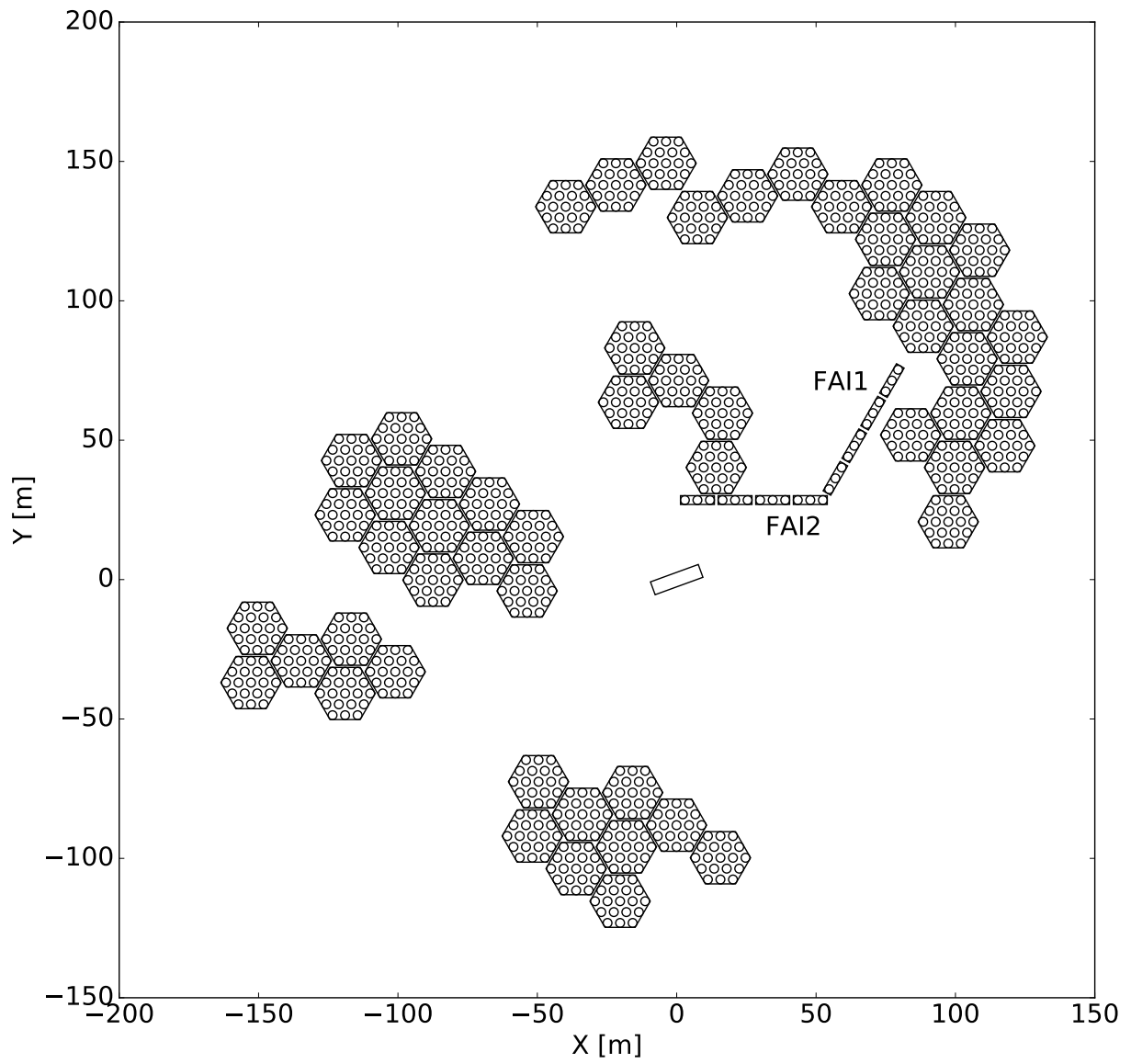


Figure 4.5: The antenna position and channel assignment of the PANSY radar.

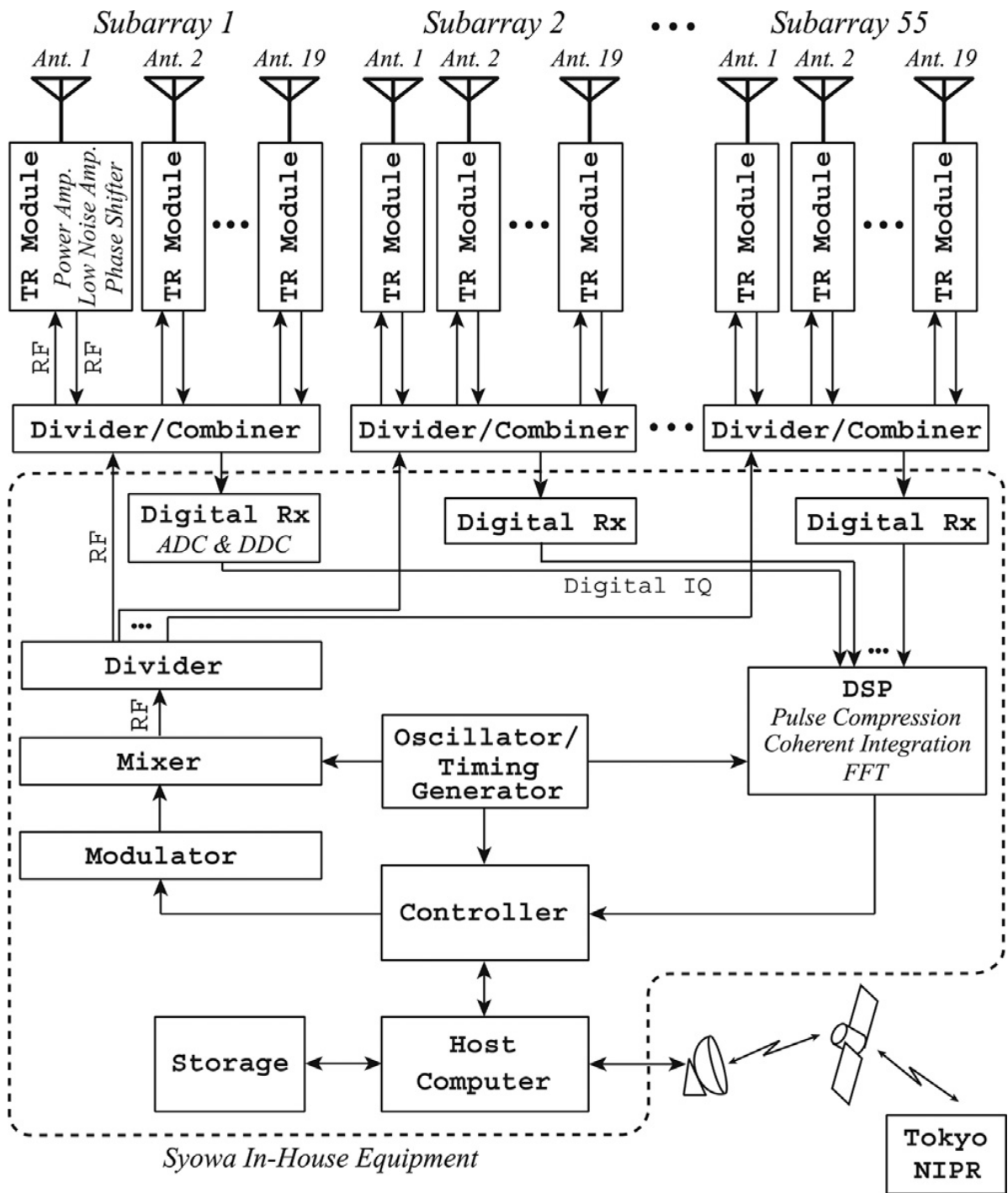


Figure 4.6: The block diagram of of the PANSY radar (Sato et al., 2014).

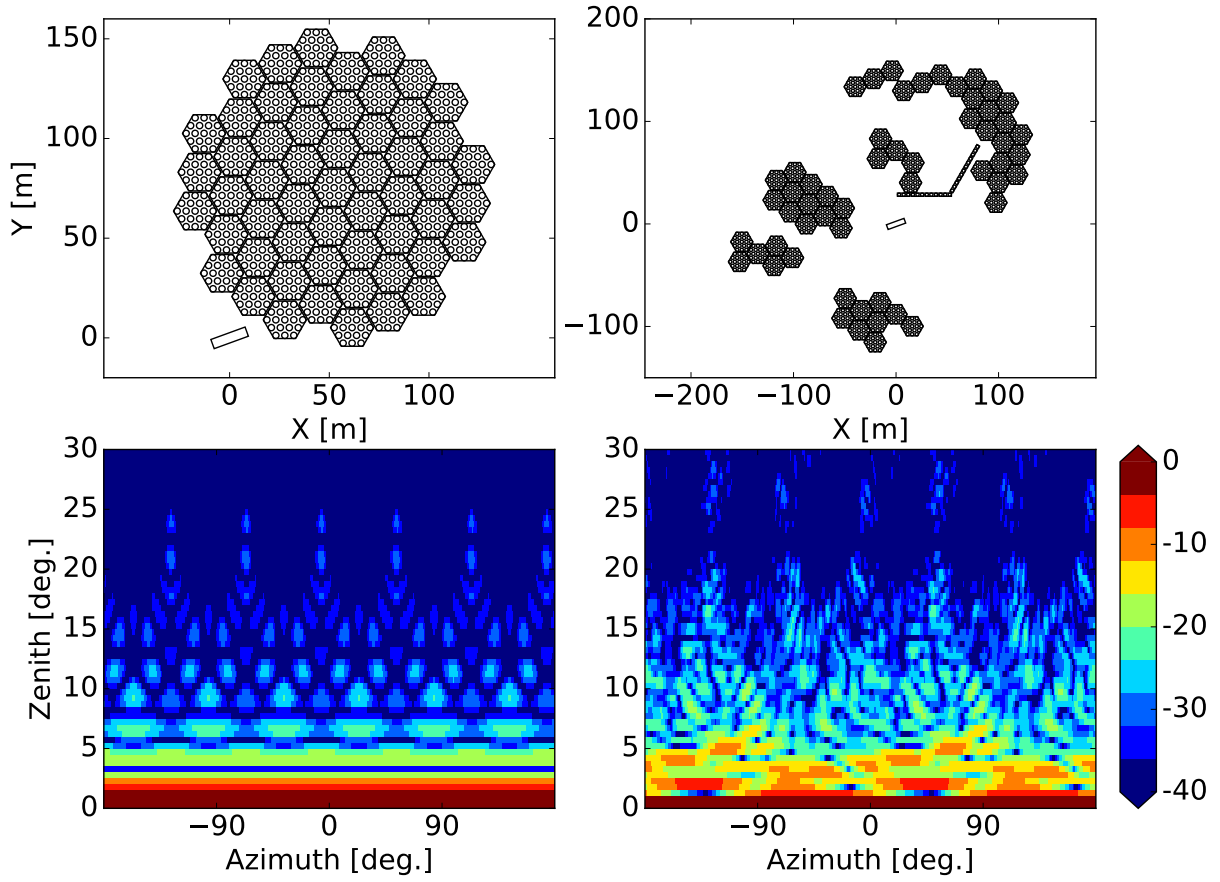


Figure 4.7: The planning (upper left) and current (upper right) antenna arrangement and the resulting array patterns (lower) of the PANSY radar.

As in Sato et al. (2014), the original antenna arrangement of the PANSY radar was the quasi-circular dense array with its diameter of 160 m. However, due to heavy snowfall at the Syowa Station during the winter of 2011, part of antennas was relocated to where the snow depth is relatively low. This made the PANSY radar to have roughly five distributed blocks of hexagonal subarrays, shown in the upper right portion of Fig. 4.7. While this does not change the superficial power aperture product of the array, the antenna pattern is changed to have much narrower mainlobe, as shown in the lower panels of Fig. 4.7. Thus, the radar volume  $V$  becomes smaller in this case, and the actual received power including this effect must be evaluated by the spherical integral on the two-way beam pattern  $P_{\text{TR}}$ :

$$P_{\text{TR}} = \iint G_{\text{Tx}}(\theta, \phi) G_{\text{Rx}}(\theta, \phi) d\theta d\phi, \quad (4.15)$$

where  $G_{\text{Tx}}(\theta, \phi)$  and  $G_{\text{Rx}}(\theta, \phi)$  are the Tx and Rx beam patterns.  $P_{\text{TR}}$  corresponds to the terms  $GA_eV$  in Eq. (1.14) as follows:

$$GA_eV = \iint G_{\text{Tx}}(\theta, \phi) \frac{\lambda^2}{4\pi} G_{\text{Rx}}(\theta, \phi) \Delta r d\theta d\phi = \frac{\lambda^2}{4\pi} P_{\text{TR}}. \quad (4.16)$$

Substituting Eq. (4.16) into Eq. (1.14) yields:

$$P_r = \frac{P_t \lambda^2 \Delta r}{(4\pi)^3 r^4} P_{\text{TR}} \eta. \quad (4.17)$$

By calculating the actual received power using Eq. (4.17), the current distributed arrangement of the PANSY radar appears to have 4.56 dB smaller echo power than the originally planned dense circular arrangement. Therefore, it should be noted that the sensitivity of atmospheric radars cannot always be evaluated by the power aperture product when the target system employs a distributed antenna arrangement.

## 4.4 Numerical simulations

### 4.4.1 Simulation settings

As mentioned in section 4.3, the target radar system is based on the PANSY radar. In this simulation, two of the 55 subarrays were not used, reducing the total number of subarrays to 53, which is the same setting for observations used in section 4.5. Other observational parameters are outlined in Table 4.2.

As mentioned in section 1.7.2, a nonuniform-gain configuration is preferable to retain the shape of the mainlobe. To confirm this is the case, both uniform-gain and nonuniform-gain configurations are considered in this simulation. In both configurations, the whole array was divided into eight groups, illustrated in Fig. 4.8. For the uniform-gain configuration, the array was divided into roughly the same-sized subgroups, which are surrounded with polygonal frames in Fig. 4.8. In contrast, for the nonuniform-gain configuration, seven subarrays, indicated by black circles in a hexagonal arrangement, were used as sidelobe cancellers. The other 46 subarrays indicated by white circles were synthesized by nonadaptive beamforming; these are referred to as the main array. Figure 4.9 shows the power directionality of the main array and one of the elements of the subarray in the azimuth section at  $45^\circ$ .

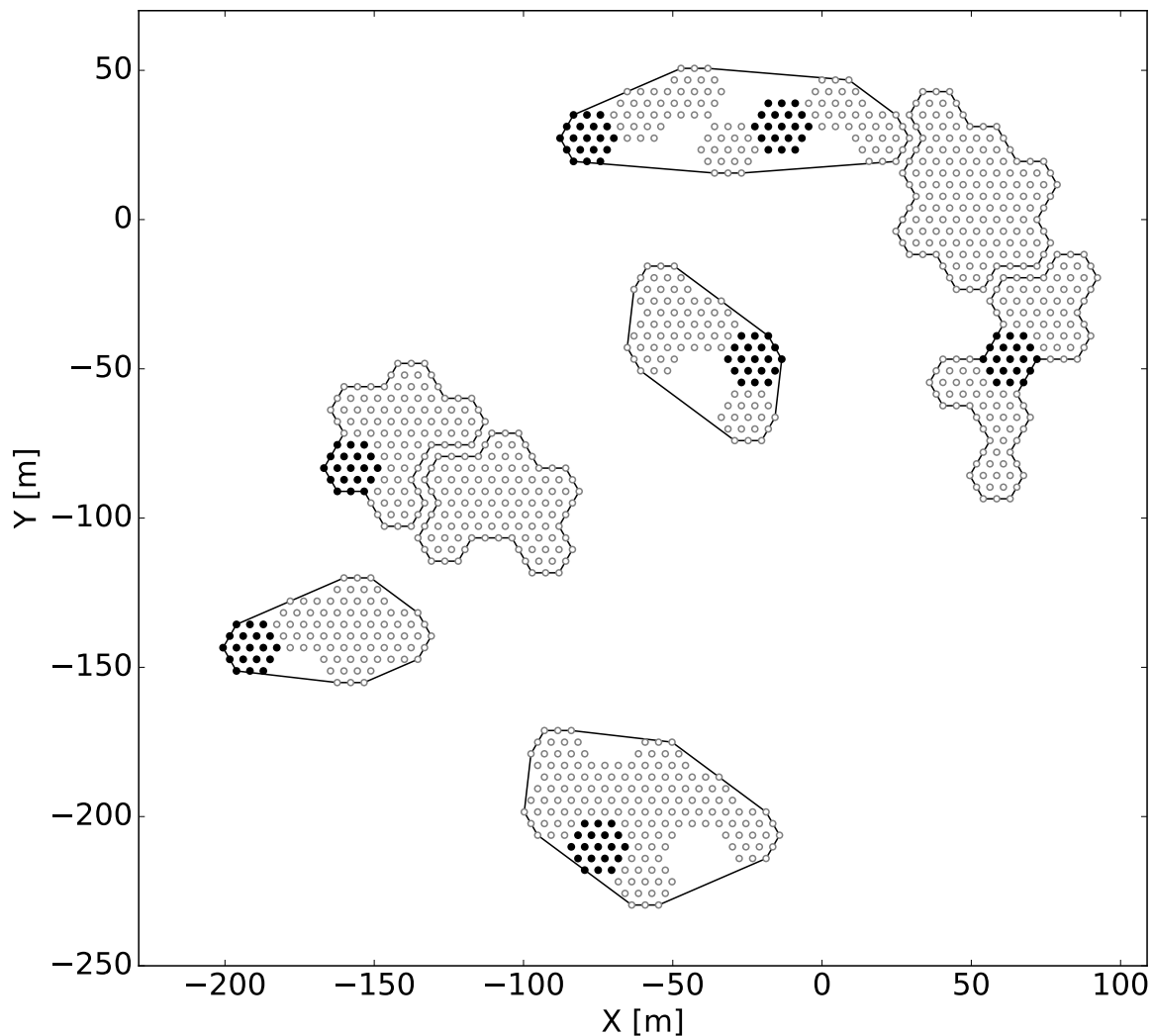


Figure 4.8: Antenna position and subarray configuration of the PANSY radar used for simulations and observations. Each set of antennas surrounded by a polygonal frame indicates a single channel in the uniform-gain configuration. Each hexagon with black circles indicates a subarray used as the sidelobe canceller in the nonuniform-gain configuration. In the nonuniform-gain configuration, all antennas with white circles are synthesized in-phase.

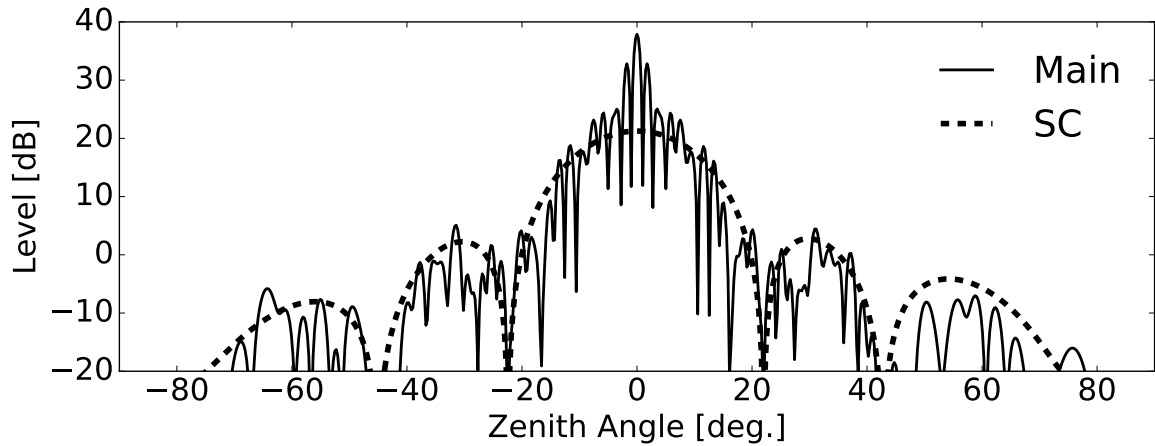


Figure 4.9: Power directionality pattern of the main array (Main) and one of the subarrays of the sidelobe canceller array (SC) used for observations. This is the section at an azimuth angle of  $45^\circ$ .

#### 4.4.2 Signal generation

In this simulation, there are three types of signals: atmospheric echoes, noise, and stationary clutter. The detailed procedures for generating these signals are described below.

##### Atmospheric echoes

Atmospheric echoes were generated using the atmospheric backscatter simulator developed by Holdsworth and Reid (1995). Detailed procedure of this method is explained in section 2.3.2. Table 4.1 lists the simulation parameters used to generate atmospheric echoes. The time series generated using this simulator for each receiver  $i = 1, \dots, M$  is written as  $\mathbf{s}(k) = [s_1(k) \cdots s_M(k)]$ , where  $k$  is the sampling time index.

##### Ground clutter

Ground clutter is modeled by point targets at low elevation angles with random directions. In this simulation, five point sources were generated at directions determined by a uniform random number in the range  $(60^\circ, 80^\circ)$  for the zenith angle, and  $[0^\circ, 360^\circ)$  for the azimuth angle. Thus, the complex time series of the received signal at each receiver

Table 4.1: Simulation parameters used for generating atmospheric backscatter signals.

Radar frequency	46.5 MHz
Range	10 km
Range resolution	150 m
Beam width	3.6°
Beam direction	(0°, 0°)
Enclosing volume radius	600 m
Enclosing volume height	500 m
No. of scatterers	200
Background wind (vertical)	1 m s <sup>-1</sup>
Background wind (horizontal)	20 m s <sup>-1</sup>
Spectral width	0.5 m s <sup>-1</sup>
Time resolution	51.2 ms
No. of time samples $N_t$	1024
SNDR	20 dB, 40 dB

$\mathbf{u}(k) = [u_1(k), \dots, u_M(k)]$  can be modeled as:

$$u_i(k) = \sqrt{P_1} \sum_{j=1}^5 A_i(\theta_j, \phi_j) G_i(\theta_j, \phi_j), \quad (i = 1, \dots, M) \quad (4.18)$$

where  $P_1$  is the total power from all clutter sources,  $(\theta_j, \phi_j)$  is the direction of the  $j$ -th clutter source, and  $G_i(\theta_j, \phi_j)$  is the directionality gain for direction  $(\theta_j, \phi_j)$  of the  $i$ -th receiver. Note that Eq. (4.18) depends only on the incident angle  $(\theta_j, \phi_j)$ , because each ground clutter signal is modeled as a stationary source and its location is independent of time. The clutter power  $P_1$  is selected such that the total SIDR obtained by nonadaptive beamforming is equal to the designated value. Here, the SIDR is defined as the peak distance between the atmospheric and clutter spectra. The periodogram of the clutter signal with 8-time incoherent integration is calculated as:

$$\bar{S}_u(v_d) = \sum_{m=1}^8 \left| \mathcal{F} [\mathbf{W}^H(k_m) \mathbf{u}(k_m)] \right|^2, \quad (4.19)$$

where  $\mathcal{F}[\cdot]$  denotes the Fourier transform,  $k_m = k + N_f(m - 1)$  ( $k = 1, \dots, N_f$ ) is the sample index in the  $m$ -th periodogram, and  $N_f = 128$  is the length of each periodogram. Then,  $P_1$  is determined such that the INDR satisfies the following equation:

$$\text{INDR} = P_1 \bar{S}_u(0), \quad (4.20)$$

where  $\bar{S}_u(0)$  is the zero Doppler frequency component of the periodogram  $\bar{S}_u(v_d)$ . Here, INDR is defined as the peak height of the clutter spectrum compared with the noise floor level.

### 4.4.3 Signal processing and performance evaluation

For both uniform- and nonuniform-gain configurations, the DCMP algorithm, the NC-DCMP algorithm, and the proposed PB algorithm are applied to the received signal  $\mathbf{X}(k)$ , defined by:

$$\mathbf{X}(k) = \mathbf{s}(k) + \mathbf{n}(k) + \mathbf{u}(k), \quad (4.21)$$

where noise  $\mathbf{n}(k)$  is generated following the procedure in section 2.3.4. The sample covariance matrix, given by:

$$\mathbf{R}(k) = \sum_{k_i=k-N_w}^{k+N_w} \mathbf{X}(k_i)\mathbf{X}(k_i)^H, \quad (4.22)$$

is calculated using  $2N_w + 1 = 513$  snapshots around the sampling time index  $k$ . The sampling interval is  $\Delta t = 51.2$  ms, which is equivalent to time averaging over approximately 26 s. The permissible SNR degradation of the NC-DCMP algorithm was set to 0.5 dB, which corresponds to the norm constraint,  $U \sim 1.12$ . As listed in Table 4.1, the beam direction is  $(\theta_o, \phi_o) = (0^\circ, 0^\circ)$ . All antennas have the same element gain function; thus, the gain weighting coefficients of the nonuniform-gain configuration are proportional to the number of antennas in the main and subarrays, i.e., 874 and 19. Therefore,  $G_1 = 46$  and  $G_{2,\dots,53} = 1$  are used.

Once the optimal weight vector  $\mathbf{W}(k)$  has been calculated, the performance of each method for both configurations is measured by the SINDR and the beam directional error. The SINDR is calculated through Eq. (2.4). The periodogram of the atmospheric echo  $\bar{S}(v_d)$  is calculated in the same manner as the periodogram of the clutter signal using Eq. (4.19). To calculate the beam directional error, the beam direction  $(\theta(k), \phi(k))$  is first calculated by determining the direction of the most significant peak of the power directionality pattern with the optimal weight vector  $\mathbf{W}(k)$ :

$$(\theta(k), \phi(k)) = \underset{\theta, \phi}{\operatorname{argmax}} |\mathbf{W}^H(k)\mathbf{A}(\theta, \phi)|^2. \quad (4.23)$$

The beam directional error  $e_b(k)$  is then calculated by taking the average of the angles between the two radial vectors  $\mathbf{V}(\theta, \phi)$  and  $\mathbf{V}(\theta(k), \phi(k))$ , as described by:

$$e_b(k) = \arccos \frac{\mathbf{V}(\theta, \phi) \cdot \mathbf{V}(\theta(k), \phi(k))}{\|\mathbf{V}(\theta, \phi)\|^2 \|\mathbf{V}(\theta(k), \phi(k))\|^2}, \quad (4.24)$$

where  $\mathbf{A} \cdot \mathbf{B}$  denotes the inner product of the vectors  $\mathbf{A}$  and  $\mathbf{B}$ . Radial vector  $\mathbf{V}(\theta, \phi)$  is defined in Eq. (1.20).

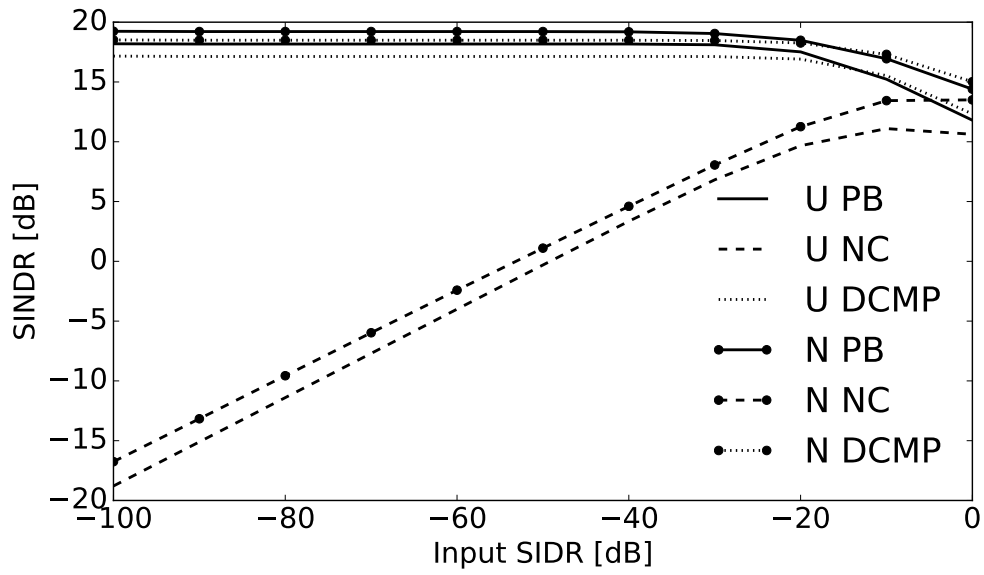
To obtain averages for the SINDR and the beam directional error for both the uniform- and nonuniform-gain configurations, 100 Monte Carlo simulations were executed for two SNDR cases: 20 dB and 40 dB. In each simulation, the input SIDR was increased from  $-100$  dB to 0 dB at intervals of 10 dB.

#### 4.4.4 Results and discussion

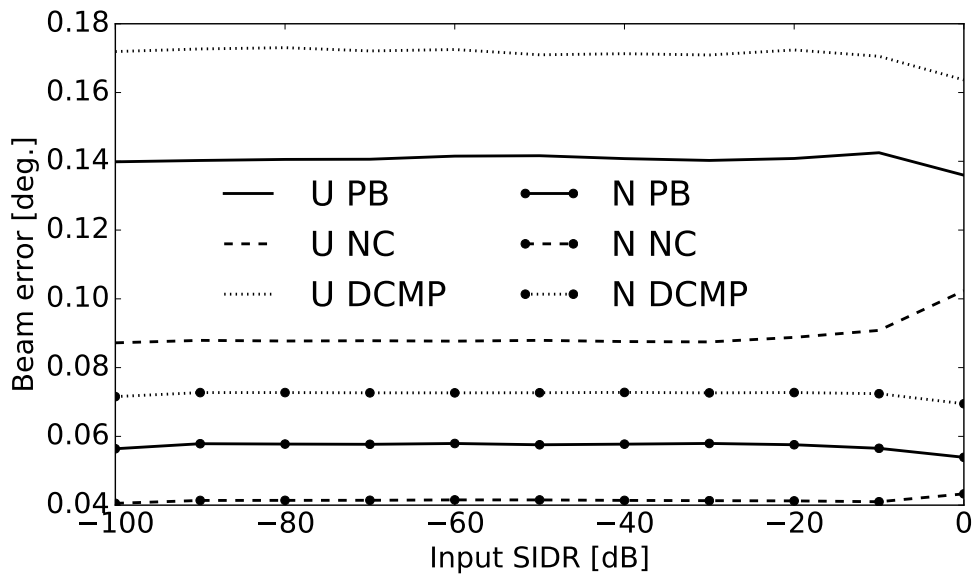
Figures 4.10a and 4.10b show the average SINDRs and beam directional errors for the DCMP algorithm, conventional NC-DCMP algorithm, and the proposed PB algorithm for both uniform- and nonuniform-gain configurations. The input SIDRs are from  $-100$  dB to 0 dB, while the input SNDR is 20 dB in these figures. Figures 4.11 and 4.12 show the average SINDRs and examples of the reception beam patterns for the DCMP, NC-DCMP, and PB algorithms, respectively. In these figures, the input SNDR is 40 dB. The azimuth angle for Fig. 4.12 is  $45^\circ$ .

As shown by Figs. 4.10a and 4.10b, the nonuniform-gain configuration gives a better result than the uniform-gain configuration for all of the signal processing methods, i.e., it has higher SINDRs and smaller beam directional errors. In particular, Fig. 4.10b shows that the beam directional error reaches about  $0.17^\circ$  for the DCMP algorithm and the uniform-gain configuration, but is less than  $0.08^\circ$  for the nonuniform-gain configuration. It should be noted that during vertical wind measurement, leakage of the horizontal wind speed can cause severe error. This is because the vertical wind speed is usually very small, e.g., mostly less than about  $0.4 \text{ m s}^{-1}$  in observations from the PANSY radar (Sato et al., 2014). Thus, such errors are undesirable for the DBS method, although they can be corrected by calculating the actual beam direction using each weight vector with Eq. (4.23). In this case, the improvement corresponds to about  $0.07 \text{ m s}^{-1}$  smaller vertical wind speed error, when the horizontal wind speed is  $40 \text{ m s}^{-1}$ , which is a considerable improvement. These results confirm the discussion of the advantages of a nonuniform-gain configuration in section 1.7.2; this configuration ensures that the noise power increase and the loss of the signal power are kept small through gain weighting. Because other trends for both configurations are almost the same, only the results from the nonuniform-gain configuration are discussed hereafter.

As shown in Fig. 4.10a, the PB algorithm averages the best output SINDR against the input SIDR variation. The DCMP algorithm performs similarly, although its SINDR is about 0.8 dB lower, equivalent to 16.8% on a linear scale. Note that this represents considerable degradation in terms of the system sensitivity, because it is equivalent to the loss of transmitted power. Compared with the PB and DCMP algorithms, the output



(a)



(b)

Figure 4.10: (a) Average SINDR, and (b) beam directional error compared with the nonadaptive beamforming for the DCMP algorithm (DCMP), NC-DCMP algorithm (NC), and the proposed PB algorithm (PB) in the simulation for uniform-gain (U) and nonuniform-gain (N) configurations. The input SNDR is 20 dB.

SINDRs of the NC-DCMP algorithm are inferior, because of the fixed norm constraint. The NC-DCMP algorithm only uses information about the noise power increase, resulting in a diagonal-loading level which is too strict to suppress clutter in this case. In contrast, the PB algorithm automatically selects the smaller diagonal-loading level to suppress these clutter, demonstrating its universality against the SIDR variations.

For the SIDRs above  $-20$  dB, the PB algorithm has a slightly lower SINDR than the DCMP algorithm, namely about  $0.5$  dB. This is because clutter is not completely suppressed in this region, even by the DCMP algorithm. As shown by Kamio and Sato (2004), the null depth formed by the DCMP algorithm depends on the strength of the clutter; hence, weak clutter is difficult to suppress. Because the PB algorithm measures SIR degradation using the difference calculated with the DCMP algorithm, the residual clutter power estimated by the PB algorithm tends to be larger than the DCMP algorithm. Therefore, if clutter is left by the DCMP algorithm, then the PB algorithm also fails to estimate the actual clutter power, resulting in a higher residual clutter power than for the DCMP algorithm.

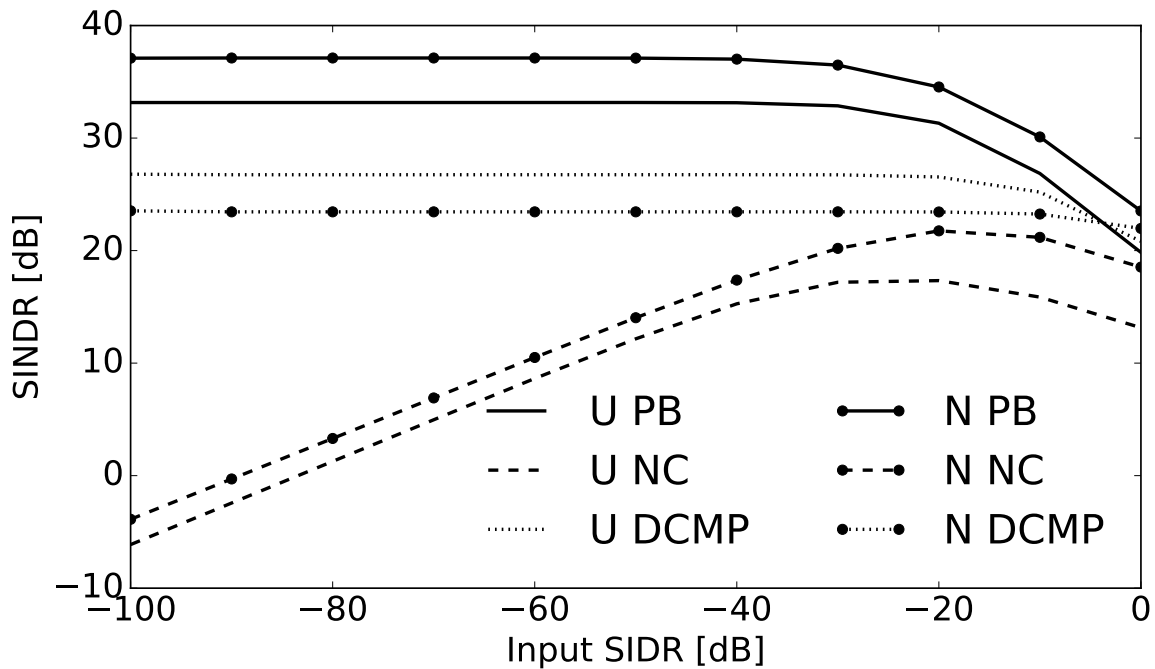


Figure 4.11: Average SINDRs for the input SNDR of 40 dB.

Although the SINDR of the DCMP algorithm was comparable to the PB algorithm in the previous case, it degrades markedly, when the input SNDR is 40 dB, as shown in Fig. 4.11. The SINDR of the DCMP algorithm is on average about 10 dB lower than that of the PB algorithm. In this case, the loss of the signal power is not negligible for the DCMP algorithm because the shape of the beam pattern is changed, as shown in Fig. 4.12. In contrast, the PB algorithm uses the minimum diagonal-loading value to preserve the main beam shape, as described in section 4.2, which ensures its robustness against input SNDR variation.

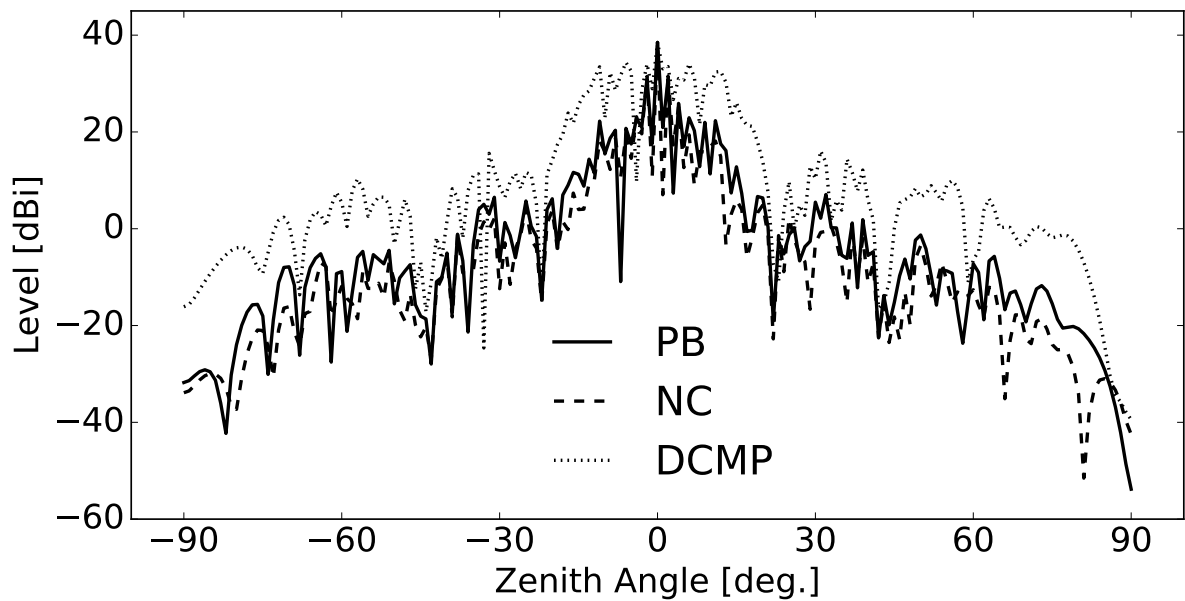


Figure 4.12: An example of the reception beam pattern synthesized by the DCMP algorithm (DCMP), NC-DCMP algorithm (NC), and the proposed PB algorithm (PB) when the input SNDR is 40 dB. This is the section at an azimuth angle of 45°.

From the above discussion, it can be concluded that the proposed PB algorithm has desirable characteristics for atmospheric radars, and can clearly replace the conventional NC-DCMP algorithm. In the following section, the proposed PB algorithm is applied to observational data to examine its performance in real applications.

Table 4.2: Parameters for observations made on March 20, 2015, by the PANSY radar.

Radar frequency	47 MHz
Ranges	1.5 km to 37 km
Range resolution	150 m
No. of beam directions	5 (zenith, N, E, S, and W)
Zenith angle for oblique beams	10°
Time resolution	51.2 ms
No. of frequency bins $N_f$	128
No. of Incoherent Integration $N_i$	8
No. of range samples $N_r$	157

## 4.5 Application to radar observations

### 4.5.1 Observations

An observation was made on March 20, 2015, by the PANSY radar at Syowa station, Antarctic (Sato et al., 2014). The settings are the same as those used in the simulation in section 4.4, except that only the nonuniform-gain configuration is considered, because it shows better performance. Here, the north beam directed to  $(\theta_o, \phi_o) = (10^\circ, 0^\circ)$  is used. Observations from 12:36 – 13:15 UTC are used for averaging.

### 4.5.2 Signal processing

The standard DCMP algorithm, the NC-DCMP algorithm, and the proposed PB algorithm are applied to a nonuniform-gain configuration with eight receivers, as described in section 4.4.1. Thus, the gain weighting coefficients are set to  $G_1 = 874$  and  $G_{2,\dots,8} = 19$ . This is determined by the number of antennas in each array, as discussed in section 4.4.3. The permissible SNR loss for the NC-DCMP algorithm is set to 0.5 dB, which corresponds to the norm constraint,  $U \sim 1.12$ .

The performance of the beamformer is evaluated using a periodogram, averaged over an observation period of about 40 min to reduce statistical fluctuations. The number of incoherent integrations is 60, and each periodogram consists of  $N_f = 128$  frequency bins.

Before incoherent integration, the noise floor level is corrected using the average squared norm of the weight vector in a range-by-range manner. Each periodogram  $S(v_d)$  is written as:

$$S(v) = |\mathcal{F} [\mathbf{W}^H(k)\mathbf{X}(k)]|^2, \quad (4.25)$$

where  $k = 1, \dots, N_v$  is the sampling time index. As discussed in section 1.7.2, the increase in the noise floor level in the periodogram is proportional to the squared norm of the weight vector. Thus, the periodogram is normalized as in Eqs. (3.5) and (3.6) according to the average squared norm of the weight vector,  $\hat{S}(v)$ . This can be written as:

$$\hat{S}(v) = N_v S(v) / \sum_{k=1}^{N_v} \|\mathbf{W}(k)\|^2. \quad (4.26)$$

Note that this correction is not only required to compare the results of different adaptive beamforming algorithms, but also to ensure across range continuity of the noise power. Otherwise, the noise floor level may have a different bias in each range.

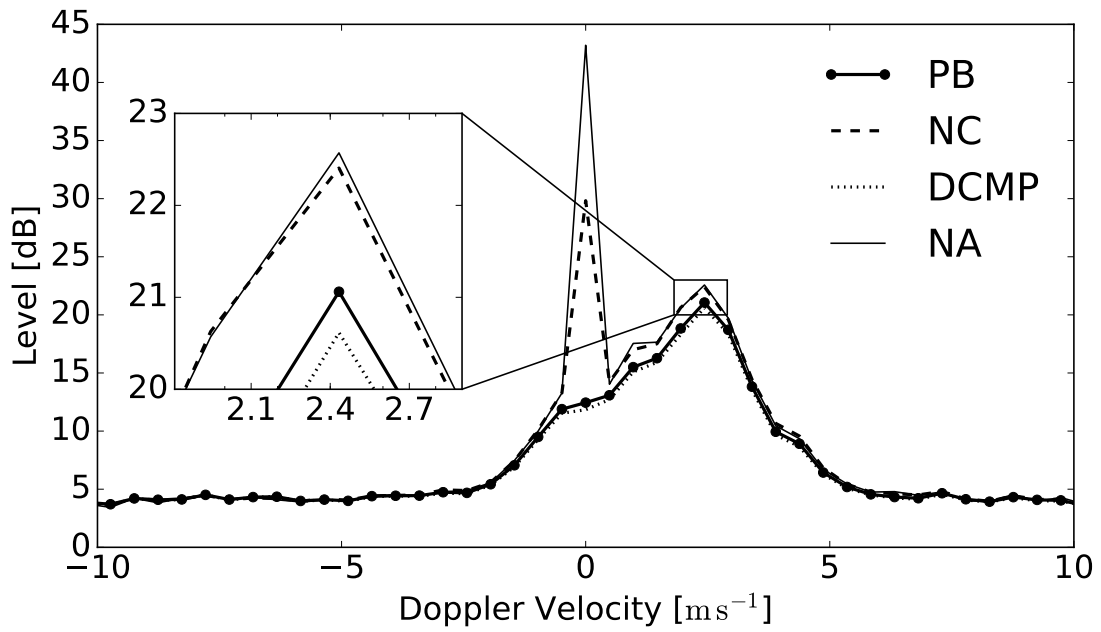
### 4.5.3 Results and discussion

Figures 4.13a and 4.13b show the Doppler spectra at 6.0 km and 4.2 km, after 60-time incoherent integration, which corresponds to about 40 min. Thin solid lines denote the nonadaptive beamforming, dotted lines denote the standard DCMP algorithm, dashed lines denote the conventional NC-DCMP algorithm, and thick solid lines with black markers denote the proposed PB algorithm.

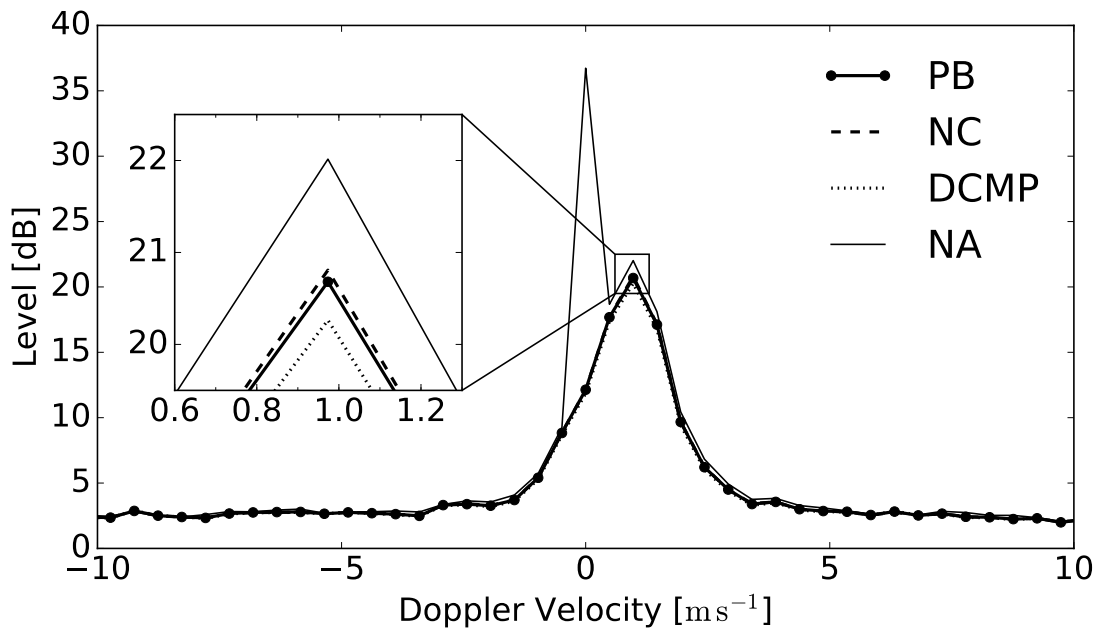
As seen in Fig. 4.13a, the strong ground clutter is left in the periodogram obtained from the NC-DCMP algorithm at 6.0 km. However, this ground clutter is sufficiently suppressed by the PB and DCMP algorithms, at a cost of about 1 dB additional SNDR degradation, compared with the NC-DCMP algorithm. The average diagonal-loading value  $\alpha$  for this range is  $\alpha_{\text{NC}} = 2.21 \times 10^2$  for the NC-DCMP algorithm and  $\alpha_{\text{PB}} = 2.57$  for the PB algorithm. Such a large difference in  $\alpha$  values implies that the ground clutter in this range is difficult to suppress, using the small norm constraint of  $U \sim 1.12$ . In this observation, a subarray consisting of 19 elements was used as the sidelobe canceller array, as described in section 4.4.1. As shown in Fig. 4.9, the power directionality pattern of the main array exhibits comparable responses at zenith angles around  $70^\circ$ , from where the ground clutter is expected. Therefore, the directionality pattern of the subarray may not be ideal, making the clutter from these directions difficult to suppress using the designated norm constraint.

In contrast to the 6.0 km case, Fig. 4.13b indicates that the ground clutter is suppressed by all three methods at 4.2 km. This is probably because the directionality pattern response of the subarray at the incident angle of the ground clutter is higher than in the previous case. The diagonal-loading values support this presumption because they are much smaller, i.e.,  $\alpha_{\text{NC}} = 0.40$ , and  $\alpha_{\text{PB}} = 0.69$ .

Now the results for the PB and DCMP algorithms are compared. The SNDR degrada-



(a)



(b)

Figure 4.13: Doppler spectra at (a) 6.0 km and (b) 4.2 km, which is averaged for about 40 min.

tion for the PB algorithm is about 0.9 dB and 0.4 dB less than that of DCMP algorithm, as shown in the zoomed portion of Figs. 4.13a and 4.13b. These values correspond to 18.7 % and 8.8 % on a linear scale, representing a substantial difference in terms of system sensitivity, as mentioned in section 4.4.4. However, the clutter suppression capabilities of these two methods are the same in both figures. This agrees with the simulation results in section 4.4, i.e., when the SNDR is about 20 dB and the SIDR is around  $-20$  dB, the PB and DCMP algorithms work similarly. However, the results from the simulation have also shown that the DCMP algorithm can cause a severe SNR degradation with high sidelobes, when the input SNDR is high. Therefore, the PB algorithm gives a better solution, even when SNR degradation caused by DCMP algorithm is not significant, because the PB algorithm can prevent an unpredictable noise power increase.

## 4.6 Summary and concluding remarks

A novel method to automatically determine the diagonal-loading level for robust adaptive beamforming on atmospheric radars by balancing the SIDR and SNDR degradations to maximize the detectability of the desired signals has been presented. The proposed PB algorithm evaluates the residual clutter power and increased noise power in the dimension of power spectral density, making the algorithm suitable for applications dealing with extremely weak signals. The proposed method also shows robustness against high SNDRs, when the performance of the standard DCMP algorithm deteriorates with high sidelobes. The algorithm includes a nonlinear least-squares problem, which increases its complexity compared with the conventional NC-DCMP algorithm. However, the computational complexity is still sufficiently small to be applied to real-time applications.

In section 4.4, the performance of the proposed algorithm was examined using numerical simulations. The proposed PB algorithm shows the greater universality and robustness compared with the DCMP or NC-DCMP algorithms, i.e., it automatically selects the smaller diagonal-loading value, or equivalently, mitigates the norm constraint when clutter is strong, and prevents the distortion of the beam pattern when the input SNDR is high. In addition, its automatic selection of the diagonal-loading level balances the SNR and SIR degradation, making this algorithm free of user-defined parameters. In section 4.5, the proposed algorithm was applied to observations from the PANSY radar. The results confirmed its universality and robustness in real applications. The proposed algorithm sufficiently suppressed ground clutter, even in ranges where the conventional NC-DCMP algorithm failed, with a smaller noise floor increase than the standard DCMP algorithm. From these results, the proposed PB algorithm is suitable for wind profilers,

and can readily replace the conventional NC-DCMP algorithm.

# Chapter 5

## Concluding remarks

This thesis has proposed the optimal array design and a novel robust adaptive beamforming algorithm for suppressing clutter in atmospheric radars. The proposed beamforming techniques were applied to actual observations from atmospheric radars, and the results confirmed the effectiveness of these techniques. The optimal array design is effective in both improving the clutter suppression capability and keeping the white noise gain lower than the ordinary equally-divided adaptive arrays with the same degrees of freedom. The proposed adaptive diagonal loading scheme automatically balances the SIR and SNR degradations to maximize the total detectability of the desired signal. Furthermore, the results from simulations and observations have shown that these two concepts can be applied at the same time, bringing the universality and robustness in suppressing the ground clutter compared with the conventional designs and algorithms.

In Chapter 2, the norm constrained power minimization approach was applied to the mesosphere observations of the MU radar. The applied NC-DCMP algorithm has been shown to be effective for improving the accuracy of the wind velocity estimation in mesospheric radar observation. The number of spectra discarded by the spectral thresholding to reject the contamination of meteor trail echoes was decreased because the meteor clutter was sufficiently suppressed by the adaptive beamforming. The weak meteor clutter that cannot be detected by the conventional spectral thresholding was also mitigated, thus expanding the observable range twice as wide as those given by the non-adaptive beamforming.

In Chapter 3, the optimal array design was investigated using numerical simulation by comparing two array configurations with the same degrees of freedom; uniform-gain configuration with equally-divided subarrays, and the nonuniform-gain configuration with a large main array supplemented by small sidelobe canceller subarrays. The results from the simulation have shown that the nonuniform-gain configuration is the more suitable array design, because it can achieve both the higher clutter suppression capability and smaller white noise gain compared with the uniform-gain configuration. Further-

more, the gain orthogonality between the main and sub arrays has been shown to be the key, i.e., the element gain function of the sidelobe canceller array should not have the response at the desired direction. The gain-weighted NC-DCMP algorithm strictly handles these gain differences to improve the clutter suppression capability per unit SNR degradation. The performance evaluation using the observational data from the MU radar has shown the consistent results with those in numerical simulations confirming the effectiveness of the partial adaptive array in atmospheric radars.

In Chapter 4, a novel diagonal loading scheme for balancing the SNR and SIR degradations was proposed. The proposed PB algorithm evaluates both the residual clutter power and increased noise power in dimensions of power spectral density as the estimated SIR and SNR degradations, respectively. The optimal diagonal-loading value is determined by balancing these two factors to maximizing the signal detectability in the spectrum. The results of applying the proposed algorithm to the observational data from the PANSY radar have shown that it has the better clutter suppression capability than the conventional norm constrained approach. Furthermore, the proposed algorithm has shown the robustness in the high SNDRs case when the performance of the standard DCMP algorithm deteriorates with high sidelobes.

Above results confirm that the proposed gain-weighted array design and PB algorithm can improve the accuracy of the wind measurements of atmospheric radars. While the outcome of these proposed techniques are quite promising, several more steps are required to actually improve the accuracy of the weather prediction using numerical models because the number of radars that can utilize such signal processing techniques is still limited. Hence, further technological innovation are expected to increase the phased array radars capable of adaptive beamforming with lower costs. In addition, quantitative analysis of the improvement in prediction accuracy in relation to the adaptive beamforming is another future work.

# Bibliography

- Alvarez, H., J. Aparici, J. May, and F. Olmos, 1997: A 45-MHz continuum survey of the southern hemisphere. *Astronomy and Astrophysics Supplement Series*, **124** (2), 315–328, doi:10.1051/aas:1997196.
- Applebaum, S. P., and D. J. Chapman, 1976: Adaptive arrays with main beam constraints. *IEEE Transactions on Antennas and Propagation*, **24** (5), 650–662, doi:10.1109/TAP.1976.1141416.
- Arnett, W. D., J. N. Bahcall, R. P. Kirshner, and S. E. Woosley, 1989: Supernova 1987A. *Annual review of Astronomy and Astrophysics*, **27**, 629–700, doi:10.1146/annurev.aa.27.090189.003213.
- Balsley, B. B., and K. S. Gage, 1982: On the use of radars for operational wind profiling. *Bulletin of the American Meteorological Society*, **63** (9), 1009–1018, doi:10.1175/1520-0477(1982)063<1009:OTUORF>2.0.CO;2.
- Booker, H. G., and W. E. Gordon, 1950: A theory of radio scattering in the Troposphere. *Proceedings of the IRE*, **38** (4), 401–412, doi:10.1109/JRPROC.1950.231435.
- Browning, K., and R. Wexler, 1968: The determination of kinematic properties of a wind field using Doppler radar. *Journal of Applied Meteorology*, **7** (1), 105–113, doi:10.1175/1520-0450(1968)007<0105:TDOKPO>2.0.CO;2.
- Capon, J., 1969: High-resolution frequency-wavenumber spectrum analysis. *Proceedings of the IEEE*, **57** (8), 1408–1418, doi:10.1109/PROC.1969.7278.
- Ceplecha, Z., J. Borovička, W. G. Elford, D. O. ReVelle, R. L. Hawkes, V. Porubčan, and M. Šimek, 1998: Meteor phenomena and bodies. *Space Science Reviews*, **84** (3–4), 327–471, doi:10.1023/A:1005069928850.
- Chapman, D., 1976: Partial adaptivity for the large array. *IEEE Transactions on Antennas and Propagation*, **24** (5), 685–696, doi:10.1109/TAP.1976.1141408.

- Chen, M.-Y., T.-Y. Yu, Y.-H. Chu, W. O. Brown, and S. A. Cohn, 2007: Application of capon technique to mitigate bird contamination on a spaced antenna wind profiler. *Radio Science*, **42** (6), doi:10.1029/2006RS003604.
- Cheong, B., R. Palmer, and M. Xue, 2008: A time series weather radar simulator based on high-resolution atmospheric models. *Journal of Atmospheric and Oceanic Technology*, **25** (2), 230–243, doi:10.1175/2007JTECHA923.1.
- Cheong, B. L., M. W. Hoffman, and R. D. Palmer, 2004: Efficient atmospheric simulation for high-resolution radar imaging applications. *Journal of Atmospheric and Oceanic Technology*, **21** (2), 374–378, doi:10.1175/1520-0426(2004)021<0374:EASFHR>2.0.CO;2.
- Compton, R. T., 1979: The power-inversion adaptive array: Concept and performance. *IEEE Transactions on Aerospace and Electronic Systems*, **AES-15** (6), 803–814, doi:10.1109/TAES.1979.308765.
- Compton, R. T., 1982: The effect of random steering vector errors in the applebaum adaptive array. *IEEE Transactions on Aerospace and Electronic Systems*, **AES-18** (4), 392–400, doi:10.1109/TAES.1982.309245.
- Cox, H., R. M. Zeskind, and M. M. Owen, 1987: Robust adaptive beamforming. *IEEE Transactions on Acoustics, Speech and Signal Processing*, **35** (10), 1365–1376, doi:10.1109/TASSP.1987.1165054.
- Crum, T. D., R. L. Alberty, and D. W. Burgess, 1993: Recording, archiving, and using WSR-88D data. *Bulletin of the American Meteorological Society*, **74** (4), 645–653, doi:10.1175/1520-0477(1993)074<0645:RAAUWD>2.0.CO;2.
- Curtis, C. D., M. Yeary, and J. L. Lake, 2016: Adaptive nullforming to mitigate ground clutter on the National Weather Radar Testbed Phased Array Radar. *IEEE Transactions on Geoscience and Remote Sensing*, **54** (3), 1282–1291, doi:10.1109/TGRS.2015.2477300.
- Doviak, R. J., D. S. Zrnic, and D. S. Sirmans, 1979: Doppler weather radar. *Proceedings of the IEEE*, **67** (11), 1522–1553, doi:10.1109/PROC.1979.11511.
- Du, L., T. Yardibi, J. Li, and P. Stoica, 2009: Review of user parameter-free robust adaptive beamforming algorithms. *Digital Signal Processing*, **19** (4), 567–582, doi:10.1016/j.dsp.2009.02.001.

- Ferguson, T., T. Lehman, and R. Balestri, 1976: Efficient solution of large moments problems: Theory and small problem results. *IEEE Transactions on Antennas and Propagation*, **24** (2), 230–235, doi:10.1109/TAP.1976.1141314.
- Fukao, S., K. Hamazu, and R. J. Doviak, 2014: *Radar for meteorological and atmospheric observations*. Springer, doi:10.1007/978-4-431-54334-3.
- Fukao, S., T. Tsuda, T. Sato, S. Kato, K. Wakasugi, and T. Makihira, 1985a: The MU radar with an active phased array system 1. Antenna and power amplifiers. *Radio Science*, **20** (6), 1155–1168, doi:10.1029/RS020i006p01155.
- Fukao, S., T. Tsuda, T. Sato, S. Kato, K. Wakasugi, and T. Makihira, 1985b: The MU radar with an active phased array system: 2. In-house equipment. *Radio Science*, **20** (6), 1169–1176, doi:10.1029/RS020i006p01169.
- Gage, K. S., and B. B. Balsley, 1978: Doppler radar probing of the clear atmosphere. *Bulletin of the American Meteorological Society*, **59** (9), 1074–1093, doi:10.1175/1520-0477(1978)059<1074:DRPOTC>2.0.CO;2.
- Guzmán, A. E., J. May, H. Alvarez, and K. Maeda, 2011: All-sky galactic radiation at 45 MHz and spectral index between 45 and 408 MHz. *Astronomy & Astrophysics*, **525**, A138, doi:10.1051/0004-6361/200913628.
- Harrington, R. F., and J. L. Harrington, 1996: *Field computation by moment methods*. Oxford University Press.
- Hashimoto, T., K. Nishimura, and T. Sato, 2016: Adaptive sidelobe cancellation technique for atmospheric radars containing arrays with nonuniform gain. *IEICE Transactions on Communications*, doi:10.1587/transcom.2016EBP3047, submitted for publication.
- Hashimoto, T., K. Nishimura, M. Tsutsumi, and T. Sato, 2014: Meteor trail echo rejection in atmospheric radars using adaptive sidelobe cancellation. *Journal of Atmospheric and Oceanic Technology*, **31** (12), 2749–2757, doi:10.1175/JTECH-D-14-00035.1.
- Hassenpflug, G., M. Yamamoto, H. Luce, and S. Fukao, 2008: Description and demonstration of the new Middle and Upper atmosphere Radar imaging system: 1-D, 2-D, and 3-D imaging of troposphere and stratosphere. *Radio Science*, **43** (2), doi:10.1029/2006RS003603.

- Heiss, W. H., D. L. McGrew, and D. Sirmans, 1990: NEXRAD: next generation weather radar (WSR-88D). *Microwave Journal*, **33** (1), 79–89.
- Hey, J. S., S. J. Parsons, and G. S. Stewart, 1947: Radar observations of the Giacobinid meteor shower, 1946. *Monthly Notices of the Royal Astronomical Society*, **107** (2), 176–183, doi:10.1093/mnras/107.2.176.
- Hildebrand, P. H., and R. Sekhon, 1974: Objective determination of the noise level in doppler spectra. *Journal of Applied Meteorology*, **13** (7), 808–811, doi:10.1175/1520-0450(1974)013<0808:ODOTNL.2.0.CO;2.
- Holdsworth, D. A., and I. M. Reid, 1995: A simple model of atmospheric radar backscatter: Description and application to the full correlation analysis of spaced antenna data. *Radio science*, **30** (4), 1263–1280, doi:10.1029/95RS00645.
- Hubbert, J., M. Dixon, and S. Ellis, 2009: Weather radar ground clutter. Part II: Real-time identification and filtering. *Journal of Atmospheric and Oceanic Technology*, **26** (7), 1181–1197, doi:10.1175/2009JTECHA1160.1.
- Hudson, J., 1981: *Adaptive array principles*, Vol. 11, 175–181. IET.
- Ishihara, M., Y. Kato, T. Abo, K. Kobayashi, and Y. Izumikawa, 2006: Characteristics and performance of the operational wind profiler network of the japan meteorological agency. *Journal of the Meteorological Society of Japan. Ser. II*, **84** (6), 1085–1096, doi:10.2151/jmsj.84.1085.
- Kamio, K., K. Nishimura, and T. Sato, 2004: Adaptive sidelobe control for clutter rejection of atmospheric radars. *Annales Geophysicae*, **22** (11), 4005–4012, doi:10.5194/angeo-22-4005-2004.
- Kamio, K., and T. Sato, 2004: An adaptive sidelobe cancellation algorithm for high-gain antenna arrays. *IEICE Transactions on Communications*, **87** (3), 11–18, doi:10.1002/ecja.10178.
- Kay, S. M., 1998: *Fundamentals of statistical signal processing, volume II: Detection theory*. Prentice Hall Upper Saddle River, NJ, USA.
- Kero, J., C. Szasz, T. Nakamura, T. Terasawa, H. Miyamoto, and K. Nishimura, 2012: A meteor head echo analysis algorithm for the lower VHF band. *Annales Geophysicae*, **30** (4), 639–659, doi:10.5194/angeo-30-639-2012.

- Koustov, A. V., K. Igarashi, D. Andr'e, K. Ohtaka, N. Sato, H. Yamagishi, and A. Yuki-matu, 2001: Observations of 50- and 12-MHz auroral coherent echoes at the Antarctic Syowa station. *Journal of Geophysical Research: Space Physics*, **106** (A7), 12–875, doi:10.1029/2000JA000165.
- Larsen, M. F., and J. Röttger, 1982: VHF and UHF Doppler radars as tools for synoptic research. *Bulletin of the American Meteorological Society*, **63** (9), 996–1008, doi: 10.1175/1520-0477(1982)063<0996:VAUDRA>2.0.CO;2.
- Latteck, R., W. Singer, M. Rapp, B. Vandepier, T. Renkwitz, M. Zecha, and G. Stober, 2012: MAARSY: The new MST radar on andøya: System description and first results. *Radio Science*, **47** (1), doi:10.1029/2011RS004775.
- Maeda, K., H. Alvarez, J. Aparici, J. May, and P. Reich, 1999: A 45-MHz continuum survey of the northern hemisphere. *Astronomy and Astrophysics Supplement Series*, **140** (2), 145–154, doi:10.1051/aas:1999413.
- Marquardt, D. W., 1963: An algorithm for least-squares estimation of nonlinear parameters. *Journal of the Society for Industrial and Applied Mathematics*, **11** (2), 431–441.
- May, J., F. Reyes, J. Aparici, M. Bitran, H. Alvarez, and F. Olmos, 1984: A 45-mhz array for radio astronomy. *Astronomy and Astrophysics*, **140**, 377–382.
- May, P. T., and R. G. Strauch, 1998: Reducing the effect of ground clutter on wind profiler velocity measurements. *Journal of Atmospheric and Oceanic Technology*, **15** (2), 579–586, doi:10.1175/1520-0426(1998)015<0579:RTEOGC>2.0.CO;2.
- McKinley, D. W. R., 1961: *Meteor Science and Engineering*. McGraw-Hill.
- McWhirter, J., 2000: Data-domain penalty function algorithm for stabilised adaptive beamforming. *IEE Proceedings - Radar, Sonar and Navigation*, **147** (6), 265–269, doi:10.1049/ip-rsn:20000753.
- Molteno, T. C., 2014: *NEC2++: An NEC-2 compatible Numerical Electromagnetics Code*. Department of Physics, University of Otago, New Zealand., URL <http://www.physics.otago.ac.nz/reports/electronics/ETR2014-3.pdf>.
- Morgan, D., 1978: Partially adaptive array techniques. *IEEE Transactions on Antennas and Propagation*, **26** (6), 823–833, doi:10.1109/TAP.1978.1141952.

- Nakamura, T., T. Tsuda, M. Tsutsumi, K. Kita, T. Uehara, S. Kato, and S. Fukao, 1991: Meteor wind observations with the MU radar. *Radio Science*, **26** (4), 857–869, doi:10.1029/91RS01164.
- Nishimura, K., T. Nakamura, T. Sato, and K. Sato, 2012: Adaptive beamforming technique for accurate vertical wind measurements with multi-channel MST radar. *Journal of Atmospheric and Oceanic Technology*, **29** (12), 1769–1775, doi:10.1175/JTECH-D-11-00211.1.
- Ogawa, T., 1997: Radar observations of ionospheric irregularities at Syowa Station, Antarctica: A brief overview. *Annales Geophysicae*, **14** (12), 1454–1461, doi:10.1007/s00585-996-1454-z.
- Pellinen-Wannberg, A., and G. Wannberg, 1994: Meteor observations with the European Incoherent Scatter UHF Radar. *Journal of Geophysical Research: Space Physics*, **99** (A6), 11 379–11 390, doi:10.1029/94JA00274.
- Petitdidier, M., A. Sy, A. Garrouste, and J. Delcourt, 1997: Statistical characteristics of the noise power spectral density in UHF and VHF wind profilers. *Radio Science*, **32** (3), 1229–1247, doi:10.1029/97RS00250.
- Richards, M. A., J. A. Scheer, and W. A. Holm, 2010: *Principles of Modern Radar: Basic Principles*. SciTECH Publishing.
- Rubinstein, A., M. Rubinstein, and F. Rachidi, 2006: A physical interpretation of the equal area rule. *IEEE Transactions on Electromagnetic Compatibility*, **48** (2), 258–263, doi:10.1109/TEMPC.2006.873861.
- Sato, K., M. Tsutsumi, T. Sato, T. Nakamura, A. Saito, Y. Tomikawa, K. Nishimura, M. Kohma, H. Yamagishi, and T. Yamanouchi, 2014: Program of the Antarctic Syowa MST/IS radar (PANSY). *Journal of Atmospheric and Solar-Terrestrial Physics*, **118A**, 2 – 15, doi:10.1016/j.jastp.2013.08.022.
- Sato, T., I. Atsuo, W. L. Oliver, S. Fukao, T. Tsuda, S. Kato, and I. Kimura, 1989: Ionospheric incoherent scatter measurements with the middle and upper atmosphere radar: Techniques and capability. *Radio Science*, **24** (1), 85–98, doi:10.1029/RS024i001p00085.
- Sato, T., and R. Woodman, 1982: Spectral parameter estimation of CAT radar echoes in the presence of fading clutter. *Radio Science*, **17** (4), 817–826, doi:10.1029/RS017i004p00817.

- Spano, E., and O. Ghebrehghan, 1996a: Pulse coding techniques for ST/MST radar systems: A general approach based on a matrix formulation. *IEEE Transactions on Geoscience and Remote Sensing*, **34** (2), 304–316, doi:10.1109/36.485109.
- Spano, E., and O. Ghebrehghan, 1996b: Sequences of complementary codes for the optimum decoding of truncated ranges and high sidelobe suppression factors for ST/MST radar systems. *IEEE Transactions on Geoscience and Remote Sensing*, **34** (2), 330–345, doi:10.1109/36.485111.
- Strauch, R., B. Weber, A. Frisch, C. Little, D. Merritt, K. Moran, and D. Welsh, 1987: The precision and relative accuracy of profiler wind measurements. *Journal of Atmospheric and Oceanic Technology*, **4** (4), 563–571, doi:10.1175/1520-0426(1987)004<0563:TPARAO>2.0.CO;2.
- Takao, K., M. Fujita, and T. Nishi, 1976: An adaptive antenna array under directional constraint. *IEEE Transactions on Antennas and Propagation*, **24** (5), 662–669, doi:10.1109/TAP.1976.1141411.
- Takao, K., and N. Kikuma, 1986: Tamed adaptive antenna array. *IEEE Transactions on Antennas and Propagation*, **34** (3), 388–394, doi:10.1109/TAP.1986.1143821.
- Torres, S. M., and D. S. Zrnic, 1999: Ground clutter canceling with a regression filter. *Journal of Atmospheric and Oceanic Technology*, **16** (10), 1364–1372, doi:10.1175/1520-0426(1999)016<1364:GCCWAR>2.0.CO;2.
- Tsuda, T., 1989: Data acquisition and processing. *Handbook for MAP*, **30**, 151–184.
- Tsuda, T., M. Yamamoto, T. Sato, S. Kato, and S. Fukao, 1985: Comparison observations between the MU radar and the Kyoto meteor radar. *Radio Science*, **20** (6), 1241–1246, doi:10.1029/RS020i006p01241.
- Tsutsumi, M., T. Tsuda, T. Nakamura, and S. Fukao, 1994: Temperature fluctuations near the mesopause inferred from meteor observations with the middle and upper atmosphere radar. *Radio Science*, **29** (3), 599–610, doi:10.1029/93RS03590.
- Urkowitz, H., and J. D. Nesor, 1992: Obtaining spectral moments by discrete Fourier transform with noise removal in radar meteorology. *IEEE International Geoscience and Remote Sensing Symposium, 1992*, IEEE, Vol. 1, 12–14, doi:10.1109/IGARSS.1992.576614.

- Valaee, S., B. Champagne, and P. Kabal, 1995: Parametric localization of distributed sources. *IEEE Transactions on Signal Processing*, **43** (9), 2144–2153, doi:10.1109/78.414777.
- Van Veen, B., and R. Roberts, 1987: Partially adaptive beamformer design via output power minimization. *IEEE Transactions on Acoustics, Speech and Signal Processing*, **35** (11), 1524–1532, doi:10.1109/TASSP.1987.1165069.
- von Zahn, U., and T. L. Hansen, 1988: Sudden neutral sodium layers: a strong link to sporadic E layers. *Journal of Atmospheric and Terrestrial Physics*, **50** (2), 93–104, doi:10.1016/0021-9169(88)90047-5.
- Woodman, R. F., 1985: Spectral moment estimation in MST radars. *Radio Science*, **20** (6), 1185–1195, doi:10.1029/RS020i006p01185.
- Woodman, R. F., and A. Guillen, 1974: Radar observations of winds and turbulence in the stratosphere and mesosphere. *Journal of the Atmospheric Sciences*, **31** (2), 493–505, doi:10.1175/1520-0469(1974)031<0493:ROOWAT>2.0.CO;2.
- Yamamoto, M., S. Fukao, R. F. Woodman, T. Ogawa, T. Tsuda, and S. Kato, 1991: Mid-latitude E region field-aligned irregularities observed with the MU radar. *Journal of Geophysical Research: Space Physics*, **96** (A9), 15 943–15 949, doi:10.1029/91JA01321.
- Yamamoto, M., T. Sato, P. T. May, T. Tsuda, S. Fukao, and S. Kato, 1988: Estimation error of spectral parameters of mesosphere-stratosphere-troposphere radars obtained by least squares fitting method and its lower bound. *Radio Science*, **23** (6), 1013–1021, doi:10.1029/RS023i006p01013.
- Yu, T.-Y., J.-I. Furumoto, and M. Yamamoto, 2010: Clutter suppression for high-resolution atmospheric observations using multiple receivers and multiple frequencies. *Radio Science*, **45** (4), doi:10.1029/2009RS004330.
- Zrnic, D. S., 1975: Simulation of weatherlike Doppler spectra and signals. *Journal of Applied Meteorology and Climatology*, **14** (4), 619–620, doi:10.1175/1520-0450(1975)014<0619:SOWDSA>2.0.CO;2.
- Zrnic, D. S., 1979: Estimation of spectral moments for weather echoes. *IEEE Transactions on Geoscience Electronics*, **17** (4), 113–128, doi:10.1109/TGE.1979.294638.

# Major publications

## Refereed Papers

1. Hashimoto, T., K. Nishimura, M. Tsutsumi, and T. Sato, 2014: Meteor Trail Echo Rejection in Atmospheric Phased Array Radars Using Adaptive Sidelobe Cancellation, *Journal of Atmospheric and Oceanic Technology*, **31** (12), 2749–2757, doi:10.1175/JTECH-D-14-00035.1.
2. Hashimoto, T., K. Nishimura and T. Sato, 2016: Adaptive Sidelobe Cancellation Technique for Atmospheric Radars Containing Arrays with Nonuniform Gain, *IEEE Transactions on Communications*, **E99 – B** (12), doi:10.1587/transcom.2016EBP3047, in press.

## Refereed Conference Proceedings

1. Hashimoto, T., K., Nishimura, K. Sato, and T. Sato, 2012: Adaptive suppression of aircraft clutter with the PANSY radar training system, *The 13th International Workshop on Technical and Scientific Aspects of MST radar*, **Mo-20**, 79–85, K uhlungsborn, Germany, March 2012.
2. Hashimoto, T., K. Nishimura, M. Tsutsumi, and T. Sato, 2014, An Adaptive Meteor Clutter Rejection Technique for Mesospheric Radar Observations, *The 14th International Workshop on Technical and Scientific Aspects of MST Radar*, **7**, S ao Jos e dos Campos/SP, Brazil, May 2014.
3. Hashimoto, T., K. Nishimura, M. Tsutsumi, T. Sato, and K. Sato, 2015: Basic Study on the Ionospheric Observations of the PANSY radar; Adaptive Sidelobe Cancellation Techniques for the FAI clutters, *The 37th Conference on Radar Meteorology*, Poster **1–8**, Norman OK, United States, September 2015.
4. Hashimoto, T., K. Nishimura, and T. Sato, 2015: Adaptive aircraft clutter rejection in wind profile observations of the MU radar, *2015 International Symposium on Earth-Science Challenges*, **5**, Norman OK, United States, September 2015.

5. Hashimoto, T., K. Nishimura, M. Tsutsumi, K. Sato, and T. Sato, 2016: Automatic diagonal-loading scheme for robust adaptive beamforming on atmospheric radars, *International Symposium on the Whole Atmosphere*, accepted for presentation, Tokyo, Japan, September 2016.